X-ray absorption spectroscopy of molecular-based spin-hybrid systems

Dissertation

genehmigt von der Fakultät für Physik an der

Universität Duisburg-Essen

zur Erlangung des akademischen Grades eines

Doktors der Naturwissenschaften

David Klar

aus Herne

1. Gutachter: Prof. Dr. Heiko Wende
2. Gutachter: Prof. Dr. Mario Ruben
3. Gutachter: Prof. Dr. Claus Michael Schneider
Datum der Disputation: 19. Februar 2016

Contents

Kurzfassung

Im Rahmen dieser Arbeit werden molekulare Spin-Hybrid Systeme auf ihre strukturellen, elektronischen und magnetischen Eigenschaften untersucht. Die Resultate sind entsprechend der verwendeten Molekülklassen in zwei Kapitel unterteilt. Im ersten Teil werden Systeme mit (quasi-)planaren paramagnetischen Molekülen mit einem 3*d*-Übergangsmetallion im Zentrum des Moleküls untersucht. Mit Hilfe von XMCD-Messungen wird gezeigt, dass sich die magnetischen Momente von FePc-Molekülen auf ferromagnetischen Co-Filmen ausrichten. Bei direktem Kontakt existiert eine ferromagnetische Kopplung bei Raumtemperatur. Durch eine Zwischenlage Sauerstoff, die die Moleküle von der Co-Oberfläche trennt, wird die Kopplung zwischen Molekül und Substrat antiferromagnetisch. Hingegen wird die Kopplung durch eine Graphen-Zwischenlage auf einem Ni(111)-Substrat lediglich geschwächt, aber die parallele Spinausrichtung von Co-Substrat und Fe-Ionen des FePc-Moleküls bleibt erhalten. Anders stellt sich die Situation bei CoOEP-Molekülen dar. Auf dem gleichen Substrat Graphen/Ni(111) koppeln die Co-Ionen antiferromagnetisch durch die Graphenschicht an das Ni-Substrat. Die magnetische Kopplung kann jedoch nur für die erste Molekülllage gezeigt werden, weitere Lagen sind entkoppelt. Durch die zwei verschieden gekoppelten Molekülllagen kann die Netto-Magnetisierung der CoOEP-Moleküle in der Multilage durch Veränderung des äußeren Magnetfeldes umgeschaltet werden.
Die zweite Molekülklasse sind sogenannte Einzelmolekülmagneten des Typs $LnPc_2$. Mit feldabhängigen XMCD-Messungen wird eine magnetische Remanenz der Moleküle bei Submonolagenbedeckung auf einem HOPG-Substrat nachgewiesen. Desweiteren kann eine magnetische Remanenz auch durch die antiferromagnetische Kopplung zu ferromagnetischen Filmen erzielt werden. Auf einem Ni-Film mit senkrechter Anisotropie ist die Kopplung stärker als auf dem Co-Film mit paralleler Anisotropie bezüglich der Oberfläche. Eine systematische Studie von XMCD Messungen und DFT-Rechnungen an den drei Molekülen $TbPc_2$, $DyPc_2$ und $ErPc_2$ auf einem Ni(111)-Einkristall zeigt eine antiferromagnetische Kopplung zwischen dem Ni-Substrat und jedem der drei Moleküle. $TbPc_2$ und $DyPc_2$ weisen dabei eine senkrechte Anisotropie auf, wohingegen $ErPc_2$ die leichte magnetische Richtung in der Pc-Ebene besitzt. Die Kopplung ist stark anisotrop und ist im Falle von $TbPc_2$ stabil bis zu einer Tempe-ratur von 120 K. Mit Hilfe von DFT-Rechnungen werden die Kommunikationskanäle im Ln-Ion und dem Liganden bestimmt, die für die magnetische Wechselwirkung wichtig sind. Die antiferromagnetische Kopplung wird durch Graphen zwischen dem Substrat und den $TbPc_2$ Molekülen übertragen, ist jedoch deutlich schwächer als bei direktem Kontakt zwischen Ni und $TbPc_2$.

Abstract

Within the framework of this thesis, molecular spin-hybrid systems are studied for their structural, electronic and magnetic properties. The results are divided into two chapters with respect to the investigated classes of molecules. In the first part, systems including (quasi-)planar paramagnetic molecules having a $3d$ transition metal ion in the molecules' center have been investigated. By means of XMCD measurements it is shown that the magnetic moments of the FePc molecules align on a ferromagnetic Co film. In direct contact, a ferromagnetic coupling exists at room temperature. Due to an interlayer of oxygen separating the molecules from the Co surface, the coupling becomes antiferromagnetic. However, a graphene interlayer on a Ni(111) single crystal solely reduces the coupling strength, but the parallel spin alignment of the Co substrate and the Fe ions of the FePc molecules is maintained. The situation is different in the case of CoOEP molecules. On the same substrate graphene/Ni(111), the Co ions couple antiferromagnetically via the graphene layer to the Ni substrate. The magnetic coupling can be shown for the first layer only, additional layers are decoupled. Due to the two different coupled molecular layers, the net magnetization of the CoOEP molecules in a multilayer can be switched by variation of the external magnetic field.
The second molecular class are so-called single molecule magnets of the type $LnPc_2$. By field-dependent XMCD measurements, a magnetic remanence of the molecules is proven at submonolayer coverage on HOPG substrate. Furthermore, a magnetic remanence can be achieved by antiferromagnetic coupling to ferromagnetic films. On a Ni film with perpendicular anisotropy the coupling is stronger than on the Co film with parallel anisotropy with respect to the surface. A systematic study of XMCD measurements and DFT calculations on the three molecules $TbPc_2$, $DyPc_2$ and $ErPc_2$ on a Ni(111) single crstal shows antiferromagnetic coupling between the Ni substrate and each of the molecules. $TbPc_2$ and $DyPc_2$ feature a perpendicular anisotropy, while $ErPc_2$ has an easy axis of magnetization in the Pc plane. The coupling is highly anisotropic and in case of $TbPc_2$ stable up to 120 K. By means of DFT calculations the communication channels in the Ln ion and the ligands which are responsible for the magnetic interaction are determined. The antiferromagnetic character of the coupling is also mediated via a graphene layer between the substrate and the $TbPc_2$ molecules, but is significantly weaker than for the direct contact between Ni and $TbPc_2$.

1. Introduction

The field of spintronics, which consists in using the spin of the electron in addition to its charge, has appeared to be an exciting topic for fundamental research. Since the discovery of the giant magnetoresistance effect in 1988, more than twenty years ago, by Peter Grünberg and Albert Fert, both awarded with the Nobel price in 2007 [1, 2], spintronics has enabled the development of numerous new technologies used and needed on a daily basis [3–5]. Hard drives based on spintronics, for example, made it possible to store large amounts of data on devices small enough to fit into anyone's pocket.

Hybrid systems consisting of superconductors, ferromagnetic metals, non magnetic metals and insulators have been found to exhibit new properties and are already used in state of the art technologies, such as superconducting quantum interference device [6], giant magnetoresistance tunnel barriers [1] and tunnel magnetoresistance tunnel barriers [7], to name but a few. One step further is the implementation of molecular units into such systems, modifying electronic and magnetic properties on a size of a molecular, which is at least one order of magnitude smaller than caracteristic dimensions in spintronics devices, e. g. magnetic grains forming media for hard drives [8]. The potential increase in efficiency of future applications using molecular-based spin-hybrid systems makes molecular spintronics a very important topic of today's research [9–17].

The road towards such applications using the magnetic moment of a single molecule is long and rocky and much more research is needed to be carried out. This is all the more true when it comes to the interaction between individual molecules of not more than one nanometer in size and solid state materials with macroscopic characteristics. The new emerging properties of these spin-hybrid systems can vary drastically. However, the potential of such spin-hybrid system is large because of the possibility to tailor their properties by altering the composition, to suit the specific requirements.

Due to the complexity of these systems and the variety of combinations, the microscopic understanding is still incomplete and is currently being investigated by means of theoretical and experimental approaches. A comprehensive understanding of molecular-based spin-hybrid systems, their interactions and the resulting properties is necessary. In order to reach this goal, specific suitable systems need to be studied.

Spin effects at the interface of hybrid systems made of inorganic magnetic electrodes and organic molecules are currently at the heart of molecular spintronics [13]. While spin interface effects are commonly investigated in 2D structures, the key mechanisms can be naturally scaled down to the level of a single molecule [10, 18]. In this rapidly growing field, metal-organic complexes, comprising an organic group such as phthalocyanines and porphyrins and a metallic center such as a transition metal or a rare earth ion, represent a prototypical case due to their versatility and high stability. Particularly appealing is the possibility to control the spin state of such molecules by adsorption on opportune substrates or by doping [19–27]. This work was focused on studying the various spin-hybrid systems in order to develop a microscopic understanding of the interaction within the system, divided into two main chapters (4, 5) with respect to the type of molecules.

In chapter 4, the results on two planar, organic, paramagnetic molecules, Fe-phthalocyanine and Co-octaethylprophyrin, are presented. Phthalocyanines and porphyrins are sublimable molecules with a high thermal and chemical stability, and the ability to self-assemble on a surface. They are already used for prototype devices, but also for industrial and medical applications [28–35]. These properties make them excellent candidates to help investigating the molecule-surface interactions. The two molecules are very similar to each other in many respects, however, they also show clear differences concerning their chemical and physical properties. Determining the origin of these differences should lead to a deeper understanding of the molecular behavior, especially the molecule-surface interaction. In chapter 4, the focus is put on the possibility to manipulate the molecule's spin with the underlying substrate. The interaction between the molecule and the magnetic substrate is studied by taking into account the molecular adsorption geometry, the spin alignment and the field-dependence. A combination of structural characterization, x-ray magnetic circular dichroism and density functional theory calculations are used to determine the magnetic coupling mechanism. Also the influence of the ligand and the central $3d$ ion on the coupling is studied. Further modification of the substrate and additional graphene and oxygen interlayers lead to new properties and coupling phenomena. To describe the origin of different properties, the systems are studied with respect to the coupling type, coupling energy, charge transfer, van der Waals interaction, spin state and communication channels and the orbitals participating in the coupling. The following questions are addressed in this chapter:

- How do submonolayers of FePc and CoOEP behave on different surfaces? Do they stay intact and how do they assemble on the surface? Are they chemisorbed or physisorbed? Is there a significant charge transfer between the molecule and the substrate? What is the effect of different $3d$ ions and different ligands?

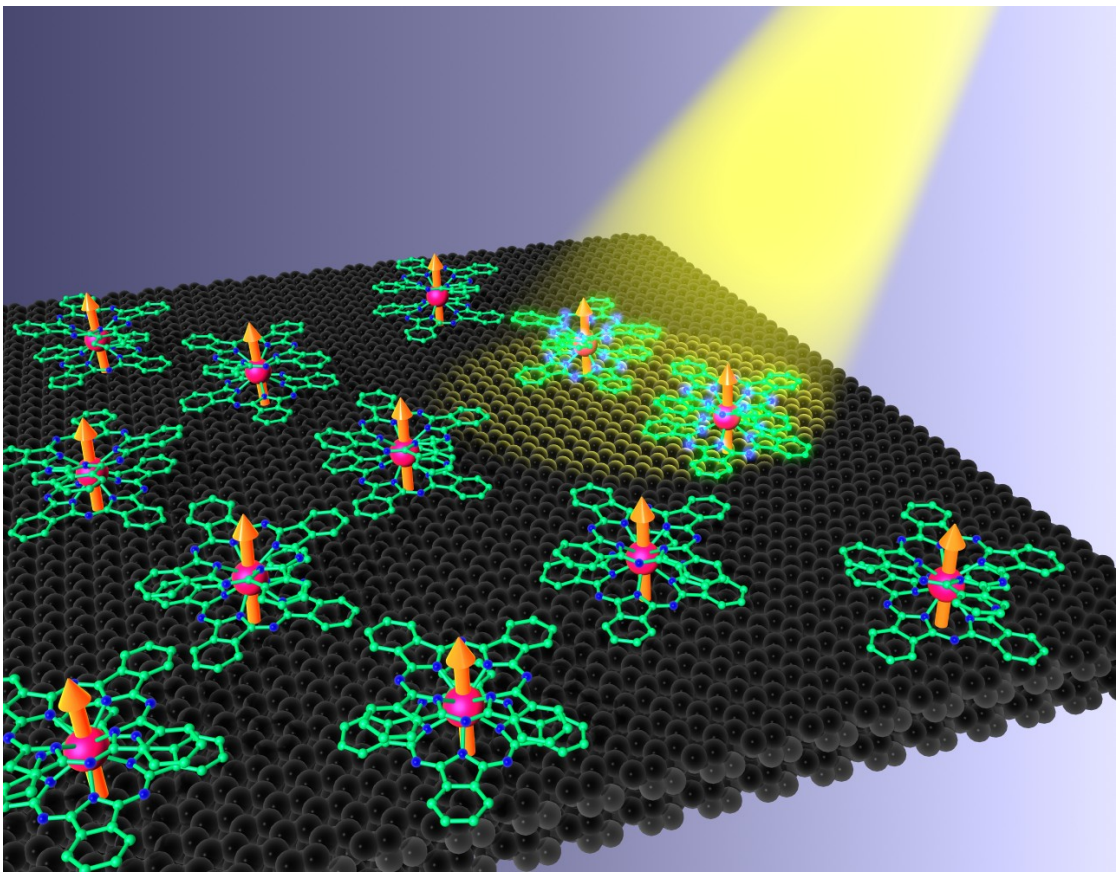

Figure 1.1.: Graphical representation of $LnPc_2$ molecules with parallel aligned magnetic moments on a graphite surface under x-ray irradiation [36]. Details to this experiment are given in chapter 5.

- How can the magnetization of the paramagnetic FePc and CoOEP molecules be stabilized? Is a stable magnetization at room temperature possible due to spin interface effects? What are the coupling phenomena in a microscopic picture? How does the insertion of interlayers affect the coupling? Is it possible to tailor the coupling?

- Is an interlayer coupling between molecular layers detectable and in which way is the field dependence of a molecular multilayer system different from a single layer system?

In the second part, chapter 5, the class of Ln-based single molecule magnets in the form $LnPc_2$ are investigated. Single molecule magnets are a special class of molecules, representing the smallest units possessing an intrinsic magnetic bistability and showing magnetic remanence below a certain blocking temperature without the need of long-range ferromagnetic ordering [37]. Compared to the paramagnetic phthalocyanine or porphyrin molecules, the spin relaxation times

for SMMs can be 10^8 times longer [10, 38, 39]. This unique characteristic of this bulk magnetic property in a molecular dimension makes SMM molecules attractive for nanoscale spintronic devices. An illustration of individual $TbPc_2$ molecules adsorbed on graphite is demonstrated in figure 1.1. In the specific case of $LnPc_2$ the large axial single ion anisotropy of the Dy and Tb ions leads to a remanent magnetization, but only at very low temperatures and on a short timescale [40]. The remanence is also shown to vanish, when the molecules are in contact with a non-magnetic, metallic substrate [41, 42]. Hence, the coupling to a ferromagnetic substrate is used to stabilize to magnetic moment of the molecules. Due to the strongly localized $4f$ magnetism of the Ln ion in the molecules, the magnetic communication of the molecules to their environment is expected to differ from the planar molecules with $3d$ metal center. The electronic and magnetic properties of the molecules are therefore studied in detail by x-ray magnetic circular dichroism and density functional theory, addressing the following questions:

- Are the structural properties of these three dimensional molecules similar to the planar molecules?
- Is a magnetic remanence in $LnPc_2$ molecules detectable on a timescale of x-ray absorption measurements, when the molecule is in contact with a surface?
- Can the magnetization of the $LnPc_2$ molecules be stabilized on ferromagnetic substrates? What is the coupling mechanism, the coupling energy and the communication mechanism between the localized $4f$ electrons and the substrate? What is the effect of different magnetic anisotropies of the molecules and the substrate on the coupling mechanism? Is the coupling anisotropic?
- Can the coupling be tailored by different Ln ions, substrates and interlayers?

2. Magnetism and molecular systems

2.1. Magnetic anisotropy and thin film ferromagnetism

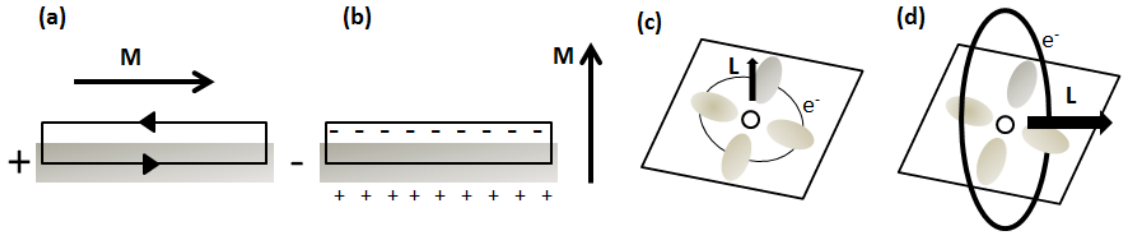

Figure 2.1.: Large, planar homogeneously magnetized sample perpendicular (a) or parallel (b) to the external field. The path integral (a) and the surface integral (b) are sketched for the application of Stoke's and Gauss' Theorem, respectively. In (c) and (d) the origin of the magnetocrystalline anisotropy is illustrated as consequence of orbital quenching.

The magnetic anisotropy in a ferromagnetic sample can originate from several sources, not only from the intrinsic properties of the sample, but also from external influences, e.g. electric field or mechanical strain. The two most common contributions that set the easy and hard magnetic axes of a sample are the shape anisotropy and magneto-crystalline anisotropy (MCA) [43]. The origin of the shape anisotropy is the demagnetization field $\boldsymbol{H}_d$ in a non-spherical sample,

$$\boldsymbol{H}_d = \frac{1}{\mu_0}(\boldsymbol{B} - \boldsymbol{M}) \tag{2.1}$$

with $\boldsymbol{B}$ the magnetic induction and $\boldsymbol{M}$ the magnetization. The demagnetization field is strongly related to the sample geometry. One extreme geometry, which is important in parts of this work, is a thin film. $\boldsymbol{H}_d$ is nearly zero for an in-plane magnetization, but largest for out-of-plane magnetization. Hence, most thin films have an in-plane easy magnetic axis. In figure 2.1 (a) and (b) this is demonstrated in a simplified picture with the principle of a magnetic surface charge using the

nomenclature of reference [43]. If $\boldsymbol{M}$ is in-plane, the sketched line integral path is according to Stoke's theorem

$$\oint \boldsymbol{H} \cdot d\boldsymbol{l} = \int (\boldsymbol{H}_s - \boldsymbol{H}_d) \cdot d\boldsymbol{l} = 0 \tag{2.2}$$

and therefore $\boldsymbol{H}_s = \boldsymbol{H}_d$, with the magnetic field inside $\boldsymbol{H}_s$. Since the surface charges, generating $\boldsymbol{H}_s$, are far apart, $\boldsymbol{H}_s$ must be small. On the other side, the surface integral in figure 2.1 is according to Gauss' theorem

$$\int\int (\boldsymbol{B}_i - \boldsymbol{B}_o) \cdot \boldsymbol{n} dS = 0 \qquad \Rightarrow \boldsymbol{B}_i = \boldsymbol{B}_o \tag{2.3}$$

where $\boldsymbol{B}_i$ and $\boldsymbol{B}_o$ are respectively the magnetic inductions inside and outside the material. $\boldsymbol{B}_\perp$ must be continuous at the surface, implying a large stray field $\boldsymbol{H}_d = -\boldsymbol{M}/\mu_0$. However, there are examples of out-of-plane easy magnetic axes, even for the thin film geometry, e.g. Ni/Cu(100) (see chapter 5.1). In these systems the MCA can overcome the shape anisotropy. The primary source for the MCA is the spin-orbit-coupling (SOC) which couples the isotropic spin moment to an anisotropic lattice [44]. Once again the example of the thin film should describe the anisotropy mechanism. In a very simple picture of a free-standing monolayer, the out-of-plane orbit of the electrons is free, while the in-plane orbit is quenched. Hence, the orbital moment is larger in the bonding plane than perpendicular to it. The fortunate circumstance that the shape anisotropy and the magneto-crystalline anisotropy are competing with each other enables the possibility to engineer the preferred magnetization direction (see chapter 5.1).

2.2. Molecular magnetism

2.2.1. Ligand field theory

Models to describe transition metal complexes have been developed for a century [45] and were really improved in the 1950s with the ligand field theory (LFT). The LFT describes certain molecules that can consist of many atoms by taking advantage of symmetries and the non-equivalency of the central atom with regards to the symmetric surrounding organic ligands. Instead of taking into account each atom, the ligands are considered just as negative charges, symmetric around the positive charged central ion. This approximation makes the LFT a method requiring relatively minor numerical effort [46]. As result of the perturbation coming from this ligand field (LF), the properties of the central ion are changes. The formalism to describe it, is the perturbation theory [47]. The basic concept of this approximation is to replace a complicated Hamiltonian $\boldsymbol{H}$ by a slightly simpler one $\boldsymbol{H}_0$, for which the Schrödinger equation

$$\boldsymbol{H}\Psi = E\Psi \tag{2.4}$$

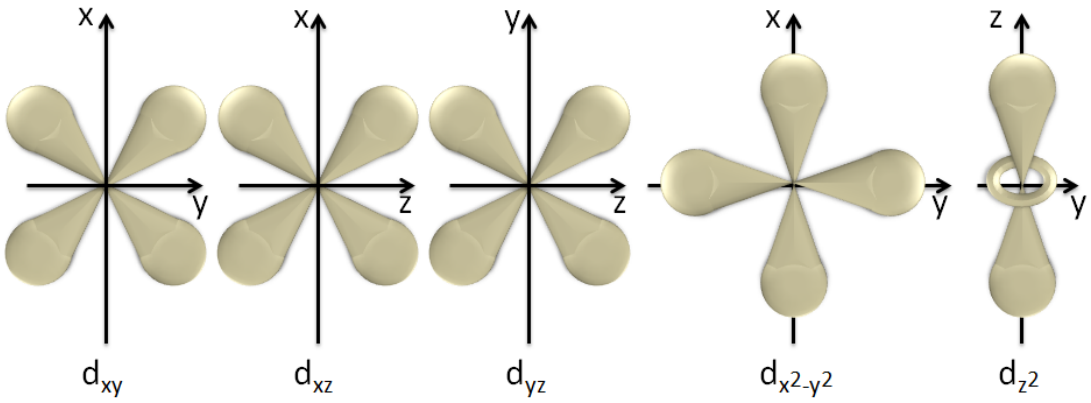

Figure 2.2.: Sketch of the five different d orbitals. Note that the axes vary depending on the orbitals' orientation.

can be solved. The error made due to this approximation is then compensated by adding a small perturbation $\boldsymbol{H}_1$. In case of the LF $\boldsymbol{H} = \boldsymbol{H}_0 + \boldsymbol{V}_{LF}$, where $\boldsymbol{H}_0$ is the Hamiltonian for the free central ion and $\boldsymbol{V}_{LZ}$ is the LF Hamiltonian. As consequence of this LF the $3d$ states, which are degenerated for the free ion, split up into different energy levels. The amount and direction of the splitting depends on the specific symmetry and strength of the LF. The splitting of atomic energy levels induced by an electric field is also known as Stark effect.

Figure 2.2 shows the five different $3d$ orbitals, which are degenerated for a free ion. In figure 2.3 the splitting is illustrated for three different LFs with high symmetry, each sketched above the energy levels [48]. For an octahedral LF the d levels split into e_g (corresponding to the degenerated $d_{x^2-y^2}$ and d_{z^2}) and t_{2g} (corresponding to the degenerated d_{xy}, d_{xz} and d_{yz}). Lowering the symmetry by removing the top and bottom ligand charge (tetragonal distorted), causes further splitting into four different levels, where only d_{xz} and d_{yz} remain degenerated for symmetry reasons. In the limiting case, in which the ligand charges are infinite away from the center, the central ion is surrounded only by a two dimensional LF (square plane), leading to a larger total splitting and crossing of the levels d_{xy} and d_{z^2}.

The cancellation of the degeneration has a direct impact on the magnetic properties of the central ion, which can be explained based on the example Fe^{2+}. Fe^{2+} has the electronic configuration $3d^6$. According to Hund's rules, five of the electrons occupy the five levels in a parallel alignment, while the sixth one has to be antiparallel following the Pauli exclusion principle, leading to a $S = 2$ spin state. However, the splitting of the energy levels, e.g. in an octahedral LF, counteracts the energy minimization by occupation according to Hund's rules. If the energy splitting is large, the favorable occupation is the complete filling of the t_{2g} level

with three spin up and three spin down electrons and leave the e_g level completely empty. This results in a $S = 0$ configuration and is called low spin state. If the splitting is small, the favorable occupation can correspond to the one of the free ion, resulting in the high spin state ($S = 2$). A third occupation is possible in case of the square plane LF. The $d_{x^2-y^2}$, which is significantly higher in energy remains unoccupied, d_{xy}, d_{yz} are filled, each with one spin up and one spin down electron, d_{z^2} and d_{xy} are single-occupied, leading to a $S = 1$ intermediate state.

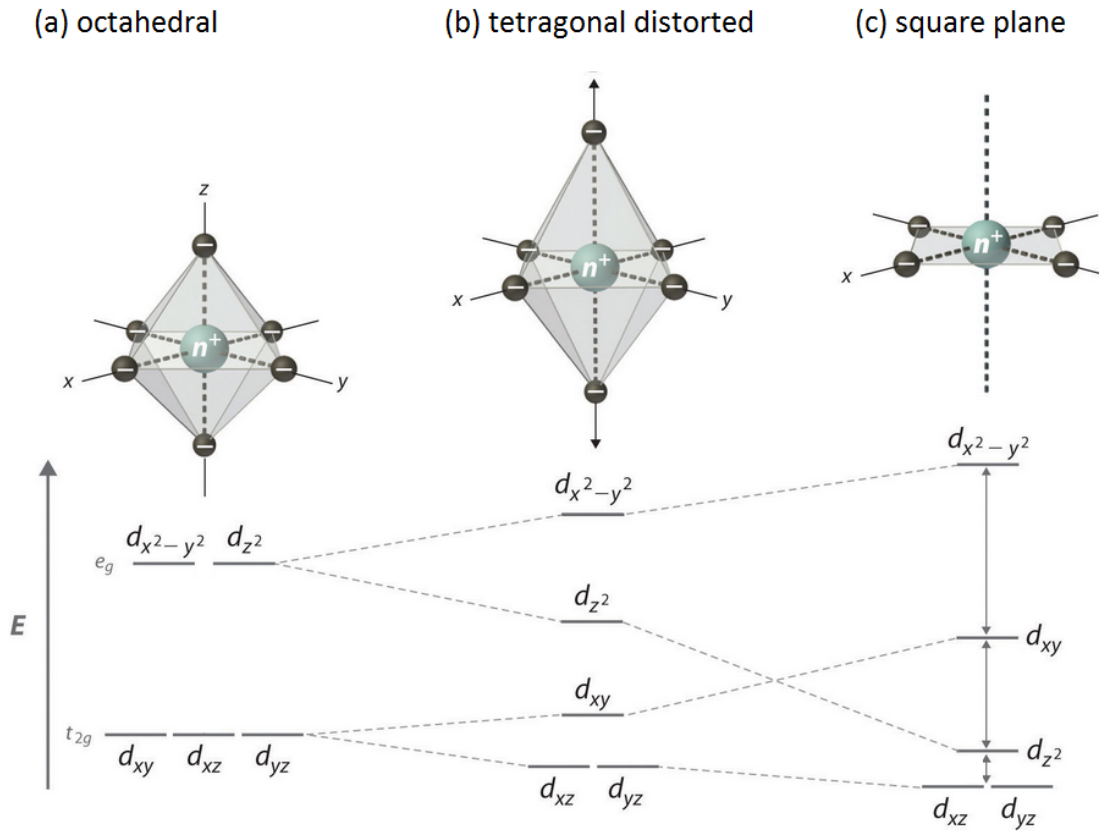

Figure 2.3.: LF splitting of the 3d orbitals in (a) octahedral, (b) tetragonal distorted and (c) square plane geometrie [48].

2.2.2. Superexchange

To describe spin hybrid systems, it is crucial to determine the magnetic interaction mechanism. The magnetic interaction is not necessary occurring directly between the molecules' central ion and the surface atoms, but can be mediated through the non-magnetic ligand (superexchange) or a combination of those. Apart from the atoms taking part in the magnetic interaction, one also has to determine the

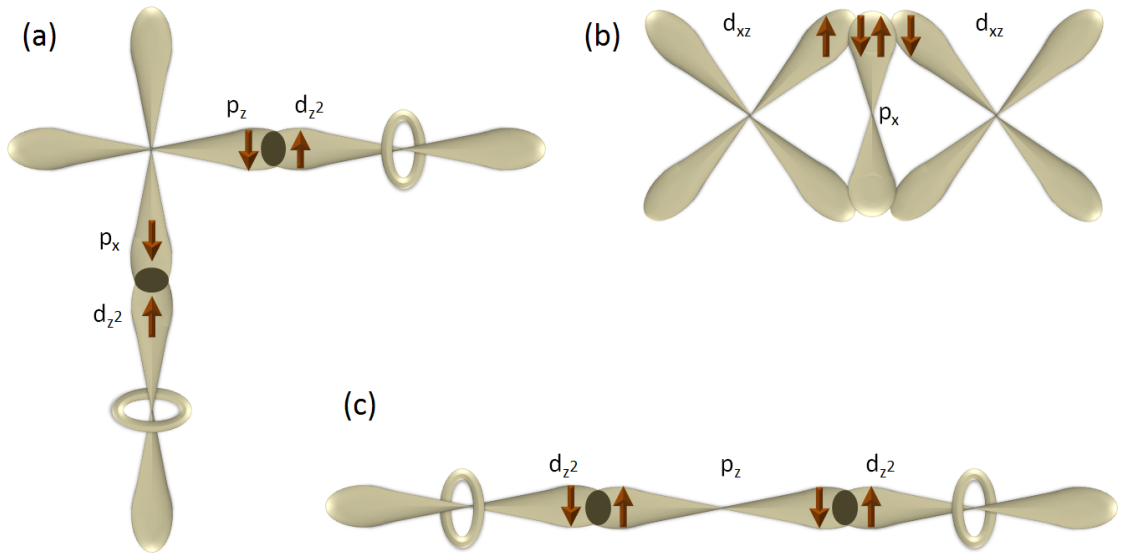

Figure 2.4.: Illustration of the exchange mechanisms between occupied orbitals based on three simple examples: (a) 90° ferromagnetic, (b) and (c) 180° antiferromagnetic.

involved orbitals from the atoms, which can vary for similar systems. Three possible superexchange pathways are shown in figure 2.4. In (a) a 90° superexchange is shown between two d_{z^2} orbitals mediated by p_x and p_z orbitals. The metal's d_{z^2} electron spin polarizes the electron spin in the ligand's p_z orbital, which is parallel aligned to the p_x spin. This electron, in turn, polarizes the second metal's electron spin. This pathway results in a ferromagnetic coupling between the two metal atoms. On the other hand, the pathways (b) and (c) represent 180° superexchange interactions and lead to an antiferromagnetic coupling as consequence of the Pauli exclusion principle. Since the mediation of the interaction via the ligand atom is only within one orbital, e.g. p_z, the two spins must be antiparallel and hence, the two metal atoms are antiferromagnetically coupled. The difference between (b) and (c) lies in the interaction strength, which is stronger in the σ-type (c) than in the π-type (b) [49]. Which one of the superexchange types is present, also depends on the occupation of the orbitals and is summarized by the Goodenough-Kanamori rules [50–52]:

- The 180° superexchange between filled or between empty orbitals is strong and antiferromagnetic.

- The 180° superexchange between one filled and one empty orbital is weak and ferromagnetic.

- The 90° superexchange between filled orbitals is weak and ferromagnetic.

2.2.3. Single molecule magnets

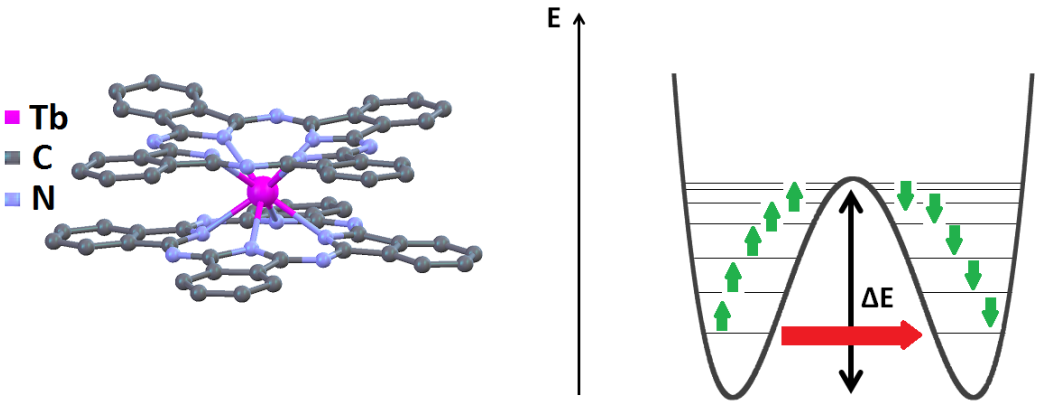

Figure 2.5.: Sketch of a $TbPc_2$ molecule (left) and the double-well potential at zero field with the energy barrier ΔE. The green arrows represent thermal spin relation while the red arrow shows the spin quantum tunneling.

About twenty years ago, the existence of single molecule magnets (SMMs) was discovered [37]. SMMs are discrete molecules that show magnetic hysteresis without the need of long-range interaction. The occurrence of magnetic hysteresis without long-range interaction, as it is the case for a ferromagnet, is a consequence of an energy barrier ΔE (figure 2.5), high enough to prevent spin-reorientation. A description of the mathematical properties is given by a spin hamiltonian [10]:

$$\boldsymbol{H} = DS_z^2 + E(S_x^2 - S_y^2) + g\mu_B\mu_0\boldsymbol{S}\cdot\boldsymbol{B}, \tag{2.5}$$

where S_x, S_y and S_z are the spin components, D and E are the magnetic anisotropy constants and $g\mu_B\mu_0\boldsymbol{S}\cdot\boldsymbol{H}$ is the Zeemann energy in an applied magnetic field B. The quadratic dependence of equation 2.5 is clearly illustrated in the sketch of the parabolic shape of the energy landscape in figure 2.5.

A special type of single molecule magnet addressed in this work in chapter 5, is bis(phthalocyaninato) Lanthanide ($LnPc_2$) [53]. Figure 2.5 shows a sketch of $TbPc_2$, a molecule consisting only of one Tb center surrounded by organic ligands. The single molecule behavior is a consequence of the single ion anisotropy [39]. Such molecules are characterized by large unquenched magnetic moments and high magnetic anisotropies. Unfortunately all SMMs have in common that the hysteretic behavior vanishes above a certain temperature, in general only a few K. Above this so-called blocking temperature, the SMM behaves like a paramagnetic molecule. However, at very low temperature, the spin relaxation time becomes large and spin quantum tunneling dominates (see figure 2.5), leading to steps in the hysteresis curve if the experimental method is fast enough, e.g. AC susceptibility [40].

Single molecule magnets are defined by the bistability of the ground state, a large energy difference between the ground state and the first excited state and a large spin-orbit coupling. The doubly-degeneracy of the ground state with a high magnetic quantum number $\pm m_J$ [39] and the large separation between the ground state and the first excited state is illustrated in figure 2.5. The energy difference between these stated defines the energy required to relax the spin.

The shape of the f electron charge cloud varies strongly from prolate to oblate as consequence of the strong angular dependence of the f orbitals. The occupation of the f orbitals can be determined according to Hund's rules, enabling to easily determine the shape of the electron clouds for each Ln element (figure 2.6 (a)).

In addition to the single-ion anisotropy, the crystal field of the $LnPc_2$ double-decker molecule plays a major role for the magnetic anisotropy. The symmetry of the sandwich structure of the molecules with the two pc ring and the Ln ion in between maximizes the anisotropy of an oblate ion, such as Tb or Dy, because the electron density is concentrated above and below the molecular plane. To minimize the repulsive contacts between ligand and f electron charge clouds, the bistable ground state is parallel or antiparallel to the molecular axis (figure 2.6 (b). For a prolate ion, such as Er, the f electron density is axially located (figure 2.6 (b)). Therefore $ErPc_2$ with the prolate Er ion does not exhibit an axial anisotropy, but an in-plane anisotropy.

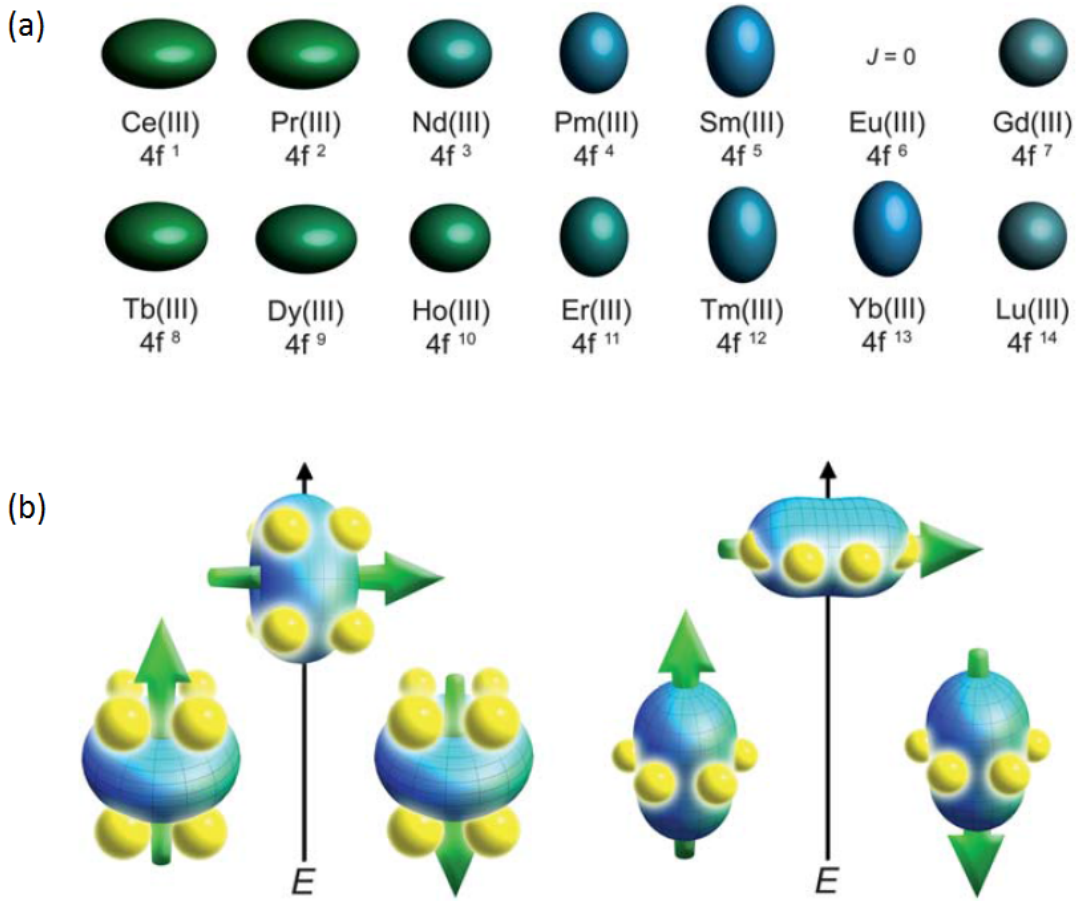

Figure 2.6.: (a) Prolate, spherical or oblate shape of the $4f$ electron distribution according to quadrupol approximations of the Ln^{3+} ions. (b) Illustration of the oblate and prolate elctron density in different crystal fields, minimizing or maximizing the $m_J = J$ state. (figures taken from J. D. Rinehart and J. R. Long, Chem. Sci. 2, 2078 (2011). [39]).

3. Experimental Details

3.1. Sample preparation and characterization

3.1.1. Ultra high vacuum

For the presented investigations on surface-molecule interaction, ultra high vacuum (UHV) conditions with a base pressure of $p < 10^{-9}$ mbar are absolutely necessary. The *in situ* preparation of a sample takes no more than a few hours and the individual preparation steps, e.g. depositing magnetic films or molecules, does not take more than some minutes. However, this period is long enough that the sample can be contaminated by adsorbing any residual gas in the UHV at a pressure $> 10^{-9}$ mbar. The number of atoms from the residual gas that hit the sample per time unit is linear with the density of atoms. Even in a UHV pressure of 10^{-9} mbar the number of atoms hitting the sample is large enough to build a complete layer within one hour [54]. The actual amount on the surface depends on the sticking coefficient which is close to one at room temperature considering that the residual gas is mainly CO and the investigated samples are Cu, Co or Ni. In our experiments the base pressure during preparation is 2 - 5×10^{-10} mbar, giving us the opportunity the produce very clean, well-defined samples.

Single crystals, e.g. Cu and Ni, can be cleaned from contaminations on the surface by Ar^+ sputtering under UHV conditions. Ar gas of high purity is dosed typically with a partial pressure of 10^{-6} - 10^{-5} mbar and ionized by electrons from a filament in the sputter gun. Depending on the material, the surface orientation and the amount of expected impurities, the Ar^+ acceleration voltage is chosen to be 500 - 3000 V. The Ar^+ ions hit the sample under an incidence angle of 45 - 60° with regards to the surface and remove the atoms on the surface. After some time the upper layers are ablated. However, due to the bombardment with Ar^+ ions, the surface becomes rough and needs to be annealed by heating the crystal to temperatures below the melting point, e.g. $T = 900$ K for Cu. For a single crystal with a high amount of contamination, e.g. after exposition to air, this sputter-anneal procedure needs to be repeated several times to guarantee a clean and smooth surface.

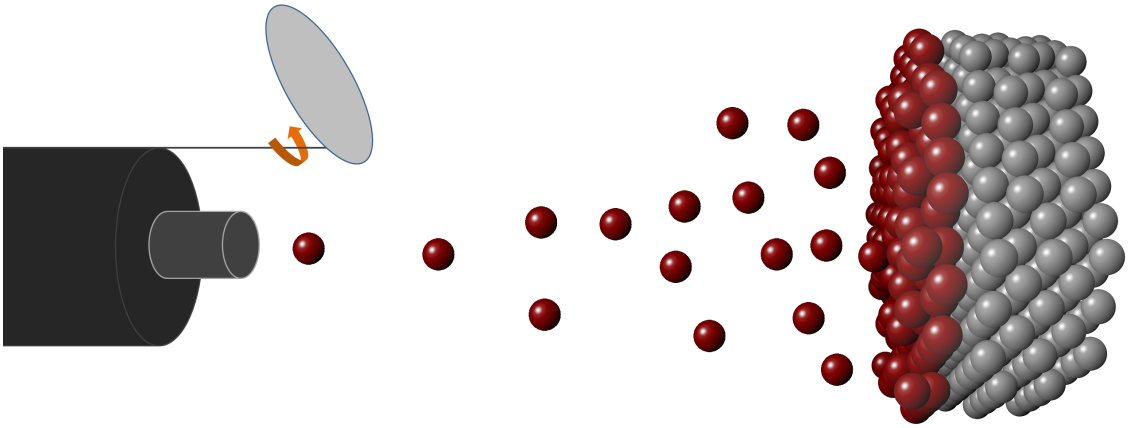

Figure 3.1.: Graphical presentation of the molecular beam epitaxy. The evaporated material grows epitaxially on a certain substrate. The deposition can be started and finished by opening or closing the shutter.

3.1.2. Molecular beam epitaxy

Molecular beam epitaxy (MBE) is an extremely precise technique for producing ultrathin, epitaxial films (figure 3.1). For the purposes of this work, the epitaxy and precision is crucial, since it defines both, the magnetic characteristics, e.g. magnetic anisotropy, and the surface structure. Two different ferromagnetic films are produced in this work, 5 ML Co and 15 ML Ni, each on Cu(100). High purity (> 99 %) rods of Ni and Co of ≈ 50 mm length and 2 mm in diameter are placed into two of the three positions of the water-cooled metal evaporator. Each position can be controlled individually. A filament produces free electrons at a current of 2 A, while a voltage of 1 kV is applied to the rod. Locally the rod is heated and evaporates metal ions onto the sample with a low rate of less than 1 ML/minute. Opening or closing the shutter starts or ends the evaporation process. The rate can be calibrated with a micro balance or monitoring MEED (medium energy electron diffraction) oscillations. During evaporation, the rate can be checked with the flux, measured in the metal evaporator or more precisely with the current between sample and ground that is a measure of deposited metal ions per second. A crosscheck of the final thickness can be performed by comparing reference spectra with Auger electron Spectroscopy (AES) or XAS, if the film is prepared at the synchrotron.

3.1.3. Surface Characterization

Even though the preparation mechanisms are very precise and reliable, a characterization of the surface is necessary to determine the sample geometry and confirm

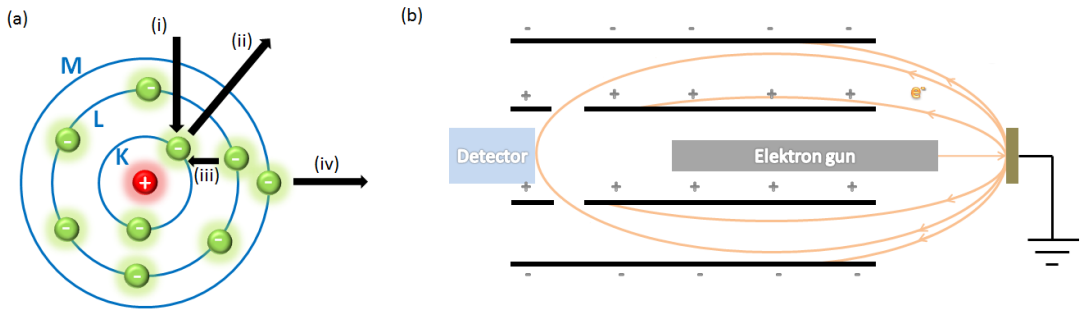

Figure 3.2.: (a) Illustration of the Auger process in an atom with three energy levels K, L, M and (b) a sketch of a cylindrical mirror analyzer.

the successful preparation. Very common and important methods to determine surfaces in terms of elemental composition, adsorption geometry and latteral ordering are AES, x-ray photoelectron spectroscopy (XPS), low energy electron spectroscopy (LEED) and scanning tunnel microscopy (STM). These four techniques have been used to characterize the samples investigated in this work and will be described briefly in the following.

AES

The Auger-effect, discovered by Lise Meitner [55] and named after Pierre Auger [56], is a non-radiative process, illustrated in figure 3.2 (a). An electron from the inner K level is struck out (ii) by external excitement, e.g. an electron (i). In the next step (iii) the resulting hole is occupied by an electron from the higher level L. The released energy in this transition is transferred non-radiatively to another electron on level M, which has enough energy to overcome the binding energy and leaves the atom (iv). The kinetic energy of this Auger electron

$$E_{Aug} = |E_K - E_L - E_M| \tag{3.1}$$

is element-specific and independent of the exciting energy. Therefore the Auger spectrum is characteristic for the elements which are contained in the investigated sample, making AES a suitable method to detect contamination of the sample. The exciting electrons' energy is normally between 1-5 kV and the escape depth of the Auger electrons is typically only a few monolayers. Hence, AES is very precise for the contamination on the surface, not to detect impurities within the sample volume.

To determine the energy of the Auger electron, a cylindrical mirror analyzer (CMA) is used, illustrated as cross-section in figure 3.2 (b). The CMA consists of two concentric metal cylinders. Applying a voltage between the two cylinders, positive charge to the inner one, negative charge to the outer one, will cause an electric field, pointing to the outer cylinder. Negatively charged electrons will be attracted to the inner

one, respectively. Electrons from an electron gun are accelerated in a potential of some kV towards the sample and diffracted electrons, secondary electrons and Auger electrons enter the cavity between the two cylinders. At a certain voltage applied to the cylinders, only the electrons with a specific energy will pass the exit slit and reach the detector. Electrons with higher energy will impact on the outer, electrons with lower energy on the inner cylinder. A channeltron is used for the amplification of the small signal coming from the Auger electrons. To separate the detection of the Auger electrons from the large background of secondary electrons, a lock-in amplifier is used to differentiate the signal.

XPS

XPS is a similar method to AES and is also used to determine the chemical composition of a material. While for the AES accelerated electrons are used to excite electrons in the atoms, for XPS photons from an x-ray tube are used. The excitement of an electron with a photon is based on the photoelectric effect [57]. The ejected electron is detected and its kinetic energy E_{kin} is measured. However, the kinetic energy of the secondary electron depends on the energy of the incident photon $E_{h\nu}$ in opposite to Auger electrons:

$$E_{kin} = E_{h\nu} - E_{bond} - \Phi. \tag{3.2}$$

Φ is a work function, a constant value of only some eV, depending on the material and the spectrometer itself [58]. The analysis of energy is normally done with the help of a concentric hemispherical analyzer (CHA), operating similar to the CMA. The small signal of the secondary electrons is amplified with channeltrons. In addition to the determination of the elements of the sample, XPS is capable of distinguishing between different states of one element, e. g. graphene or carbide [59].

LEED

While AES and XPS deliver reliable information about the chemical composition of a material's surface, they cannot determine geometries and the quality of a surface concerning the smoothness. Therefore LEED is a complimentary method to receive these information. The diffraction of electrons on a crystal lattice can be described by Bragg's law [60]

$$n\lambda = 2d\sin(\theta) \tag{3.3}$$

with the diffraction order n, the atomic distance d, the de Broglie wavelength $\lambda = \frac{h}{p}$ [61] and the Bragg angle θ. An equivalent to the Bragg's law is the Laue

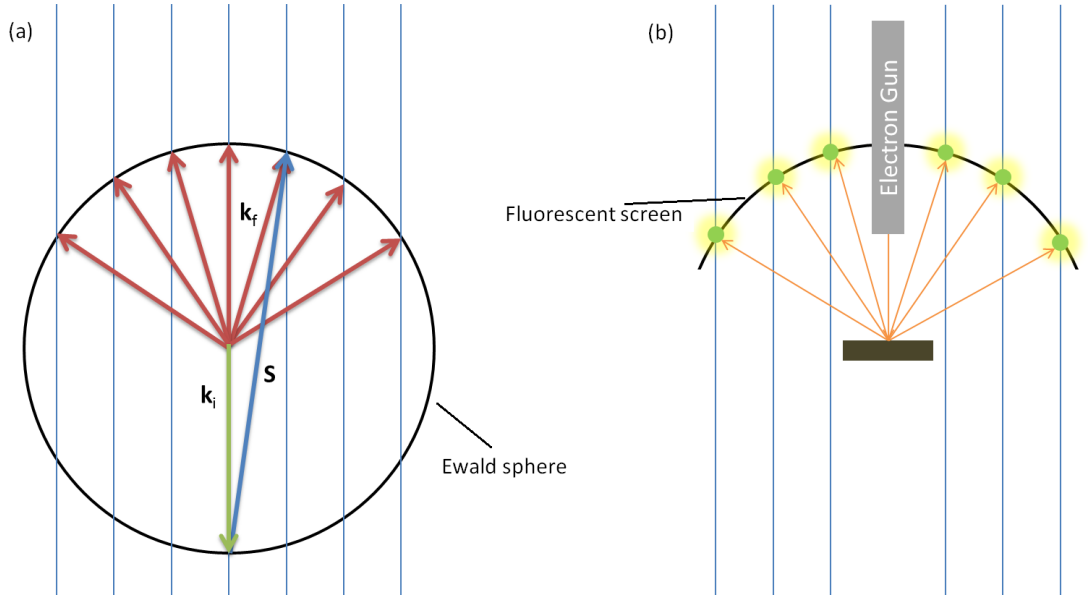

Figure 3.3.: (a) Ewald sphere in two dimensions. To detect intensity, the difference between the initial and scattered wave vector must be a reciprocal lattice vector $\Delta\mathbf{k} = \mathbf{S}$. (b) Schematic structure for LEED measurements.

equation in the reciprocal space, when $\mathbf{S}$ is a lattice vector of the reciprocal lattice

$$\Delta\mathbf{k} = \mathbf{S}, \tag{3.4}$$

with $\Delta\mathbf{k} = \mathbf{k_f} - \mathbf{k_i}$ the difference between the wave vectors before and after the diffraction. We only consider elastically diffracted electrons, so $|\mathbf{k_i}| = |\mathbf{k_f}|$. A graphical explanation is given by the Ewald sphere, which can be reduced to a 2-dimensional sphere, because only the surface is considered, see figure 3.3 (a). In the two dimensional case, lattice points are replaced by rods, since the third dimension is degenerated. The construction: Draw a vector $\mathbf{k_i}$ with the end on a rod and add a circle with the radius $|\mathbf{k_i}|$. Wherever $\mathbf{k_f}$ and the rods intersect, intensity will be detected. The Ewald sphere is a helpful construction, because it can be easily transferred to the experiment, sketched in figure 3.3 (b). The electrons from the electron gun are accelerated to the sample, scattered at the surface and detected on the fluorescence screen.

The electric signal that has to be detected is small in the described methods (AES, XPS, LEED). A possibility to amplify the signal is the use of a channeltron, figure 3.4 (a). The operating principle of a channeltron is very simple. The incident electron is accelerated by an electric field due to an applied voltage of a few kV. When the electron hits the wall of the channeltron, a larger number of secondary electrons are emitted from the wall material. By consecutive hits, the initial electron has caused an electron avalanche. A micro channel plate (MCP),

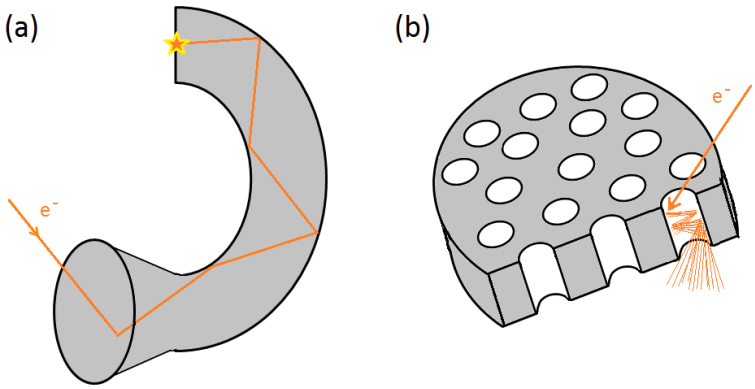

Figure 3.4.: Simplified illustrations of a channeltron (a) and an MCA (b). The path of the electrons is sketched. The electron avalanche is shown only in (b) for a better presentation.

figure 3.4 (b), consists of many such channels multiplying the electrons. In chapter 4 LEED results from an MCP-LEED are shown. This enables performing LEED with a reduced intensity of the electron beam and hence a very small sample current to protect the surface structures, e.g. the integrity of molecules [62].

STM

A scanning tunnel microscope, invented by Gerd Binnig and Heinrich Rohrer in 1982 [63], who were awarded with the Nobel prize in 1986 [64], is able to display surfaces on an atomic level. STM, like LEED, can be considered as complementary method to AES or XPS. But there are several advantages for STM compared to LEED. STM images the surfaces in the real space and does not only deliver information about periodic geometries, but can also determine the integrity of molecules, adsorption sites and the adsorption height of atoms and molecule, see chapter 5. However, an STM is much more sensitive and for the best possible results it needs to be operated with great care under special optimized, low-noise conditions. These conditions are almost impossible to achieve for the purposes of this work, given the fact that the samples are *in situ* prepared and measured at the synchrotron. Therefore the here presented STM results are not of the highest quality and the use of LEED is easier and much quicker to qualify the preparation outcome.

The operation of an STM is based on the tunnel effect. Certain areas of the sample can be scanned and an image of the surface can be calculated from the tunneling current. The tip has ideally a single atom at the end (figure 3.5), delivering the highest resolution. The STM tip, e.g. made of tungsten, is moved towards the sample until a distance between the tip and the sample is only a few Å. The precise movement of the tip is piezoelectrically controlled. At this small distance, the wave functions of the electrons in the tip and in the sample overlap

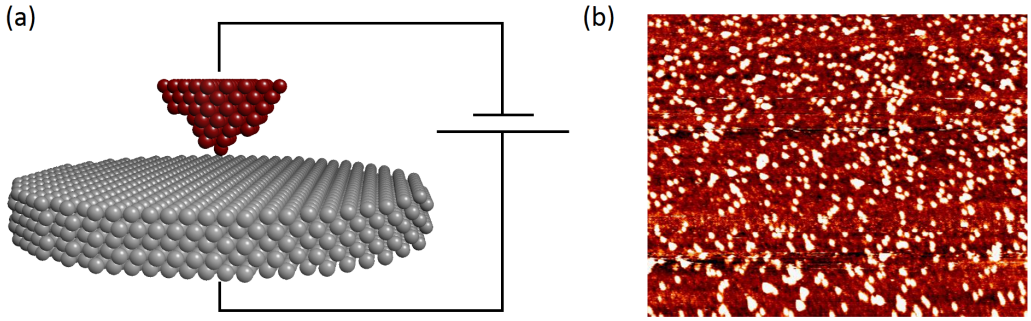

Figure 3.5.: Sketch of an STM tip over a surface (a) and an STM pattern (200x200nm^2) of $TbPc_2$ molecules on a Ni(111) surface [65].

enough that they can tunnel either way through the barrier with height eU_B. By applying a voltage, a tunneling current can be detected, which is exponentially depending on the distance d between the surface and the tip [58].

$$I \propto \exp\left(2\kappa d\right), \tag{3.5}$$

$$\kappa = \frac{2m}{\hbar^2}\left(eU_B - E\right). \tag{3.6}$$

E is the energy of the state from which tunneling occurs.

3.2. Cryogenic devices used for the sample cooling

Investigations of the magnetic properties of paramagnetic molecules and single-molecule magnets usually require extremely low temperatures. Depending on the desired temperature, the use of special cooling devices are necessary, briefly described in this section. A more detailed and theoretical description of the devices can be found in references [66, 67].

3.2.1. Bath cryostat

A very common system is a conventional liquid helium cryostat, used e.g. at the beamlines ID08, ESRF and UE46, BESSY II. Natural He (>99.999% ^{4}He) is liquid at temperatures below 4.2 K at atmospheric pressure and often used for sample cooling. One has to distinguish between cooling down from room temperature and holding the sample at a low temperature. For the cooling down process, it is important

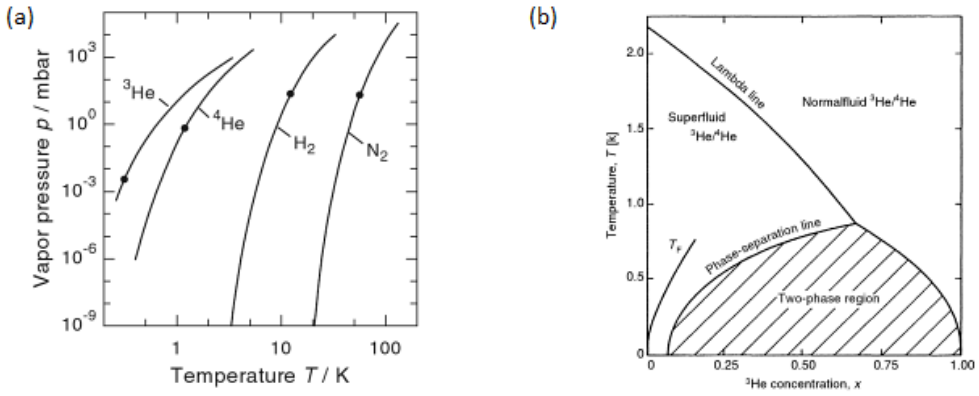

Figure 3.6.: (a)Vapor pressure of different cryogenic liquids as a function of temperature. The points indicate the lowest temperature that can be achieved in practice with moderate efforts [66]. (b) Phase diagram of liquid ^{3}He-^{4}He mixtures at saturated vapor pressure [67].

not only to use the latent heat (L = 2.6 kJ/l), but also the enthalpy change of the He gas, which is almost two orders of magnitude higher between 4.2 K and 300 K (200 kJ/l) [66, 67]. In the stationary state the heat transferred from external sources has to be compensated by the cooling power of the cryoliquid. In this state the cooling power basically comes from the evaporation of liquid He. The cooling power provided by the enthalpy change of the cold gas can be used to cool down the environment, e.g. the walls of the cryostat [67]. One experimental challenge for such a device - that also applies for the latter described systems - is a good thermal contact to the sample and a good thermal isolation to the 300 K warm environment. This is not only important to reach the lowest possible sample temperatures, but also to cap the costs, since liquid He is expensive in comparison to e.g. liquid N. Hence, aside from thermal isolation by vacuum, a shield of liquid N in a tank surrounding the He bath is often used.

3.2.2. Evaporation cryostat

To reach temperatures below 4.2 K, some additional technical effort is required. Pumping on the He bath can lower the temperature down to ≈ 1.3 K [66]. Assuming an equilibrium of the liquid and gas phases of He in a cryostat, Clausius-Clapeyron-Equation [68, 69] gives

$$\frac{dP}{dT} = \frac{S_g - S_l}{V_g - V_l} \tag{3.7}$$

with S_g, S_l the entropies in the gas and liquid phases and V_g, V_l the volumes, respectively. $V_g >> V_l$, the latent heat is $L = T(S_g - S_l)$ and the ideal gas law gives $PV = RT$, so that

$$\frac{dP}{dT} = \frac{LP}{RT^2}. \tag{3.8}$$

The latent heat L is nearly temperature-independent [67], hence the solution of the first order differential equation delivers

$$\frac{P}{P_0} = \exp\left[\frac{L}{R}\left(\frac{1}{T_0} - \frac{1}{T}\right)\right]. \tag{3.9}$$

This equation demonstrates that the temperature can be cooled down by just reducing the pressure. However, the exponential behavior also explains, why there must be an experimental limit of $T \approx 1.3$ K, also illustrated in figure 3.6 (a), showing the vapor pressure as a function of temperature. The cooling power $\dot{Q}$ in a pumped-on liquid bath is given by $\dot{Q} = \dot{n}\dot{L}$, with $\dot{n}$ particles/time moved to the vapor phase [67]. It follows from equation 3.9

$$\dot{Q} \propto \exp\left(\frac{L}{RT}\right). \tag{3.10}$$

Aside the cooling power, the limit of temperature is given by heat coming from various sources, e.g. heat conduction through the tubes, radiation from warmer parts of the apparatus and heat generated by the experiment [66]. That is why usually a sample temperature of $T \approx 2$ K is reached in a pumped cryostat at the synchrotron, e.g. DEIMOS, SOLEIL.

3.2.3. Dilution refrigerator

Cooling below 1 K is not possible with ^{4}He, but ^{3}He can be used, because it has a significantly larger vapor pressure than ^{4}He at the same temperature, see figure 3.6. The ratio P_3/P_4 is 74 at 1 K and 1000 at 0.5 K [67]. A problem regarding the use of ^{3}He is the rare natural occurrence and consequently an extremely high price of > 1000 € per liter ^{3}He gas, continuously rising in the last number of years [70]. However, the accessible final temperature of a ^{3}He cryostat is about 0.3 K. Even lower temperatures can be reached by using a ^{3}He-^{4}He dilution refrigerator, already developed in the 1960s [71, 72], whose setup and principle functionality are described in the following paragraph according to references [66, 67, 73, 74]. The operation of the dilution refrigerator can be explained on the basis of figure 3.7, showing a simplified sketch of the dilution refrigerator and the ^{3}He circuit, starting top left: The precooled and condensed ^{3}He passes a heat exchanger, which is in thermal contact with the still at $T \approx 0.7$ K. After further precooling the liquid ^{3}He enters the upper phase in the mixing chamber. The appearance of two separated phases is the clue

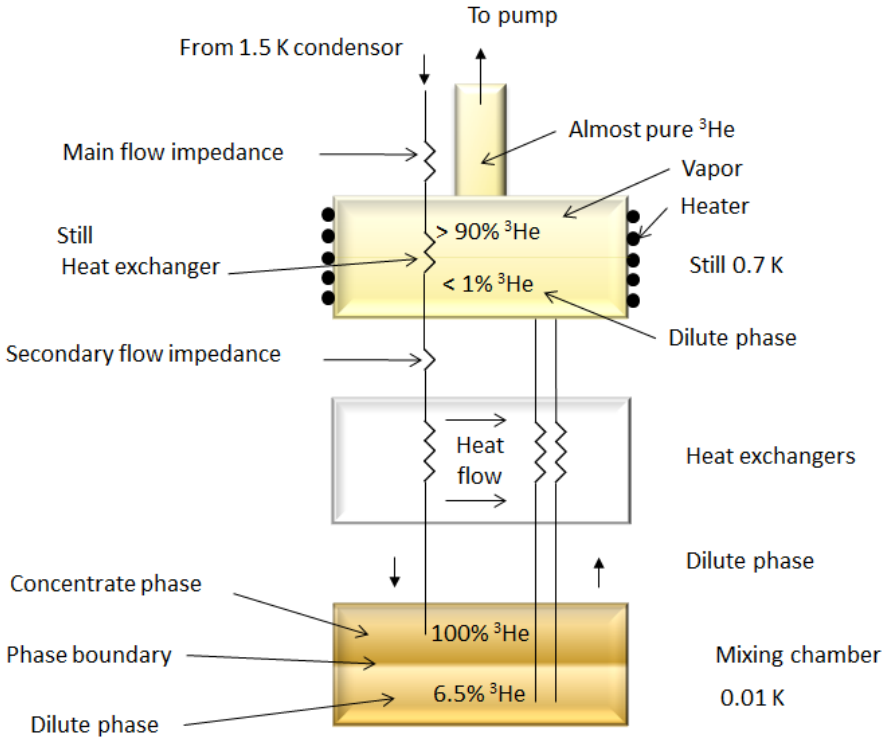

Figure 3.7.: Simplified sketch of a dilution refrigerator (graphic created according to reference [67]).

of the dilution refrigerator (figure 3.7). Below 2.17 K ^{4}He bosons make a phase transition to the superfluid state [67], while the ^{3}He fermi liquid does not show this transition. Below 0.87 K the ^{3}He-^{4}He mixing ratio is limited and two phases coexist in the mixing chamber, a pure ^{3}He phase on top (concentrated phase) and a mixture phase below (dilute phase) with a ^{3}He concentration of 6.6% for T approaching zero. If the equilibrium concentration is disturbed by removing ^{3}He from the dilute phase, ^{3}He atoms pass from the concentrated phase into the diluted ^{3}He phase. Because of the higher potential energy of the ^{3}He in the diluted phase, this process removes energy from the liquid, whose temperature decreases. To make a continuous cooling process, the still is heated to $\approx$ 0.7 K and pumped. Because of the much higher vapor pressure, almost pure ^{3}He is pumped. The circuit is closed by condensation of the ^{3}He, which is again supplied to the mixing chamber. In principle, one can achieve a constant temperature of some mK. However, in the system that is used for x-ray absorption studies at the SLS, we could reach a stable temperature of $T \approx 300$ mK, in the described experiment $T \approx 500$ mK.

3.3. X-ray absorption spectroscopy

X-ray absorption near edge spectroscopy (XANES), extended x-ray absorption fine structure (EXAFS) and x-ray magnetic circular dichroism (XMCD) fall under the generic term x-rays absorption spectroscopy (XAS). The spectroscopy of the x-ray absorption by matter can deliver various microscopic information about the material, e.g. elemental composition, the electronic structure, atomic binding length or magnetic moments. The detection of the x-ray absorption can be executed in transmission mode, by measuring the fluorescence yield or the total electron yield (TEY). Trough out this work the investigated samples are impenetrable for soft x-rays and a transmission measurement is therefore impossible. If heavy elements are studied, fluorescence yield is preferable [75], because the cross section rises with the atomic number. The results presented here have all been recorded in TEY mode, which means that the detected sample current is the sum of all photoelectrons, Auger electrons and secondary electrons and is proportional to the absorption coefficient, if the escape depth of the electrons is small compared to the penetration depth of the photons. The escape depth of the electrons is only a few nanometers, while the penetration depth of soft x-rays is two orders of magnitude larger [76], making TEY a surface-sensitive method.

3.3.1. Interaction of electromagnetic radiation with matter

The Lambert-Beer law [77] delivers a description of the intensity I of radiation propagating in homogenous, isotropic material

$$I(x) = I_0 \cdot \exp(-\mu(E)x). \tag{3.11}$$

The attenuation coefficient μ is the sum of the molecular cross sections σ_i of the elements i per unit cell volume V [78]:

$$\mu = \frac{1}{V} \sum_{i=1}^{n} \sigma_i. \tag{3.12}$$

For anisotropic, inhomogeneous materials, μ is also position-depend. In any case, μ is characteristic for the interacting material and strongly energy-dependent. The composition of the cross-section and its energy dependence is shown in figure 3.8, using the example Pb. All contributions, namely atomic photoelectric effect, coherent scattering, incoherent scattering, nuclear-field pair production, electron-field pair production and nuclear photoabsorption, depend on the energy of the electromagnetic radiation. Here we will focus only on the soft x-ray regime $\approx 10^2$ eV - $\approx 10^3$ eV, which is the only relevant regime for the presented work. In this range, the photo-effect dominates the cross-section. Clearly visible in the cross-section are the element-specific absorption edges at the energies, which matches the required

energy to excite an electron of initial state i to a final state f. A formal description of the absorption process is given by *Fermi's Golden Rule* [79], which was originally derived by Paul Dirac [80] and later called *Golden Rule No.* 2 by Enrico Fermi. It describes the first order transition probability from i to f, induced by the electromagnetic field:

$$T_{i,f} = \frac{2\pi}{\hbar} \left|\langle f \left|H_{int}\right| i\rangle\right|^2 \delta(\epsilon_i - \epsilon_f)\rho(\epsilon_f). \tag{3.13}$$

H_{int} is a perturbing Hamiltonian, which is in the dipolar approximation [81]

$$H_{int} \propto \mathbf{p} \cdot \mathbf{A} \tag{3.14}$$

with the momentum vector $\mathbf{p}$ and the vector potential $\mathbf{A}$ ($E = -\partial\mathbf{A}/\partial\mathbf{t}$ in free space). The permitted transition from an initial state $|l, m_l, s, m_s\rangle$ into a final state $|l', m_l', s', m_s'\rangle$ is determined by the dipole selection rules:

$$\Delta l = l - l' = \pm 1 \tag{3.15}$$
$$\Delta m_l = m_l - m_l' = 0, \pm 1 \tag{3.16}$$
$$\Delta s = s - s' = 0 \tag{3.17}$$
$$\Delta m_s = m_s - m_s' = 0. \tag{3.18}$$

The spin of the electron during the absorption process is preserved ($\Delta s = s - s' = 0$), while the preservation of momentum demands that $\Delta m_l = +1$ for the absorption of a left circular polarized, $\Delta m_l = -1$ for the absorption of a right circular polarized and $\Delta m_l = 0$ for the linear polarized photon, a superposition of left and right polarized photons.

3.3.2. XANES, XLD and XMCD

With XANES the fine structures at the absorption edges, e.g. the L_2 ($2p_{1/2} \rightarrow 3d$) and L_3 ($2p_{3/2} \rightarrow 3d$) edges, are studied, which deliver information about the unoccupied states and the chemical environment. In this work we exclusively focus on the near edge regime and therefore XANES will be referred to as XAS in the following.

The x-ray linear dichroism (XLD) is sometimes also specified as x-ray natural linear dichroism (XNLD) to distinguish it from x-ray magnetic circular dichroism (XMLD), reveals the electronic distributions, especially electronic anisotropies. The XLD is defined as difference in absorption from linear vertically μ_V and linear horizontally μ_H polarized light, XLD $= \mu_V - \mu_H$. The sketch in figure 3.9 illustrates

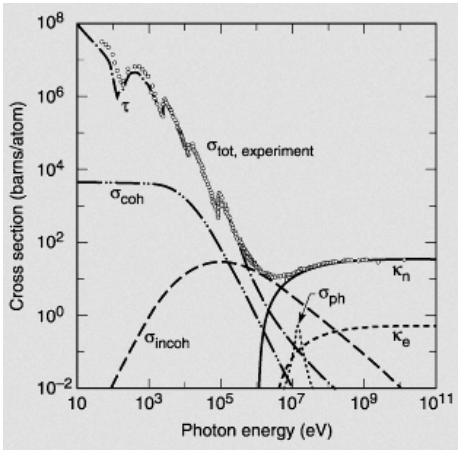

Figure 3.8.: Total photon cross section in Pb as a function of energy taken from [82], original in [83]

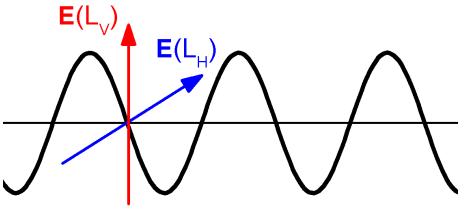

Figure 3.9.: Orientation of the electric field **E** in vertically and horizontally polarized light.

an electromagnetic wave with the two possible linear polarizations of the electric field vector **E**. In an isotropic sample, the absorption is identical and XLD = 0, while for a sample, which is anisotropic concerning the two direction of **E**, follows XLD $\neq$ 0. The results can among others be used to determine the geometry of a sample, e.g. the orientation of a molecule, see chapters 4 and 5.

XMCD spectroscopy to determine the magnetic properties of the investigated spin-hybrid systems is undoubtedly the most important measurement technique for the results presented here and will therefore be explained in more detail. The development of synchrotron radiation sources made XMCD studies possible. Hence it is a relatively new method, theoretically predicted in 1975 [84] and experimentally demonstrated in 1987 [85]. The strengths of XMCD in comparison to other magnetization methods are

(i) the extremely high sensitivity of synchrotron radiation, giving the possibility to study even fractions of a monolayer,

(ii) the element-selectivity, enabling to distinguish between the magnetization of different elements in one sample,
(iii) the quantitative determination of spin and orbital moments for specific systems.

In a one-electron picture a simple two step model can describe the origin of the XMCD effect based on a $3d$ transition metal, e.g. Fe. Figure 3.10 shows the spin-orbit-split core-level $2p_{3/2}$ and $2p_{1/2}$ with spin-up electrons $\uparrow$ left in the $2p_{3/2}$ and spin-down electrons $\downarrow$ right, and vice versa in the $2p_{1/2}$ level. The excitation probability of a polarized photon with positive +1 helicity or negative -1 helicity is determined by the Clebsch-Gordon coefficients. By summing up all possible transitions, it comes out that 62.5% electrons from the $2p_{3/2}$, excited by a +1 photon, have the spin $m_s = +1/2$, while 37.5% carry the spin $m_s = -1/2$, respectively. The spin polarization of the $2p_{1/2}$ is opposite: 75% of the electrons excited by a +1 photon have the spin $m_s = -1/2$ and only 25% $m_s = +1/2$. This spin-polarized absorption does not depend on the $3d$ state and is also valid for nonmagnetic samples. In a second step the valence shall serves as a detector of the spin polarization. In figure 3.10, the spin-resolved $3d$ band shows a clear imbalance between $\uparrow$ and $\downarrow$ states, i.e. there a more unoccupied $\uparrow$ states than $\downarrow$ states. Hence, the transition probability is higher for $\uparrow$ than for $\downarrow$ and consequently the L_3 edge ($2p_{3/2} \rightarrow 3d$) is rather large for +1 polarized photons, the L_2 edge ($2p_{1/2} \rightarrow 3d$) is rather small. The opposite is true for -1 polarized photons. The difference of these two spectra is the XMCD $= \mu^+ - \mu^-$, where μ^+ is defined at the spectrum, in which the spin polarization of the excited electron spin from the $2p_{1/2}$ and the unoccupied final state are parallel [78], and μ^- vice versa.

The determination of spin μ_s and orbital μ_l moments per unoccupied final state n_h from the XMCD spectra is possible by the use of the so called sum rules [86, 87].

$$\frac{\mu_s}{n_h} = -\frac{6\int\limits_{L_3}(\mu^+ - \mu^-)dE - 4\int\limits_{L_3+L_2}(\mu^+ - \mu^-)dE}{\int\limits_{L_3+L_2}(\mu^+ + \mu^-)dE} \cdot \left(1 + \frac{7\langle T_z\rangle}{2\langle S_z\rangle}\right)^{-1} \mu_B, \tag{3.19}$$

$$\frac{\mu_l}{n_h} = -\frac{3\int\limits_{L_3+L_2}(\mu^+ - \mu^-)dE}{4\int\limits_{L_3+L_2}(\mu^+ + \mu^-)dE} \cdot \mu_B, \tag{3.20}$$

with the intra-atomic dipole operator $\langle T_z\rangle$. The determination of the spin moment requires either the knowledge of $\langle T_z\rangle$ for the specific system or a negligible value of $\langle T_z\rangle$ compared to μ_S due to symmetry reasons. If such a high symmetry is not given, $\langle T_z\rangle$ can be calculated with some effort for specific systems, e.g. with the help of DFT. For molecular systems, e.g. FePc, the value of $\langle T_z\rangle$ can even exceed μ_S and

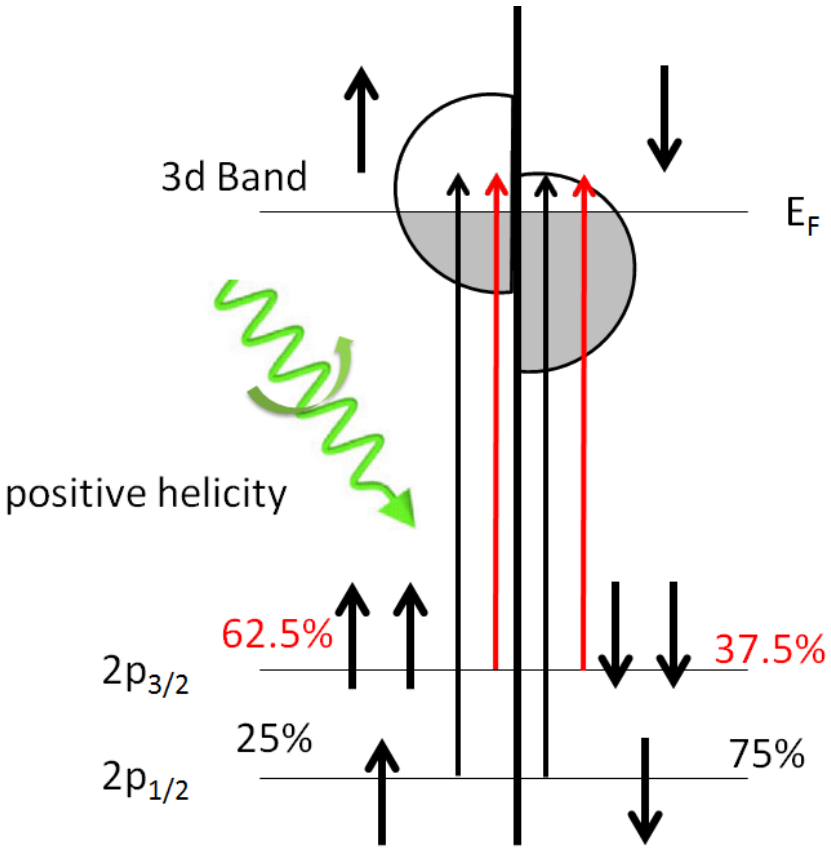

Figure 3.10.: The XMCD effect illustrated for the L edges of a magnetic 3*d* transition metal for irradiation of x-rays with positive helicity. For x-rays with negative helicity the transition probabilities of spin up and down electrons are *vice versa*.

can have the same or opposite sign [42, 88]. The focus of this work is the interaction between the molecules and the surface and the resulting electronic and magnetic properties of the spin-hybrid system. Quantitative numbers of magnetic moments play a minor role and are not determined.

3.3.3. Synchrotron radiation

Synchrotron radiation was predicted and discovered in the 1940s [89, 90]. However, before the 1970s it has been regarded as undesired energy loss, a waste product of the accelerated electrons [43], until scientists recognized the potential of the unique properties of the synchrotron radiation. Since then synchrotrons have been specially designed to produce synchrotron radiation, representing an important part for many areas of modern research.The principle construction of a synchrotron is shown in figure 3.11: Electrons are accelerated in a linear accelerator before they

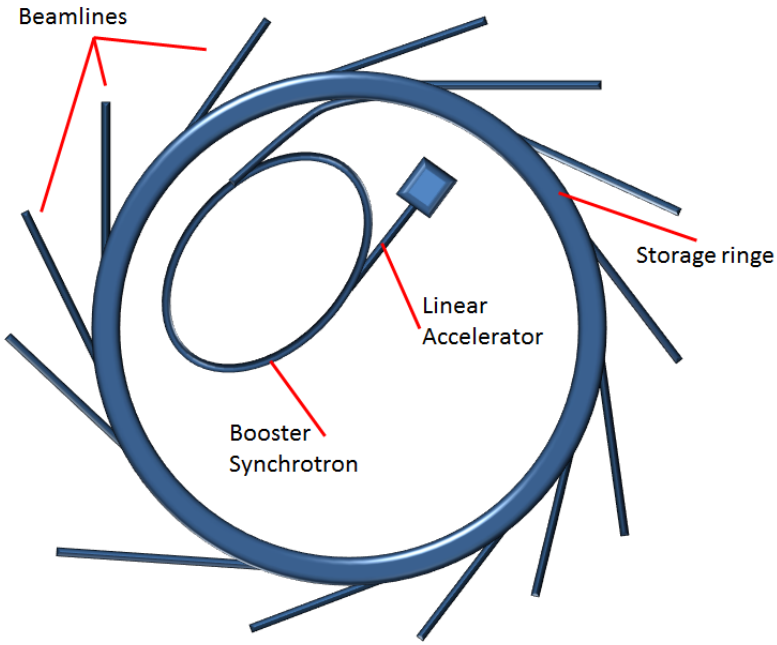

Figure 3.11.: Sketch of a synchrotron showing its main components.

are introduced to the synchrotron, where they are further accelerated to nearly velocity of light c and forced into an elliptical trajectory by bending magnets. After reaching a certain velocity, the electrons are injected to the circular storage ring, in which the synchrotron radiation is created. At the end of several beamlines, various experiments can be executed in dependence of the specific beamline and endstation.

The Lorentz force $\mathbf{F} = q_e\ \mathbf{v_e} \times \mathbf{B}$ resulting from the magnetic fields $\mathbf{B}$ in the storage ring forces the electrons to move on a circle track. According to the laws of electrodynamic, these electrons emit electromagnetic radiation. Let us consider the simplest case that the radiation is a consequence of the electrons deflected by a single bending magnet. The emitted radiation is linearly polarized and has a continuous spectrum from infrared to the hard x-ray with a peak at an energy value that depends on the energy of the deflected electrons. The electron energy in most synchrotrons is between 2 GeV and 8 GeV. With the help of mirrors, apertures and monochromators, a monochromatic, focused photon beam is produced in the beamline.

The results presented in this work have all been measured at undulator beamlines. Undulators [91, 92] are insertion devices of so called third generation synchrotrons. The principle functionality of an undulator is shown in figure 3.12. Two block structures of magnets with alternating magnetic directions enclose the electrons on their trajectory. Hence, the Lorentz force on the electron is pointing in opposite directions for adjacent magnets, resulting in the shown wiggled motion of the elec-

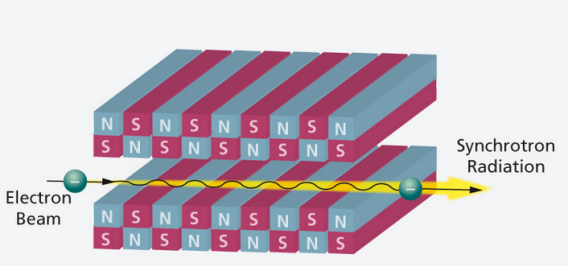

Figure 3.12.: Structure of an undulator used at third generation synchrotrons [93]. The two magnetic block structures can be shifted against each other to control the polarization.

tron. Due to interference as consequence of these oscillations, the resulting spectrum of the emitted radiation is not continuous, but peaked on certain wavelengths. The wavelength can be calculated with the so-called undulator equation [78]

$$\lambda = \frac{\lambda_u}{2\gamma^2}\left(1 + \frac{K^2}{2}\right). \tag{3.21}$$

In this equation λ_u is the period of the undulator array, $\gamma = \left(1 - \frac{v^2}{c^2}\right)$ is the relativistic factor and K is the deflection parameter, defined by

$$K = \frac{eB\lambda_u}{2\pi mc}. \tag{3.22}$$

To alter the radiation, the magnetic field has to be changed according to equation 3.21. For electromagnets one has the options to control $\mathbf{B}$ with the electric current. However, it is easier and more common to change the gap between the magnets. The peak width at half-height is a few ten eV, but smaller than a normal XA spectrum. However, to receive the best quality, it is necessary to have a constant radiation intensity for the complete spectrum. The gap-scan technique enables that, because the undulator gap and the monochromator are controlled simultaneously, while the spectrum is recorded [94]. Aside the gap, the second important undulator parameter that can be set, is the shift Δ in the periodic direction, which is responsible for the polarization of the radiation:
$\Delta = 0$ linear polarization
$\Delta = 3\lambda/4$ circular right polarization
$\Delta = \lambda/4$ circular left polarization.

3.3.4. Beamline characteristics

ID08, ESRF

The experiments described in the chapters 4.1.4, 5.4, 5.5 and 5.6 have been performed at the beamline ID08 of the European Synchrotron Radiation Facility (ESRF) in Grenoble, France. The beamline, supervised by Nick Brookes, was upgraded and renamed according to its new position ID32 in 2014. In the preparation chamber the samples can be cleaned according to the before described sputter-anneal procedure. For the sample characterization AES, LEED and STM are available. Additional evaporators can be mounted depending on the experimental requirements. The investigated sample can be cooled down to $T = 8$ K and a magnetic field up to $B = 5$ T can be applied. Variable polarization enables the measurement of XMCD and XLD in the energy range of 380 eV to 1500 eV.

DEIMOS, SOLEIL

The DEIMOS beamline (SOLEIL, near Paris) is operated by Philippe Ohresser and is very similar to the ID08 beamline. AES, LEED and STM are available and additional evaporators can be mounted for the sample preparation in addition to the permanently installed sputter gun and heater stage. The evaporation cryostat enables XMCD and XLD measurements at $T = 2$ K, while the magnetic field can reach 6 T and the energy range is 350 eV to 2500 eV. In chapter 4.2 and 5.4 the results measured at DEIMOS are presented.

SIM, SLS

The SIM Beamline at the Swiss Light Source (SLS), Paul Scherrer Institute (PSI), in Villigen, Switzerland, is an undulator beamline producing soft x-rays (90-2000 eV) with variable polarization supervised by Armin Kleibert. Various endstations can be used for different experimental setups. For the purpose of this work we used a dilution refrigerator, supervised and operated by Loïc Joly and Jean-Paul Kappler, combined with a superconducting magnet ($B_{max} = 7$ T), enabling the unique possibility of XMCD measurements at $T = 0.5$ K. The results are presented in chapter 5.3.

UE52-PGM, BESSY II

In contrast to the other described beamlines, the Undulator beamline UE52-SGM (90 eV $< E <$ 1500 eV) has no fixed endstation. Therefore the experiments described in chapter 4.1.3 have been performed with a UHV system belonging to the group AG Wende. Aside the effort and the costs to transport the heavy UHV chamber

with all pumps, tools etc. from Duisburg to Berlin, there are other disadvantages, e.g. the absence of a bath cryostat and a superconducting magnet. A water-cooled coil delivers a small magnetic field and the sample can be cooled with a continuous flow cryostat ($B_{max} \approx 80$ mT, $T_{min} \approx 40$ K). The UHV system is used for several purposes and not specialized like a fixed endstation only used for XAS. Hence, the reliability and noise level can be slightly worse. However, this UHV chamber was used for XAS at BESSY many times and excellent results have been achieved [20, 21, 27, 95–97]. There are also many advantages of executing the experiments with the UHV chamber from the home institute. Before the beamtime all parameters for the sample preparation can be calibrated and adjusted with high precision. The chamber can be constructed according to the requirements of the experiments and consequently a much wider range of possible samples can be fabricated *in situ* at the synchrotron. During the beamtime it was possible to sputter and anneal the sample and to characterize with AES, LEED. Fe, Ni, Co films could be produced from two electron beam evaporators and molecules have been thermally evaporated from a molecule evaporator.

4. Tailoring the magnetic interaction of planar paramagnetic molecules on surfaces

Work to tailor the spin of planar molecules with 3*d* metal centers has been ongoing for a decade [19] and several approaches to manipulate the magnetic coupling and the magnetic properties of the system have been published [27, 62, 96, 98, 99]. In this chapter the influence of variations in the spin-hybrid systems on the magnetic coupling are investigated. The spin-hybrid system can be varied by modifying the substrate, replacement of the molecule or the insertion of interlayers. Several variations have been investigated and are presented in this work. The effect of inserted interlayers of oxygen and graphene on the magnetic coupling between FePc molecules and Co and Ni substrates is studied. Since the studies are performed using the same molecule, the changes in the coupling are directly related to the used substrate and the mediation via oxygen and graphene, respectively. In the second section the molecule is replaced by a Co porphyrin molecule. The ligand is responsible for the adsorption geometry and can even affect the spin state of the central ion. A change from a Pc to an OEP molecule is therefore expected to show different properties. On the one hand, the OEP only has four equivalent N atoms in contact with the ion, while the Pc molecule has four additional and non-equivalent N atoms. These changes in the ligand changes the ligand field and can therefore affect the 3*d* orbitals and intramolecular bindings. The outer ethyl rings have components perpendicular to the molecular plane in contrast to the planar FePc molecule. A different adsorption geometry, especially a different adsorption height, can be expected due to those ligands and the magnetic interaction is sensitive to the molecule-surface distance. Not only the ligand, but also the central 3*d* ion is replaced, which has a huge impact. The different occupations of orbitals, different spin states and different communication channels which are involved in the coupling, may lead to different coupling mechanisms.

4.1. Utilizing magnetic surfaces to manipulate FePc molecules

4.1.1. Introduction

In the following section I will present studies of FePc molecules adsorbed onto different surfaces. This section is divided into three subsections, of which the first one presents a structural characterization with LEED to obtain a long-range ordering of the molecules. The second and third subsections show magnetic, electronic and also structural characterizations, studied by XAS and supporting DFT calculations. The interaction of the molecules with ferromagnetic substrates, i.e. Co and Ni, are investigated as well as the manipulation of the interaction by adjusting the particular spin-hybrid system. Therefore the influence of an O interlayer between the Co(100) film and the FePc is studied, as well as the influence of a graphene layer between the molecules and the Ni(111) single crystal.

4.1.2. Long-range ordering of a submonolayer FePc on FePc/O/Cu(100)

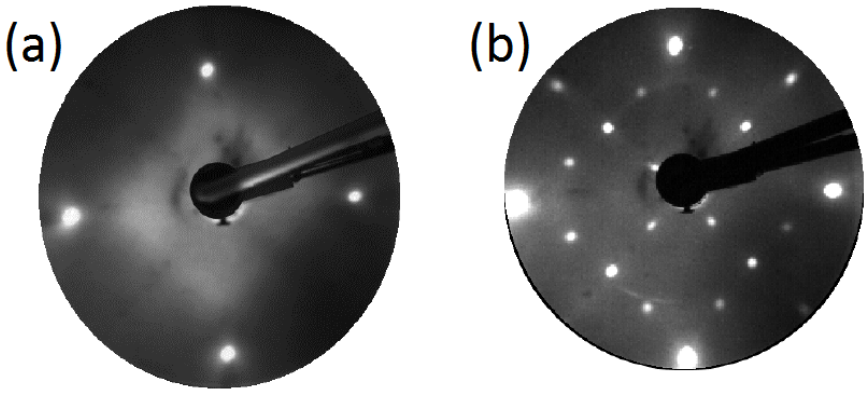

Figure 4.1.: LEED patterns of a clean Cu(100) surface (a) and of the $(2\sqrt{2}\times\sqrt{2})R45$ reconstruction coming from the O adsorption at the electron energy of 70 eV.

Though LEED is a method, which is more likely used to investigate crystalline surfaces, it also offers the possibility to determine adsorbates, like atoms or molecules, as long as they show a long-range ordering. Parts of the following LEED analysis were already presented in my diploma thesis [100].

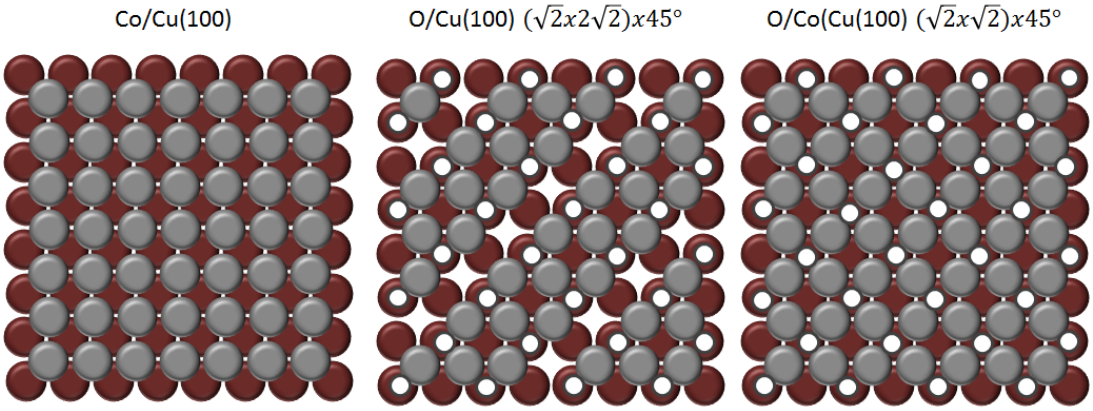

Figure 4.2.: Sketch of the top layers of the samples Co/Cu(100), O/Cu(100) and O/Co/Cu(100).

Figure 4.1 shows the LEED patterns of the investigated surfaces Cu(100) and O/Cu(100). The first order diffraction spots in figure 4.1 (a) of the face-centered cubic Cu(100) are visible, showing the expected four-fold symmetry. The additional spots in figure 4.1 (b) result from the well-known $(\sqrt{2} \times 2\sqrt{2})R45°$ O-reconstruction [101]. The schematic view on the top layers are given in the sketch in figure 4.2. Though the O-reconstruction is not quadratic anymore, the four-fold symmetry is still preserved in the LEED pattern. This is a result of two equivalent domains of the O superstructure which are rotated by 90°. The superposition of these domains is represented by the LEED pattern.

In the following paragraph the ordering of FePc molecules on O/Cu(100), investigated via LEED, will be described. A 0.4 ML thin film was thermally evaporated *in situ* with the Cu substrate held at room temperature. Since the molecules are clearly larger than the atomic distance of the Cu atoms, potential LEED spots are expected to be visible at much lower energies. Figure 4.3 shows the LEED patterns for the molecule-covered O/Cu(100) for two different energies at two different temperatures. A temperature effect is clearly visible in the LEED patterns. While only a blurred background can be obtained at room temperature, at $T = 80$ K sharp spots arise in the very low energy regime, indicating ordered structures with long periods. Hence, the FePc molecules build self-assembled structures on the O/Cu(100) surface. However, the interaction between the molecules and the surface is not strong enough to fix the position of the molecules at room temperature. The mobility of the molecules on the surface leads to the blurred background in figure 4.3 (a) and (c). Cooling down the sample with liquid nitrogen to $T = 80$ K strongly reduces the molecules' mobility. The position on the surface freezes and sharp spots are visible in figure 4.3 (b) and (d).

To conclude the ordering of the molecules on the surface, the LEED spots

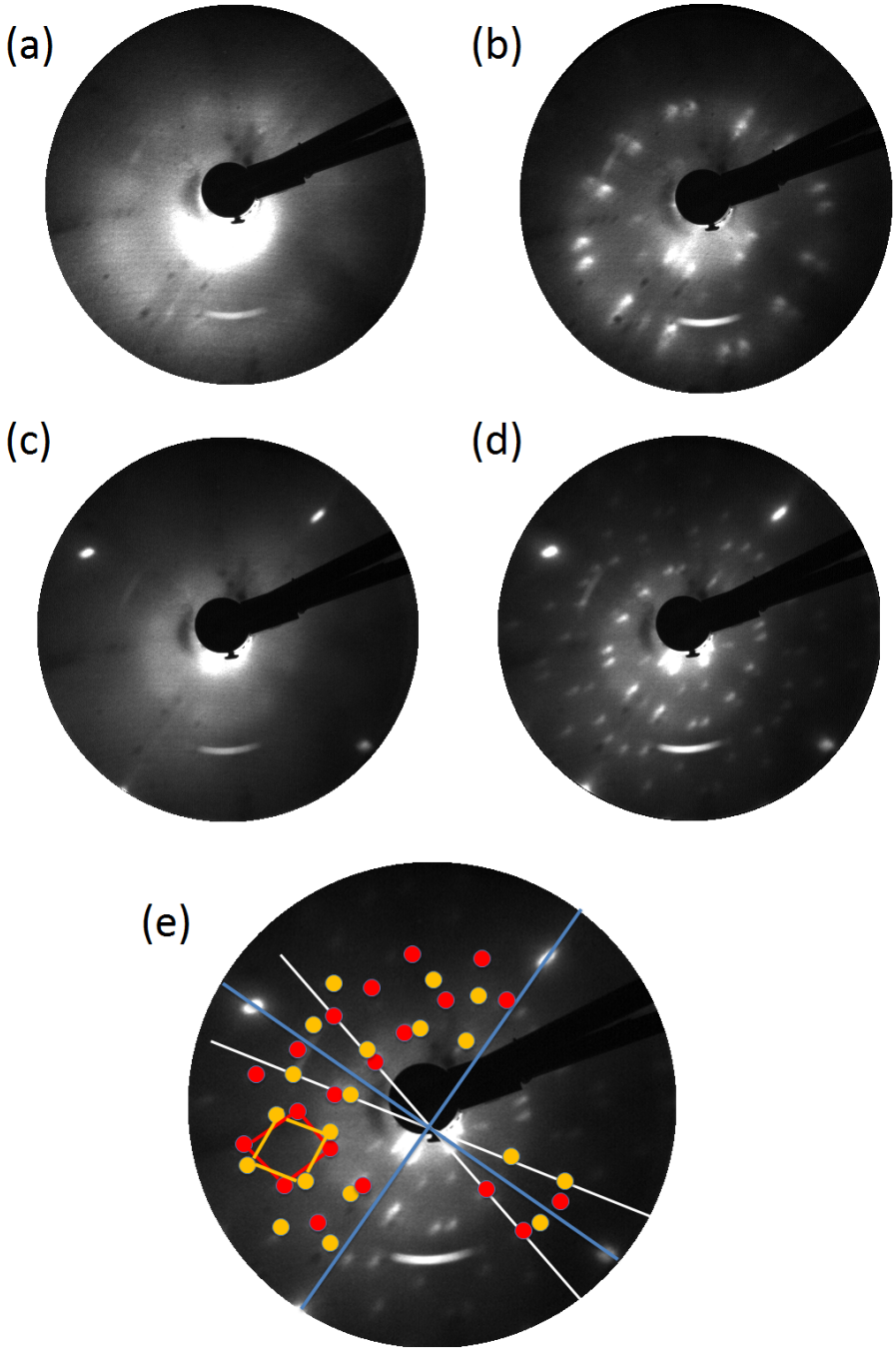

Figure 4.3.: LEED patterns of the molecule-covered O/Cu(100) surface at T = 300 K (a, c) and T = 80 K (b, d) for the energies of E = 14 eV (a, b) and E = 32 eV (c, d). (e) Illustration of the analysis of the LEED pattern from (d).

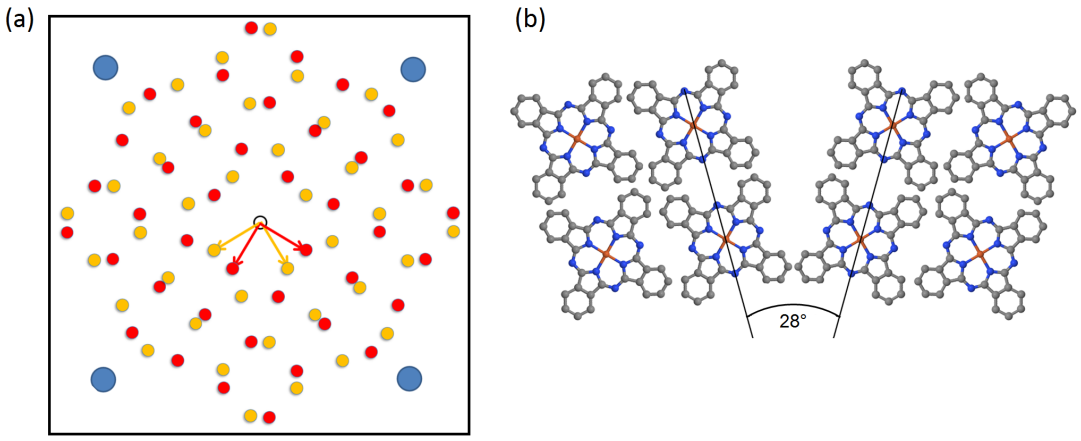

Figure 4.4.: (a) Simulated LEED pattern after the analysis of figure 4.3 (d) and (b) possible ordering of the two molecular domains in the real space according to the analysis.

have to be analyzed with respect to the known LEED spots coming from the O/Cu(100) surface. The large number of spots coming from the adsorbed molecules makes it difficult to conclude the ordering in a first view. However, it is obviously arranged in a fourfold symmetry. Assuming two domains with the same period length, but tilted by an angle, the LEED pattern can be analyzed. In figure 4.3 (e) some spots of the two domains are marked together with the unit vectors in the reciprocal space. The blue and white lines illustrate the angle between the molecular domains and the Cu lattice. It should be mentioned that the LEED screen is not spherical, which deforms the pattern. Hence, spots in the center are closer to each other than at the edge.

To illustrate the analyzed LEED structure more clearly, figure 4.4 (a) shows a simulated LEED pattern according to the analysis from figure 4.3 (e). This simulated pattern is not only to qualitatively show the LEED reflexes, but also helps to analyze the quantitative ordering of the molecules on the surface. The blue spots represent the reflexes from the O/Cu(100) surface, i.e. from the O-reconstruction. The distance between two O atoms in the real space is 0.36 nm. By comparison of the distances in the reciprocal space, the distance between two molecule centers is determined as (1.47 ± 0.05) nm, which is close to the molecules' diameter. The angle between the two domains is $(28 \pm 2)°$. A possible arrangement of the molecular domains in the real space is given in figure 4.4 (b). However, from the LEED analysis one can only conclude the relative ordering of the molecules to each other, while the exact adsorption position on the O/Cu(100) lattice is unclear and the individual molecules can be randomly rotated. The image in figure 4.4 (b) is just an example of a possible arrangement. To determine the orientation of the molecule

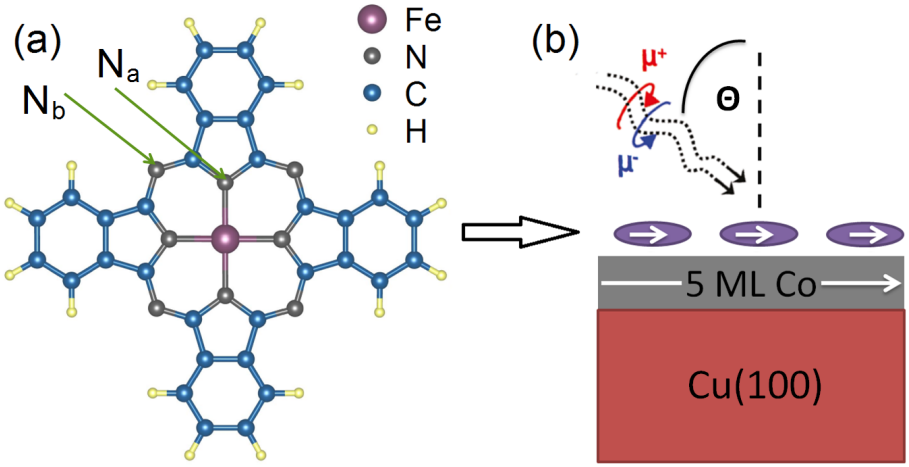

Figure 4.5.: (a) Sketch of the FePc molecule composed of an Fe (purple) ion in the center, 8 N (gray), 32 C (blue), and 16 H (yellow) atoms. (b) Schematic illustration of the XMCD measurement for the sample FePc/Co/Cu(100) under the incidence angle θ [27].

or even the lateral adsorption position, one has to do additional measurements, e.g. XAS or STM. With help of DFT it is also possible to calculate the adsorption geometry and position of the molecules.

4.1.3. Tuning the magnetization of the molecules by an O interlayer

This section is about a combined study of XAS and DFT calculations on the spin-hybrid system FePc/Co/Cu(100) and the system FePc/O/Co/Cu(100). One focus is on the magnetic coupling between the molecules and the ferromagnetic substrate and the influence of the O interlayer on the magnetic coupling. A second point is on the structural characterization, i.e. the preferred adsorption position and orientation of the molecule. As a third part, the N K edge is compared for the two different systems to analyze the interaction with the substrate. DFT enables to distinguish between the two non-equivalent N atoms in the molecule. The section is based on reference [27] [D. Klar *et al.*, Phys. Rev. B 88, 224424 (2013)].

Experimental Methods

Figure 4.5 shows the schematic structure of the investigated sample. A submonolayer of FePc molecules is adsorbed on a 5 ML Co film which is epitaxially grown on a Cu(100) surface. The second investigated sample has an additional O interlayer between the molecules and the Co film (not shown in this figure). The prepara-

tion of the samples has been performed at the synchrotron *in situ* immediately before the x-ray absorption measurements at a base pressure of 2×10^{-10} mbar. The *in situ* preparation in the UHV regime guarantees uncontaminated samples and undisturbed interaction of the individual components of the samples. As cleaning procedure for the Cu(100) surface sputter-heating cycles we carried out several times and the surface quality was subsequently checked by means of LEED and AES. After obtaining a clean and smooth Cu(100) surface, the ferromagnetic 5 ML thick Co film was deposited via MBE with a deposition rate of 1 ML/min. The resulting Co film has a well-defined easy magnetic axis parallel to the surface [102]. The O reconstruction was produced by a well-known procedure [101, 103–105]. Before the Co deposition, an O $(\sqrt{2} \times 2\sqrt{2})R45°$ superstructure was constructed on the Cu single crystal. The O atoms act as a surfactant for the growth of the Co film and this results in a well-characterized $c(2 \times 2)$ superstructure of 0.5 ML atomic O on top of the Co film. The O-adlayer does not affect the easy magnetic axis of the underlying Co film, which is still in-plane. In the last preparation step the FePc molecules were thermally evaporated with a slow rate of 0.05 ML/min from a Knudsen cell onto the substrate held at room temperature. Before the sublimation the molecules were degassed at their evaporation temperature for several hours to guarantee that potential molecular fragments and contamination are not adsorbed on the surface during the evaporation process. The XAS measurements in total electron yield were performed at the undulator beamline UE52-SGM at HZB-BESSY II. Since the magnetization of the Co film is parallel to the surface in both cases, i.e. with and without O surfactant, the XMCD measurements were executed at grazing photon incidence ($\theta = 70°$). Angle-dependent XAS at the N K edge and Fe $L_{2,3}$ edges with linearly horizontally polarized light were carried out to study the orientation of the FePc molecules on the surface and contributions of the different orbitals. The XMCD measurements were performed in an applied field of 20 mT parallel to the beam. This small magnetic field serves only to saturate the in-plane magnetization of the ferromagnetic Co film. To avoid radiation damage to the molecules, the x-ray intensity was reduced. In addition the sample was moved frequently, so that the x-ray spot impinges on a fresh position and no long-term radiation damage effects can affect the results.

Computational Methods

In addition to the experimental results, complementary theoretical studies were performed by Dr. Barbara Brena, Dr. Heike C. Herper, Dr. Biblap Bhandary and Dr. Sumantha Bhandary in the group of Prof. Olle Eriksson at the Uppsala University in Sweden.

DFT calculations using the VASP code [106] and the projector augmented wave approach (PAW) [107] were executed to determine the electronic and magnetic structure of FePc on both the bare and O-covered Co(100) surfaces. The

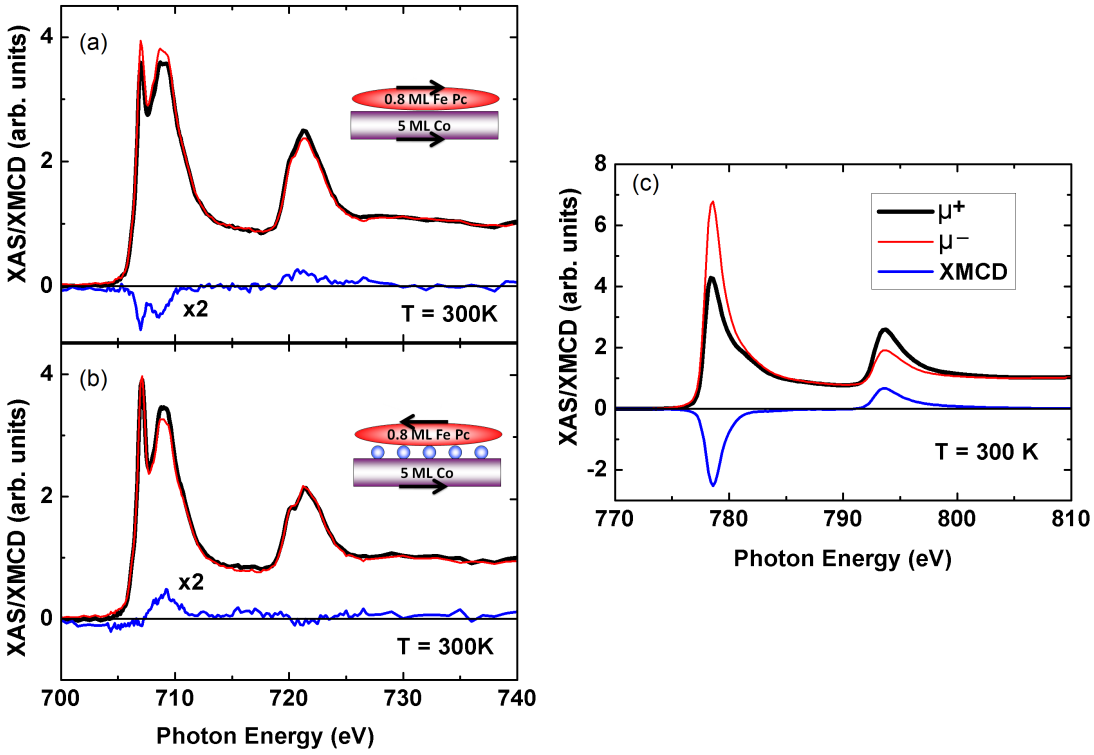

Figure 4.6.: Fe $L_{2,3}$ XAS and XMCD spectra of 0.8 ML FePc/5 ML Co (a), 0.8 ML FePc/O/5 ML Co (b) and Co $L_{2,3}$ XAS and XMCD spectra (c). The spectra are recorded at room temperature and with a grazing angle of θ =70° [27].

NEXAFS calculations were carried out for a single FePc molecule using the DFT code StoBe [108]. A more detailed description of the computational methods can be found in A.1.

Magnetic Coupling between molecule and substrate

Figure 4.6 shows the normalized XAS and XMCD spectra at the Fe $L_{2,3}$ edges of the sample 0.8 ML FePc/5 ML Co (a) and 0.8 ML FePc/O/5 ML Co (b). The corresponding Co XAS and XMCD is shown in (c). The red line (μ^-) represents the normalized spectrum for left circularly polarized light, the black one (μ^+) is for right circularly polarized light and the blue line is the difference ($\mu^+ - \mu^-$). The Fe XMCD signal is amplified by a factor of two for a clearer presentation. All spectra have been recorded at room temperature and show a clear dichroic signal. This is expected for the ferromagnetic Co film, which has a Curie temperature clearly above room temperature. However, the paramagnetic FePc molecules are not expected to show any magnetic dichroism, if they were isolated or in a powder

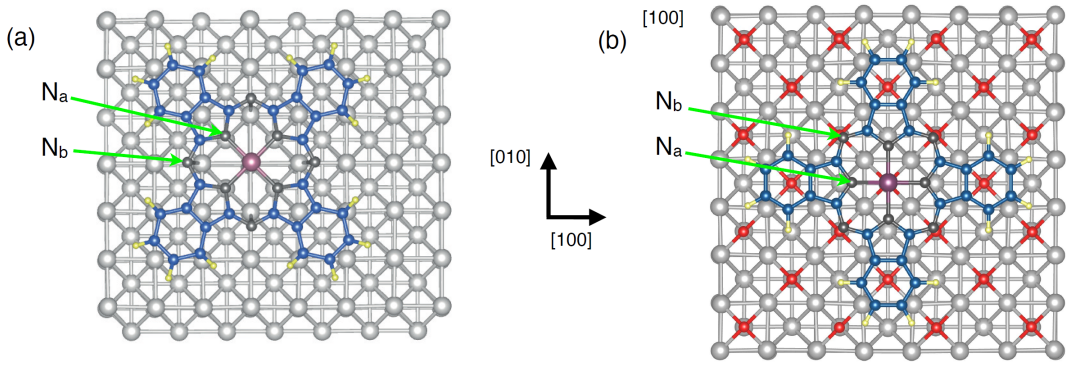

Figure 4.7.: (a) Top view of the ground state configuration of FePc/Co(100) (note that the long axis of the FePc molecule is rotated with 45° with respect to the (100) direction of the substrate). The purple sphere represents the Fe atom, dark gray spheres represent the N atoms, blue spheres the C atoms, yellow spheres the H atoms, and light gray spheres the Co atoms. (b) Top view of the ground state configuration on FePc on c(2×2)O/Co(100). Red circles denote O atoms. The color scheme for the other atoms is the same as in (a) [27].

sample, only interacting with each other. Hence, the magnetization in the molecules must be induced by the contact with the Co surface. A ferromagnetic coupling exists between the Fe ion in the molecules' center and the Co atoms. However, the coupling path cannot be determined alone from the experimental results. It can be an indirect ligand-mediated coupling, a direct interaction between Co and Fe or a superposition of both. However, the XMCD of the FePc changes its sign, when the O layer is between the molecules and the substrate. While the dichroic signal of the underlying Co film remains negative at the L_3 edge and positive at the L_2 edge, it is *vice versa* at the Fe edges. The magnetization of Fe is antiparallel to the one of the Co film, indicating an antiferromagnetic coupling in presence of the oxygen. This coupling can be understand in a simple picture of a 180° superexchange which results in an antiparallel spin alignment. In this picture both, the Co atoms and the Fe ions hybridize with the O atoms in between. To confirm this assumption that the Fe hybridize with O and the exchange is not ligand-mediated, the adsorption position of the FePc molecule has to be determined. To make an experimental, quantitative statement about the coupling, a detailed field- and temperature dependence of the XMCD signal would be necessary. However, since the XMCD is clearly present at room temperature, the coupling appears to be quite strong. A more precise and quantitative analysis of the coupling is given in the following as result of the DFT calculations.

Qualitatively the results of the x-ray absorption experiment can be confirmed by the DFT calculations. They reveal that the FePc molecule on the bare Co substrate

is adsorbed on top of Co with a rotated geometry of 45° (as described in the caption of figure 4.7 (a)), whereas on the oxidized surface the ground state is adsorbed at the on top of O position, see figure 4.7 (b), without rotation. The FePc molecule orient on both surfaces in a way that the N_a atoms sit on top of a Co atom, in contrast to what was found for MnPc on Co(100) in reference [22]. In the literature various works on the fcc(111) surfaces (Ag, Cu, Au) exist [109–120], in which the structure and the exchange mechanisms are studied. Since a different surface is investigated in the present work, it is not surprising that different adsorption sites are found. From the investigations described here it turned out that the coupling mechanism and adsorption position strongly depend on choice of the molecular substrate hybrid system. In comparison to the FePc in the gas phase, on the metallic Co film the molecule is deformed, while on O the gas-phase structure is retained, which is expected as consequence of a weaker interaction due to the oxygen. On Co(100) the Fe-N_a bond length is increased by 0.02 Å compared to FePc in gas phase and the angle between C-N_a-C is reduced by about 4°. Though the adsorption position is found to be different, it does not have an effect on the spin state. The molecules' spin state is $S = 1$ and Fe carries a magnetic moment of 2 μ_B.

The change from ferromagnetic to antiferromagnetic coupling on the O-covered Co(100) surface is also confirmed by the calculations. Figure 4.8 shows the spin density for both substrates, clearly revealing ferromagnetic coupling on Co(100) and antiferromagnetic coupling on O/Co(100). Not only the sign changes due to the O adlayer, but also the coupling strength is remarkably reduced from 0.229 eV to -0.097 eV.

Another important contribution from the calculations is the description of the coupling mechanism that cannot be received from the experimental data. In figure 4.8 (a) the coupling path on the bare Co(100) can be clearly observed. The magnetization density shows that there is a direct coupling between the Fe and Co substrate. However, not only the Fe but also the C atoms in the benzene rings possess a magnetization perpendicular to the plane of the surface, albeit the moments of the C atoms are small, whereas the magnetization density of the N atoms is mostly directly in the plane of the molecule. Consequently, on the bare Co substrate a mixture of direct coupling and indirect coupling via the benzene rings occurs. This fact stresses the important role of the benzene C atoms in the FePc coupling to the Co surface.

The situation is different, when molecules are adsorbed on the O-covered Co(100) surface. As expected, the magnetic coupling between molecule and surface is mainly mediated by the coupling of the Fe atom to the Co substrate via the O atom, i.e. the dominating mechanism is a 180° superexchange which results in an antiparallel spin alignment. The benzene C atoms play a minor role, however, they show coupling effects with the surface. Only C atoms next to N_b atoms exhibit

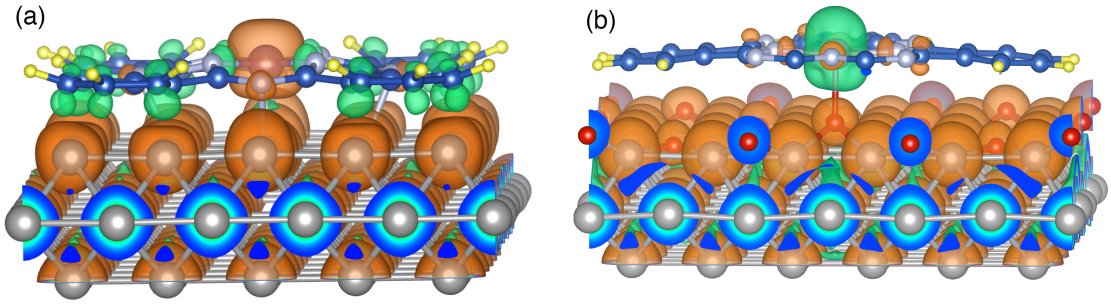

Figure 4.8.: Isosurface spin density close to the Fermi level for FePc on top 45° site on bare Co(100) (a) and on top of O position in case of oxidized surface (b). Brown denotes up-spin and green down-spin density such that same color of magnetization density of Fe and Co surface (a) corresponds to FM coupling whereas the different colors on the oxidized surface (b) denote an AF coupling of Fe and Co [27].

magnetization perpendicular to the surface. The N_a atoms interact mainly with the central Fe atom.

Calculated magnetic structure

The DFT calculations reveal that the Fe atom is in an intermediate spin state $S = 1$ on both surfaces and has therefore the spin moment of $2\mu_B$, which is in contrast to previous findings of Fe porphyrin molecules on a Co(100) surface, which was claimed to be in a high spin state, which is stabilized by the oxygen [21]. The $S = 1$ spin state found here, is in agreement with previous calculations for FePc on the bridge position [121]. The very small spin moment of the elements in the ligands cannot be detected via XMCD, but calculated. The N_a atoms directly bound to the Fe have a spin moment of -0.02μ_B, while the N_b atoms have a spin moment of 0.023μ_B. Small spin moments are also obtained for some of the C atoms in the benzene rings. More specifically, the eight more external C atoms have a spin moment of -0.016μ_B, and the eight atoms directly bound to these and still belonging to the benzene rings have a spin moment of -0.034μ_B. Due to the particular distortion of the adsorbed molecule, these atoms are at rather short bonding distances from the Co atoms underneath, of 2.01 Å and 2.16 Å respectively. This result further strengthens the observation that in FePc, the outer C atoms in the benzene rings participate in the hybridization with the Co surface.

Figure 4.9 (a) shows the calculated density of states for the chemisorption configuration on top of Co 45° (a). The electronic configuration is a $(d_{xy})^2$ $(d_{z^2})^2$ $(d_\pi)^2$, which also corresponds to one of the two proposed configurations for the FePc molecule in the gas phase, see for example Ref. [122]. Compared to gas phase

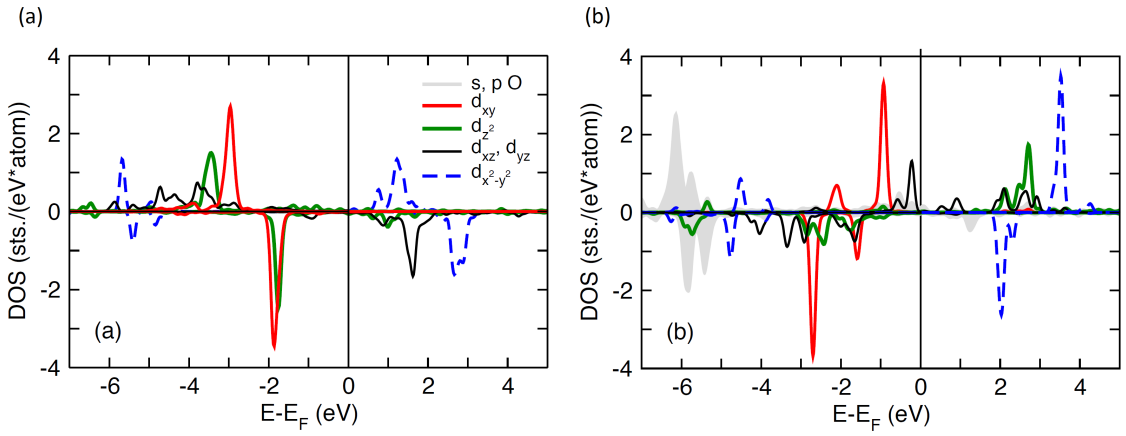

Figure 4.9.: (a) Projected density of states (DOS) of the Fe d orbitals in the FePc/Co(100) top 45° adsorption site. (b) DOS of the Fe d orbitals in FePc/c(2×2)O/Co(100) top of O adsorption site. Gray shaded areas mark the s and p density of states of the O atom beneath the Fe atom [27].

density of states, the d peaks are broader due to interaction with the surface [121]. As previously discussed, the spin-state and the magnetic moments of the Fe atom are not changed in presence of an O adlayer. The electronic structure shown in figure 4.9 (b), corresponds to a $(d_{xy})^2$ $(d_{z^2})^1$ $(d_\pi)^3$ configuration. This configuration is according to Ref. [122] one possible electronic configuration for FePc. The other one is the $(d_{xy})^2$ $(d_{z^2})^2$ $(d_\pi)^2$ configuration obtained on the bare Co(100) substrate.

The spin moments for the ligand elements in the molecule are calculated on O/Co(100) as well, revealing a spin moment of 0.02 μ_B at the N_a atoms. An O atom, which is directly beneath an Fe ion carries a spin moment of 0.18 μ_B. A strong hybridization between O s and p states (gray shaded areas in figure 4.9 (b)) with d_π and d_{z^2} states of Fe is observed, see figure 4.9 (b).

Figure 4.10 shows the magnetic moments of the individual first Co layer atoms and O atoms below the FePc molecule. The position of the FePc molecule is indicated by the red circles. In detail the magnetic moments are given for the Co atoms covered with O (a), the O atoms of the same surface (b) and the Co atoms on the bare Co surface (c). Compared to the free molecule and the bare Co(100) surface, the magnetic moments of the Fe atom and O atom underneath are increased by 0.04 and 0.02 μ_B, respectively, whereas the moment of the Co atom in the first Co layer is reduced by 0.05 μ_B. This hints to a strong interaction between FePc and the Co substrate via the O atoms. However, changes in the magnetic structure of the surface are not restricted to atoms of the direct Fe-O-Co bond. The molecule leads to a reduction of the O moments under the pyrrole and benzene

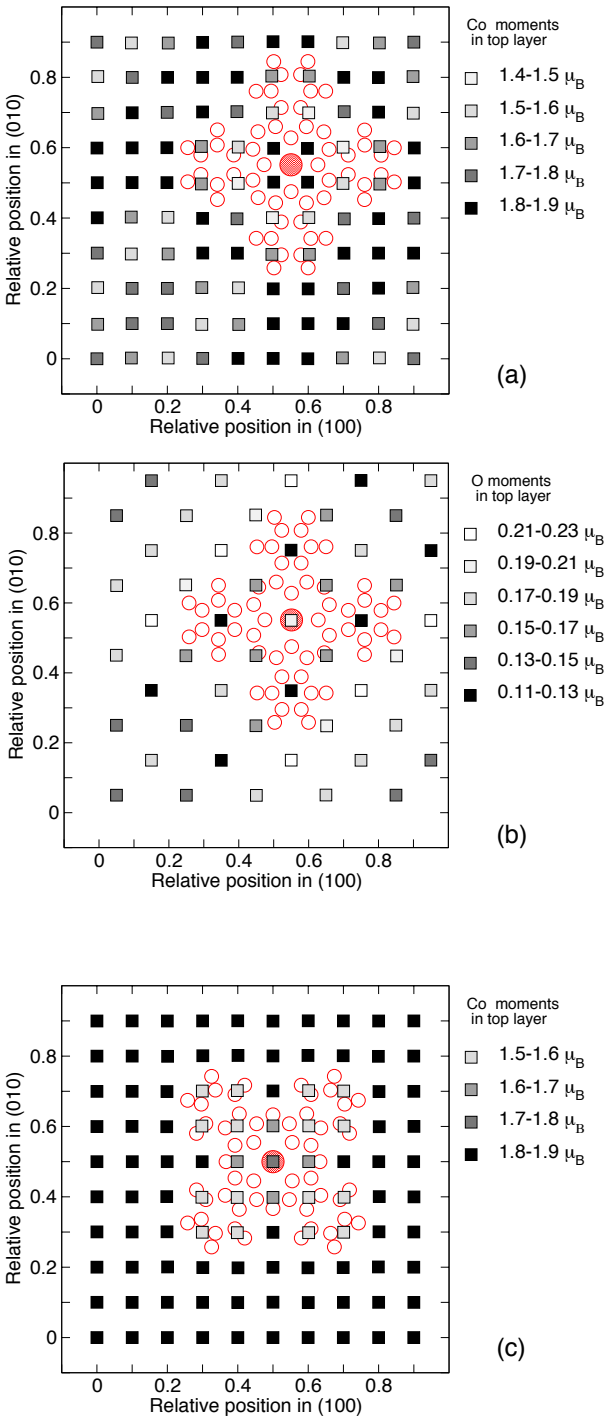

Figure 4.10.: Profile of the magnetic moments in the first Co layer (a) and in the O adlayer (b) in presence of the FePc molecule on O/Co(100). Profile of the magnetic moments in the first Co layer on the bare Co(100) substrate (c). The position of the molecule is sketched by red circles [27].

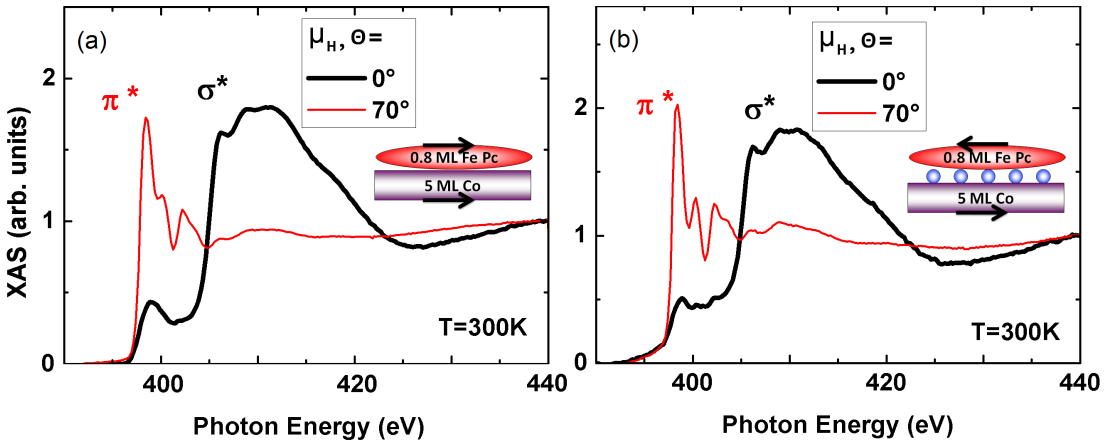

Figure 4.11.: Angle-dependent N K XAS spectra of 0.8 ML FePc/5 ML Co (a), 0.8 ML FePc/O/5 ML Co (b) measured with linearly horizontally polarized x-rays [27].

rings compared to the FePc free surface where the average O moment amounts to 0.17 μ_B, see figure 4.10 (b) for more details. This reduction in moment is continued in the first Co layer which also shows considerably reduced moments of 1.4 - 1.7 μ_B (the average moment without FePc is 1.75 μ_B) in the same regions. Only Co atoms being nearest neighbor to Fe have higher moments of 1.85 μ_B, see figure 4.10 (a).

In figure 4.10 (c) the Co moments are changed only locally under the FePc molecule in the absence of the O layer. The Co atom directly coupled to the Fe atom shows an increased magnetic moment of 2.01 μ_B, whereas the Co atoms under the benzene rings have smaller moments ranging from 1.5 - 1.7 μ_B. All other Co atoms in the surface layer possess magnetic moments between 1.8 and 1.9 μ_B. In reference [116] similar results were found for CoPc/Co(111). These results show that the changes of the Co magnetic moments in (a) and (b) are mainly a consequence of the O c(2×2) reconstruction of the surface. The coupling of the FePc is rather short-ranged and affects basically the Co atoms directly beneath the molecule (c).

Angle-dependent studies of the N K edge

Angle-dependent x-ray absorption studies of the molecules are a simple and effective method to determine the orientation of the molecules on the surface. In addition the results reveal the electronic distributions and anisotropies of the individual elements in the molecule. Additional angle-dependent XAS of linearly polarized x-rays at the Fe $L_{2,3}$ edges can be found in A.2. In the following the angle dependence of the N K edge is studied in detail. The electron is excited from the initial nitrogen 1s state into final unoccupied p states. Experimentally it is easy to distinguish

between π^* and σ^* orbitals at the N K edge and to conclude the orientation of the molecules taking into account the symmetry of the molecule. π^* and σ^* orbitals cannot only be distinguished by the difference in energy, but also by the direction with regards of the molecule. Polarized photons with a defined direction of the $\boldsymbol{E}$ vector will therefore be absorbed different with variation of the incident angle. The direction of $\boldsymbol{E}$ acts as a search light for this excitation. If the electron is excited into the direction of the molecular plane, the unoccupied σ^* orbitals are probed. The asymmetric line shape of these resonances can be described in a scattering framework (see e.g. [123]). However, if $\boldsymbol{E}$ is perpendicular to the molecular plane, the unoccupied π^* resonances are probed. Hence, if the NEXAFS spectra exhibit a strong polarization dependence, the orientation of the molecules on the surface can be analyzed. Furthermore, the fine structures in the NEXAFS spectra provide insight into the interaction of the molecule with the surface. In an earlier work, it has been demonstrated that an intermediate layer of atomic oxygen leads to an effective decoupling of the nitrogen atoms in Fe-porphyrin molecules from the substrate [21]. Because of the weaker interaction of the nitrogen atoms with the surface, sharper features in the nitrogen K edge NEXAFS have been detected in case of Fe-porphyrin molecules adsorbed on the O layer [21].

Figure 4.11 shows the experimental absorption spectra at the N K edge of the FePc molecules on Co/Cu(100) (a) and O/Co/Cu(100) (b). The spectra were recorded with linearly horizontally polarization under perpendicular x-ray incidence $\theta = 0°$ (black) and grazing incidence angle of $\theta = 70°$ (red). The spectral differences of the two difference adsorption geometries are obvious and easy to interpret. The σ^* orbitals are higher in energy because of the stronger bonding and also they are within the molecular plane. On the other hand the π^* orbitals are lower in energy, show sharper structures and are perpendicular to the plane. Hence it is easy to assign the different contribution in figure 4.11 to the different spectral features. Furthermore the adsorption geometry on the surface of the molecule is confirmed as expected, because it has been shown for similar molecules on various surfaces [20, 21, 65, 99, 124]. The molecules adsorb in a lying configuration in agreement with the calculations as sketched in figure 4.8. The general shape of the absorption spectra does not change on the two different surfaces, demonstrating that the O interlayer has no influence on the orientation of the molecule with respect to the Co(100) surface. However, the fine structures of the spectra show clear differences. On the O-covered surface, all structures are more pronounced, while they are broadened on the bare Co surface. The more pronounced fine structures as consequence of a stronger localization confirms the decoupling effect of the oxygen. The strong hybridization on the metallic Co surface and the delocalized orbitals lead to broader structures in the spectra.

To compare the experimental spectra with theoretical results, NEXAFS simulations have been performed with $\boldsymbol{E}$ parallel (0°) and almost perpendicular (70°) to the surface, shown in figure 4.12. The figure shows the direct comparison of the

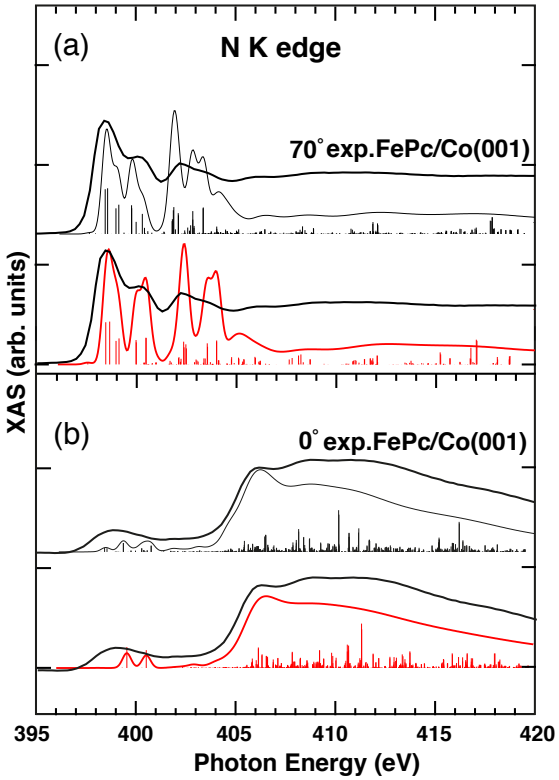

Figure 4.12.: N K edge experimental and theoretical spectra for (a) quasi perpendicular (70°) and (b) parallel (0°) polarization. The experimental spectrum for the case without an intermediate layer of atomic oxygen is shown as black thick line, the black thin line is the total calculated spectrum for the relaxed FePc and the red line is the total spectrum for the symmetric FePc. The bar graphs show the calculated oscillator strengths and the red bars represent the symmetric FePc and black bars the relaxed FePc [27].

experimental and calculated spectra of the N K edge at the x-ray incidence angles of 0° and 70°. The experimental spectra are shown for the Co surface without O interlayer. The calculated spectra are given for the symmetric molecule without surface interaction and the relaxed, distorted one on the surface (for details see figure caption). The structures for both calculated spectra in the perpendicular case (a) are very similar with only slight variations. The small variations in the peak positions and intensities reflect the changes in the π^* molecular structure due to the distortion of the geometry. Two major experimental π^* resonances at the almost perpendicular polarization at 70° are found at about 398.5 eV and 400.3 eV followed by a deep valley at 401.3 eV and by a series of indistinguishable peaks at 402.4 eV and higher energies. The theoretical spectrum of the relaxed FePc has two main peaks at 398.5 eV, with a shoulder at 399.1 eV, and at 399.8 eV, a deep valley

at 400.9 eV followed by a succession of peaks at 401.9, 402.8 and 403.3 eV. Finally there is a smaller peak at 404.7 eV. For the symmetric molecule, one can observe a main peak at 398.7 eV, followed by a double peak at 400.0 eV and 400.5 eV. The valley is located at 401.3 eV. Another major peak is at about 402.5 eV, and a double peak follows at 403.7 and 404.1 eV. A low intensity shoulder is found at 405.2 eV. Apart from small energy differences, both these simulations reproduce the general features of the experimental spectrum. The peaks are due to transitions of N 1s electrons into molecular orbitals with π^* character centered in both N_a and N_b.

For the parallel case (b) the experimental spectrum shows only a broad structure with low intensity at 399 eV, while the simulation reveals two clearly distinguishable peaks at 399.6 eV and 400.6 eV. These peaks are due to the 1s excitation in a N_a atom into in-plane σ molecular orbitals formed by the hybridization of the Fe $3d_{x^2-y^2}$ with N 2p and C 2p. The relaxed molecule shows clearly more structures at lower energies than the symmetric one, in agreement with the experimental results. The distortion of the molecule leads to distorted orbital geometries. While the symmetric molecule has σ^* orbitals in-plane and π^* orbitals perpendicular, the σ^* orbitals in the distorted molecule also reveal perpendicular components and the π^* orbitals in-plane components, respectively. From the K edge theoretical and experimental results we can therefore conclude that in FePc/Co(100) there is a strong interaction of the molecule with the Co substrate which induces a distortion in the molecular structure. This effect is clearly visible in the parallel polarization of the NEXAFS N K edge spectra, and is well reproduced by the simulations.

A strong advantage of the simulations compared to the experiment is the possibility to distinguish between the two non-equivalent N atoms in the molecule N_a and N_b. Figure 4.13 shows the distinct contributions of the two non-equivalent N atoms of the distorted molecule to the simulation of the measurements at almost perpendicular polarization. The partial NEXAFS of N_a is shown in panel (a) and the partial NEXAFS of N_b is shown in panel (b), in comparison with the total theoretical curve and with the experiment. The main peaks are related to the isodensity surfaces for the final state orbitals calculated by StoBe. The π^* resonances of the N_a atom are at higher energies due to the fact that it is bound to the C-atoms and the Fe atom. The high intensity peaks are related to final states of π^* character mostly centered on the C atoms, and especially on the benzene C atoms, like for example in the orbitals C, D and E of panel (a). The C atoms located on the benzene rings are also primarily responsible for the molecule-surface hybridization according to the calculations of the adsorption configuration.

The experimental spectrum of the FePc/O/Co in figure 4.11 (b) for grazing incidence (almost perpendicular $\boldsymbol{E}$ vector) reveals slightly more resolved peaks at 400.3 eV and 402.4 eV with respect to the equivalent features in the FePc/Co spectrum. This is also confirmed by the simulations in figure 4.13, characterized by

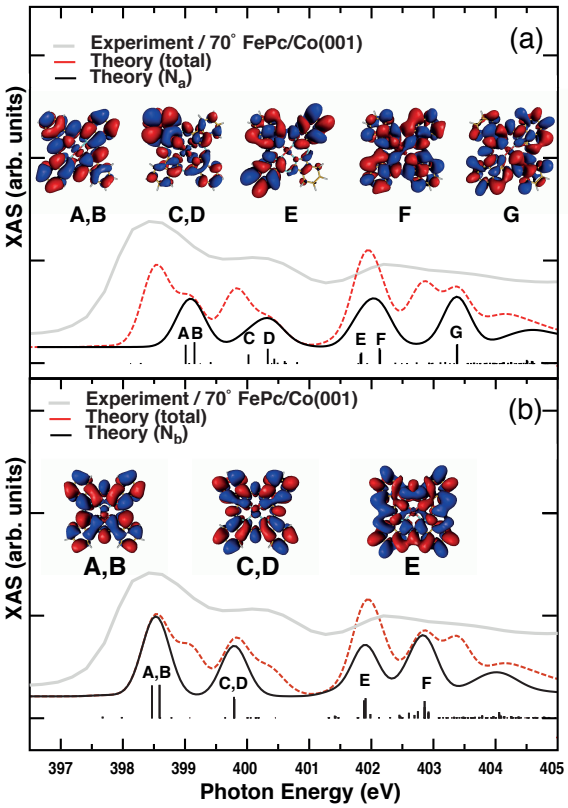

Figure 4.13.: XAS simulation of perpendicular polarization for N_a (a) and N_b (b). The experimental spectrum in the quasi perpendicular set up at 70° is shown (gray thick line). The red dashed line is the total spectrum for the relaxed FePc. The bar graphs show the calculated oscillator strengths for N_a (a) and N_b (b) [27].

slightly better distinguished peaks. On the O-covered surface, the FePc molecule is not as strongly distorted as on the bare Co surface, but remains more symmetric. The interaction of the molecules with the surface is basically mediated by the Fe, not via the ligand. This structural analysis is in agreement with the calculated magnetic coupling mechanism.

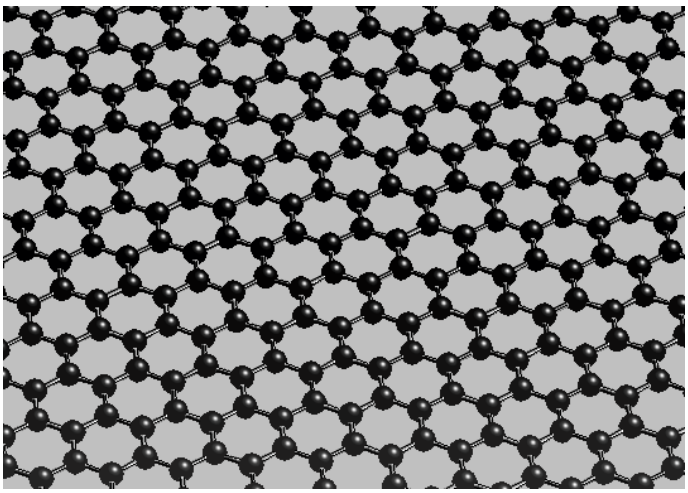

Figure 4.14.: Two-dimensional, hexagonal graphene lattice.

4.1.4. Tuning the magnetization of the molecules by a graphene interlayer

In the following section the coupling mechanism between FePc molecules and a Ni(111) single crystal is studied. In comparison to the ferromagnetic Co film in the previous section, a Ni single crystal does not show a remanent magnetization and as a consequence of the different crystal lattice and surface geometry, different adsorption behavior of the molecules is expected. In addition to the coupling of the molecules in direct contact with the Ni surface, the effect of an interlayer graphene on the coupling is investigated. The results are based on reference [125] [A. Candini, V. Bellini, D. Klar *et al.*, J. Phys. Chem. C 118, 17670-17676 (2014)].

Function of the graphene interlayer

Since its discovery, graphene [126] has become one of the most important topics in various fields of material science. The unique electronic properties of this two-dimensional structure (figure 4.14) make it invaluable for different applications [127]. On a Ni(111) surface, it is possible to grow prefect graphene layers *in situ*. While graphene is mainly known for its electronic transport properties, here the focus is on its magnetic properties. If a magnetic coupling is mediated from the Ni substrate to the molecules via the C atoms in the graphene layer, this is an indirect evidence of an induced magnetic moment in graphene on Ni. Therefore the effect of graphene on the magnetic coupling between the ferromagnetic substrate and the molecules is studied in detail. A second function of the graphene interlayer is to separate the molecules and the metallic surface to maintain the molecular properties. While on metallic surfaces the molecular orbitals are known to become delocalized (see previous section), on the inert graphene surface a localized electronic structure of the

molecules is expected. In contrast to the O interlayer, where the O atoms adsorb isolated on the surface, the C atoms form a two-dimensional graphene sheet. Different electronic and magnetic properties are therefore expected in such a system.

Experimental details

Experiments were carried out at the ID08 beamline of the ESRF in Grenoble, France. The investigated graphene/Ni(111) substrates were partially prepared *ex situ* by Dr. Valdis Corradini and Dr. Andrea Candini in the UHV-chamber in Modena with a base pressure of 5.0×10^{-10} mbar and partially *in situ* directly at the beamline in the preparation chamber of the ID08. A Ni(111) single crystal was used as the substrate. Before the graphene growth, the surface was cleaned by repeated cycles of Ar^+ sputtering and annealing (T = 800 °C for 5 minutes). The quality and the cleanliness of the surface was checked by LEED and XPS. The freshly prepared Ni(111) surface was then heated and stabilized at 500 °C. Ordered graphene overlayers were prepared by introducing propylene gas (C_3H_6), which served as the carbon source, into the chamber. The gas pressure was adjusted to $2{\times}10^{-7}$ mbar using a leak valve, following procedures established in literature [59, 128]. The quality, homogeneity and cleanliness of the prepared graphene/Ni(111) system were checked by LEED, XPS and STM. The procedure was repeated until no evidence of a carbide phase was detected by XPS. The graphene/Ni(111) system is very stable after air exposition. It could be verified that even few weeks after the preparation, for a sample kept in ambient conditions, a clean system can be easily re-obtained showing the same characteristics of the pristine one, by heating in UHV at 500 °C for 5 minutes to desorb impurities. This stability has been already observed and reported by other groups [129] also for graphene on different metals, such as Cu(111) [130]. Hence, the *in situ* and *ex situ* prepared samples show the same quality and identical properties.

Figure 4.15 shows the characterization of the graphene layer by means of XPS (left) and LEED (right). The XPS characterization was executed in Modena by Dr. Andrea Candini. The evolution of the C 1*s* spectra is given depending of the deposition time of propylene gas, as reported in the main panel of figure 4.15. At low deposition time (5 minutes) a distinct peak (C_{carb} at 283.2 eV) is present, which can be easily assigned to nickel carbide, in agreement with literature values [59, 128]. The corresponding LEED pattern showed many irregular spots and a high background intensity (figure 4.15 (b)). By increasing the deposition time the graphene related peak (C_{graph} at 284.7 eV) starts to grow. The completion of a graphene layer is evidenced by the saturation of the C_{graph} peak after 15 min of propylene exposure and by the LEED pattern (see figure 4.15 (c)). Such a sharp hexagonal LEED pattern is proof of the 1×1 reconstruction and a clear evidence of the successful synthesis of graphene. It was also verified that after air exposure, an annealing step for 5 minutes at 500°C can restore the as-grown conditions.

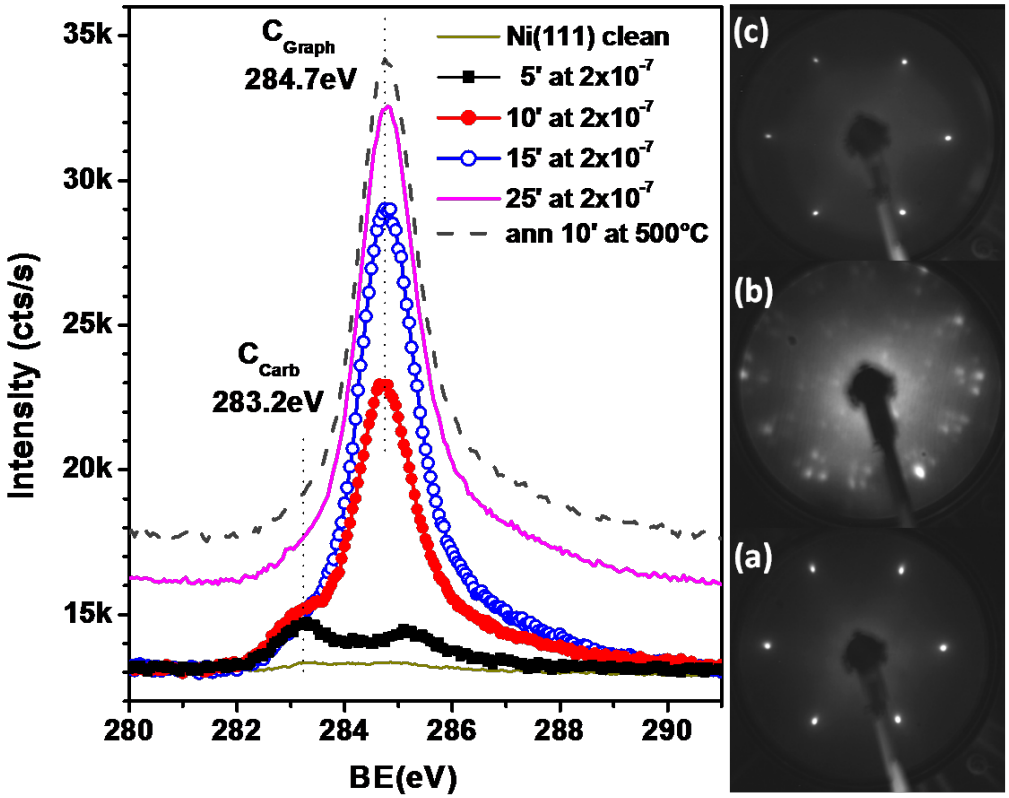

Figure 4.15.: Evolution of the C-1s core level as a function of the deposition time of propylene gas ($p_{prop} = 2 \times 10^{-7}$ mbar) on the Ni(111) substrate kept at 500°C. The completion of a graphene layer is evidenced by the saturation of the C_{graph} peak after 15 min of deposition. Corresponding LEED patterns of the clean Ni(111) surface (a), the nickel carbide phase (b) and the complete layer of graphene (c) [125].

After obtaining a clean and epitaxial graphene/Ni(111) system, a 0.4 monolayer of FePc molecules was evaporated after long degassing of the powders, at a base pressure of 1.0×10^{-9} mbar. The thickness of the molecular film was monitored *in situ* through a calibrated quartz microbalance.

Circularly and linearly polarized XAS measurements at the Fe and Ni $L_{2,3}$ and N K absorption edges were performed in TEY mode. For all the measurements, the base pressure in the measurement chamber was 1.0×10^{-10} mbar and the temperature was 8 K, achieved by a liquid He bath cryostat. As the magnetic easy axis of the Ni(111) single crystal is along the plane, the external magnetic field **B**, which is always parallel to the incident photon beam was applied at grazing incidence, with an angle $\theta = 70°$ with respect to the normal of the sample surface. To avoid sample degradation induced by the synchrotron radiation, a reduced beam

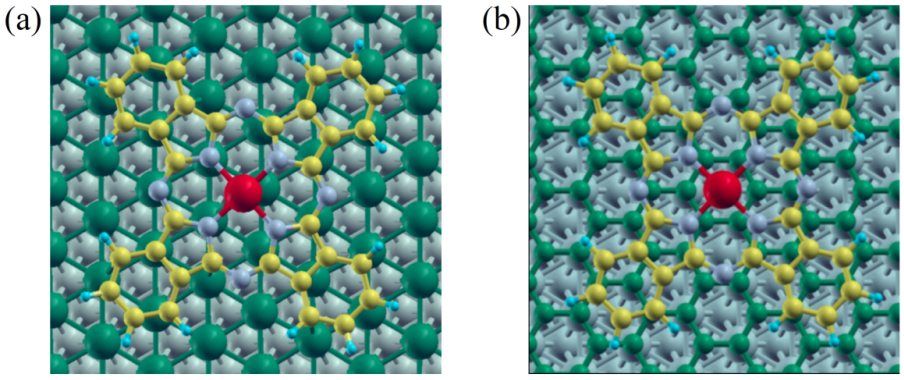

Figure 4.16.: Top-views of the (a) FePc/Ni(111) and (b) FePc/graphene/Ni(111) relaxed structures; the topmost substrate layer (Ni or graphene, respectively) is highlighted in dark green color [125].

intensity was employed and the XA spectra were carefully monitored to determine radiation-induced changes in time. The sample position was also frequently changed in order to constantly expose a non-irradiated part of the sample to the beam. The XMCD spectra are defined as the difference between the XAS spectra taken with the helicity of the incident photon antiparallel (μ^-) and parallel (μ^+) to the external field, normalized by the height of the XAS edge.

Theoretical calculations

DFT calculations have been performed by Dr. Valerio Bellini in Modena using the VASP code [106] using GGA-PBE exchange-correlation potential [131] and including van der Waals interactions in the semi-empirical method of Grimme [132]. With supercells consisting of a Ni lattice with 8×8 in-plane periodicity the two systems FePc/Ni(111) and FePc/graphene/Ni(111) have been simulated. In figure 4.16 a sketch of the relaxed structures of the two systems is presented. If not stated different, graphene is adsorbed in a top-fcc stacking, which was found to be energetically more favorable than the top-bridge one [133]. The chosen Ni lattice constant is 3.49 Å, and the atomic coordinates of the FePc molecule and of the topmost substrate layer (Ni or graphene), have been relaxed until forces were less than 2 meV/Å.

Magnetic interaction of the hybrid systems FePc/Ni(111) and FePc/graphene/Ni(111)

For both spin-hybrid systems FePc/Ni(111) and FePc/graphene/Ni(111) the interface spin coupling is studied with XAS and XMCD. Using XMCD technique combined with a variable magnetic field, the element-specific field-dependent

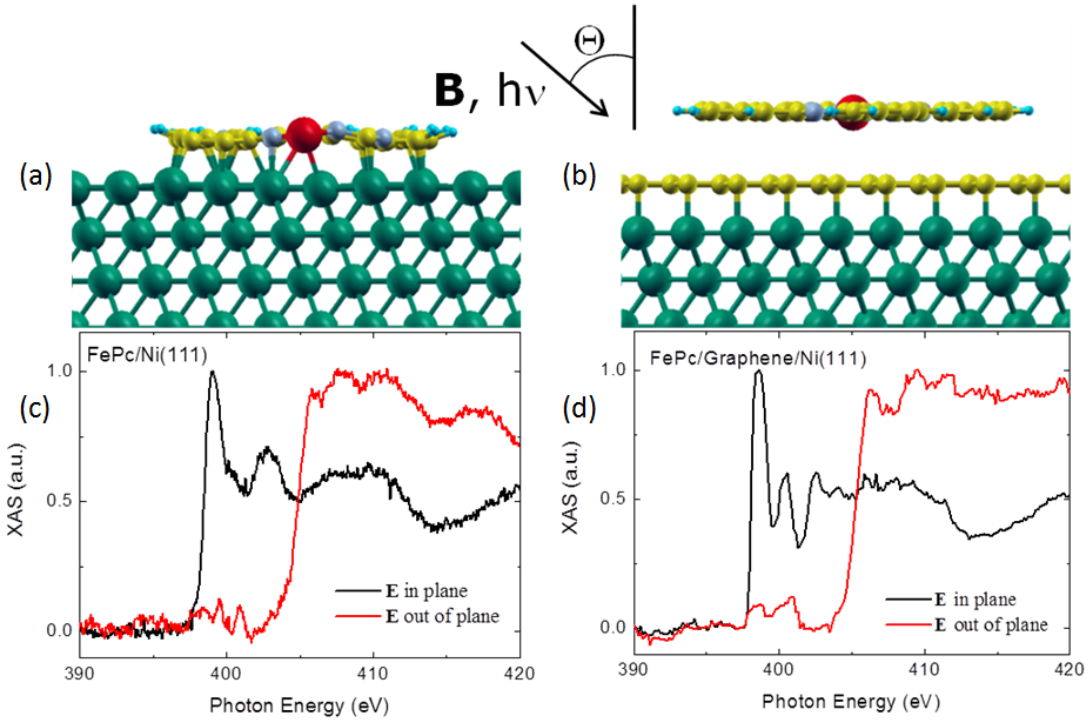

Figure 4.17.: (a, b) Schematic view of the system under investigation. The beam incidence angle is $\theta = 70°$ (grazing incidence). (c, d) Linearly polarized x-ray absorption spectra at the N K edge after background subtraction for the FePc molecules directly on Ni(111) (c) and on graphene/Ni(111) (d) [125].

magnetization of the FePc molecules and the Ni substrate have been determined at $T = 8$ K. The effect of graphene on the coupling is studied and the role of the graphene interlayer in transmitting the magnetic coupling is addressed. Additional DFT calculations support the experimental findings and point out the importance of the π orbitals of graphene.

Figure 4.17 shows a schematic view of the systems under study (upper panel) together with the N K edge absorption spectra of linearly polarized light for different photon incidence angles. As shown in the previous section, the angle-dependent absorption at the N K edge indicates the adsorption geometry of the molecule. Clearly visible are the π^* and σ^* resonances with strong polarization dependence at 397 eV and 405 eV, respectively. In agreement with other reports [21, 27] on similar molecules adsorbed on surfaces, this implies that the molecules lie flat and parallel to the surface. It is also evident that the π^* absorption peaks are sharper when the molecules are deposited on the graphene covered Ni surface, resembling the spectrum of the freestanding molecules [124, 134]. This suggests a weaker electronic interaction of N atoms with the substrate when the graphene interlayer is present

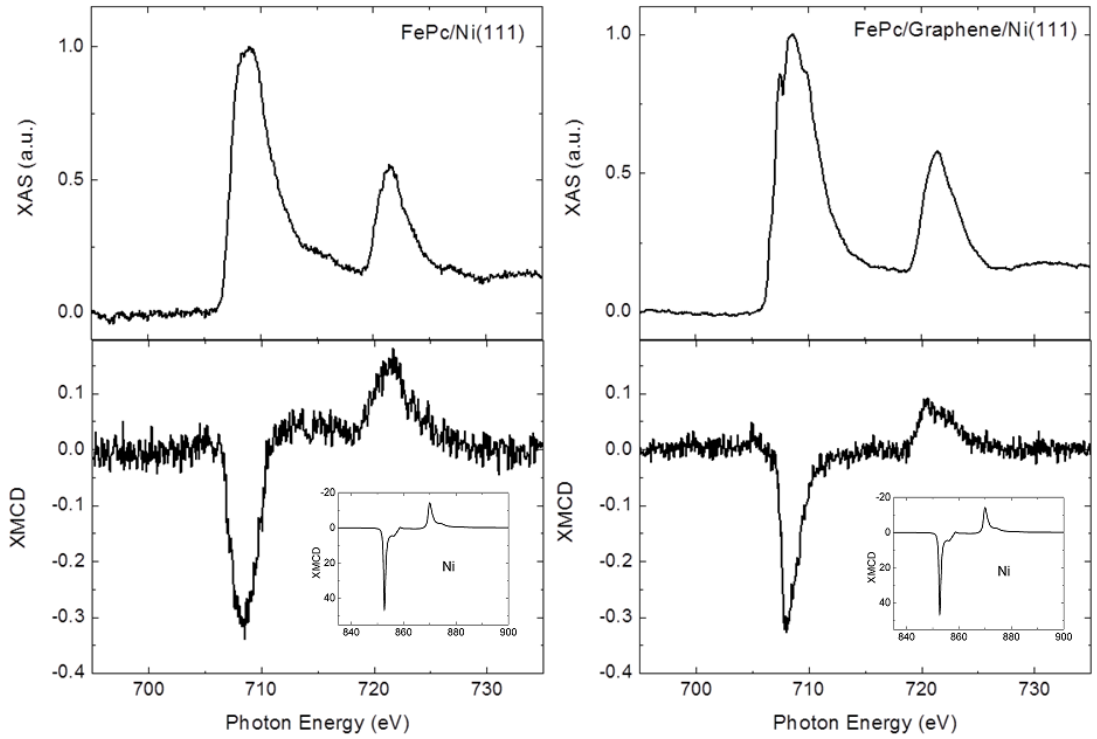

Figure 4.18.: Fe $L_{2,3}$ unpolarized XAS (upper panels) and XMCD (bottom panels) spectra for FePc molecules after background subtraction directly on Ni(111) (left) and on graphene/Ni(111) (right). The insets in the lower panels show the Ni $L_{2,3}$ XMCD spectra of the underlying substrates [125].

as it is similarly discussed in reference [27].

The focus however is on the magnetic properties of the spin-hybrid systems which were studied by XAS and XMCD at the Fe and Ni $L_{2,3}$ absorption edges, shown in the upper panels of Figure 4.18 for the FePc molecules deposited on Ni(111) (left) and graphene/Ni(111) (right). The normalized XMCD spectra (lower panels) show clearly a parallel alignment of the magnetic moments of the FePc molecules and the Ni substrate for both substrates, with and without the graphene interlayer. The Ni XMCD spectra are presented as insets in the lower panels, showing the same characteristics as the Fe $L_{2,3}$ edges with the L_3 XMCD reveals negative values and the L_2 XMCD reveals positive values. An antiferromagnetic coupling as seen for the system FePc/O/Co/Cu(100) can therefore be excluded. However, to verify a ferromagnetic coupling, a detailed field dependence is necessary. The spectra in figure 4.18 have been recorded at $T = 8$ K and $B = 5$ T, at which the paramagnetic molecule is expected to have a finite magnetization even without coupling to a ferromagnetic substrate.

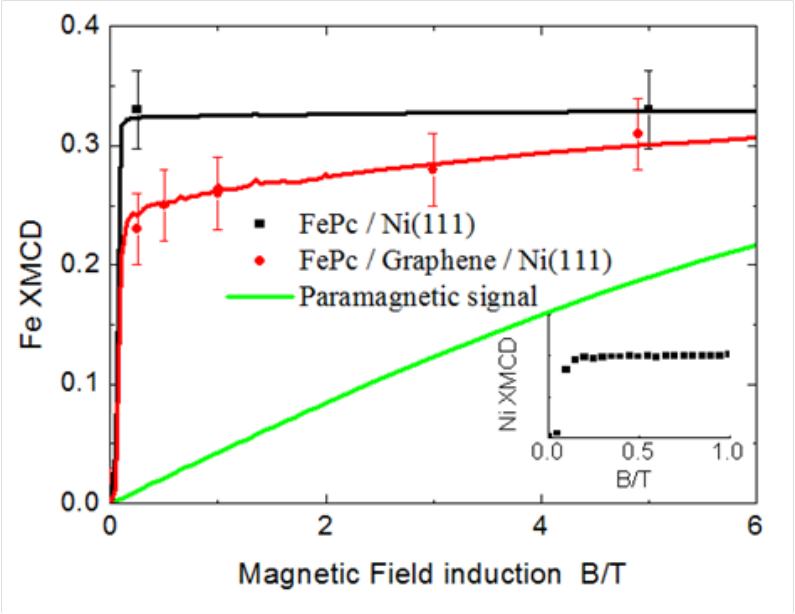

Figure 4.19.: Field-dependent XMCD intensity for FePc directly on Ni(111) (black) and on graphene/Ni(111) (red). Solid lines are the fitting curves following the model described in the text. For comparison, the curve corresponding to a paramagnetic signal is also shown in solid green. Inset: magnetization of the Ni(111) single crystal substrate [125].

The x-ray absorption spectrum (XAS) of the molecule deposited on bare Ni is very broad, pointing towards a strong Fe-Ni interaction, in agreement with what has been already reported [134]. The L_3 edge becomes sharper upon the insertion of graphene, and some of the characteristic lineshape details of the spectra associated with the non-interacting molecules, although not yet complete [124, 135], starts to develop. This illustrates the role of graphene as a decoupling layer for the electronic interaction.

To determine experimentally the magnetic interaction between the substrate and the molecules quantitatively, the magnetic properties were studied in dependence of an external magnetic field. The normalized XMCD intensities of the Fe and Ni L_3 edges are recorded as a function of the magnetic field, resulting in element-selective magnetization curves M(B), shown in figure 4.19. The figure presents four different magnetization curves, two of them corresponding to the molecules directly on Ni(111) (black squares) and on graphene/Ni(111) (red disks). When the molecules are on the bare Ni, the XMCD intensity is the same at 5 T and at 0.25 T, while a decrease of signal is observed when the graphene layer is inserted. Below 0.25 T the magnetization of the Ni(111) substrate gradually reduces to zero for $B = 0$ (see inset of figure 4.19) with vanishing coercive field, since the system

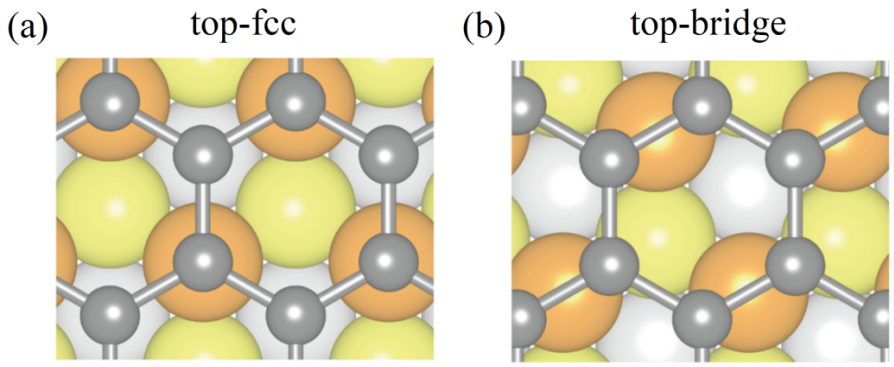

Figure 4.20.: Pictorial sketch of the (a) top-fcc and (b) top-bridge stackings of graphene on Ni(111); C (dark gray), first (top) Ni (dark orange), second Ni (yellow) and third Ni (light gray) atoms are highlighted [125].

breaks up into domains. As a consequence, no XMCD signal is found at zero magnetic field for the FePc molecule with or without graphene. To clearly demonstrate the ferromagnetic coupling of both systems, the expected magnetic behavior of uncoupled molecules is shown as green line for a paramagnetic spin $S = 1$ at the same temperature. That is what is usually reported for the FePc molecule in thick film or when deposited on non-magnetic substrates [22, 135]. The difference between the experimental data and the expected paramagnetic signal is due to the existence of a sizable magnetic exchange coupling between the molecules and the substrate [21, 98].

A quantitative determination can be made only from the experimental spectra by fitting with a simple Brillouin function $B_J(B)$ of the type

$$M_{Ni}(B) * B_J(B + B_{ex}), \tag{4.1}$$

where B_{ex} is the exchange field with the substrate and $M_{Ni}(B)$ is the Ni(111) magnetization. According to literature [27] and the experimental set-up, $J = 1$, $T = 8$ K were chosen, while anisotropic terms have been neglected. The fit yields a coupling of 0.5 ± 0.1 meV when the molecules are deposited on graphene/Ni(111). However, for the molecules adsorbed directly on Ni(111), only a lower limit of 1.2 meV for the coupling energy can be determined.

For a more precise description of the coupling mechanism and a quantitative determination of the magnetic interaction, DFT simulations of a FePc molecule deposited on a Ni(111) substrate, with and without the graphene decoupling layer, have been performed. At first it should be mentioned that different stackings of the graphene layer in Ni(111) are possible [136, 137]. Although top-fcc is the most abundant, top-bridge is also a possible stable solution (figure 4.20). In the following the results will be given for both top-fcc and top-bridge stackings, although if not explicitly stated, the analysis is relative to the top-fcc case.

Directly adsorbed on the Ni(111) surface, the FePc molecules are chemisorbed and the equilibrium average FePc-Ni distance is ≈ 2.2 Å, while, in presence of the graphene layer, the molecule-substrate interaction weakens, leading to a physisorption with larger adsorption distance of ≈ 3.1 Å (figure 4.17). Due to the rather strong surface-molecule interaction for FePc/Ni(111), some deviation from the molecular in-plane position occurs for the H atoms and the N atoms in direct contact with Fe. The interaction with Ni is also strong enough to shift the molecule to some amount from the initial hollow adsorption site and the Fe ion turns to sit in between a hollow and a bridge sites. As consequence of the rather low interaction on the graphene interlayer, the planarity of the molecule remains intact for FePc/graphene/Ni(111), and the hollow adsorption site is preserved. In both cases the Fe ion attains a spin S = 1 ($m_{Fe} = 2.00\ \mu_B$), in contrast to what has been observed for an Fe porphyrin on graphene/Ni(111) for the same adsorption site, where the spin of the molecule varies from $S = 1$ to $S = 2$ [24]. When the FePc molecule is in direct contact with Ni, charge transfer between the molecule and the substrate leads to sensible modifications in the spin moments of some of the Ni atoms below the molecule (from 0.68 μ_B to ≈ 0.30 - 0.40 μ_B), while the variation in the spin-polarization of the organic part of the molecule is very limited, and the net transferred polarization from the substrate is of small entity. The induced moment in some of the C atoms of the Pc ligand are only $\pm 0.01 - 0.02\ \mu_B$. The exchange coupling energy E_{ex}, defined as the difference between the total energy of antiparallel and parallel orientations of the Ni and Fe moments

$$E_{ex} = E_{AFM} - E_{FM}, \tag{4.2}$$

was calculated for both systems. In both cases E_{ex} is positive, indicating that a parallel orientation is favorable, and therefore confirms the ferromagnetic coupling between FePc and Ni(111) in both systems. While E_{ex} attains a value of 73 meV for FePc directly on Ni(111), the graphene interlayer reduces the coupling to 14 meV, which is approximately five times lower. Interestingly, the sign of the interaction is preserved, in agreement with the experimental results. Also for the top-bridge stacking a ferromagnetic coupling was found with $E_{ex} = 6$ meV. The larger value of the calculated exchange coupling as compared to experiments could be partly traced back to the well-known missing electronic correlation effects intrinsic in mean-field electronic structure calculations and it has been observed in previous similar studies [98]. The choice of U is also of moderate influence; test calculations have been performed for the top-fcc stacking by varying the value of U from 2 eV to 5 eV and E_{ex} is found to vary from 22 meV to 11 meV. The sign of the coupling is therefore robust upon variation in chosen U value.

The local density of states (LDOS) has been calculated to obtain additional information about the coupling mechanisms between the molecules and the substrates in the two systems. Figure 4.21 shows the orbital-projected and site-projected LDOS for the isolated FePc molecule (Fe-*d* in panel (a) and N-*sp*, C-*sp* in

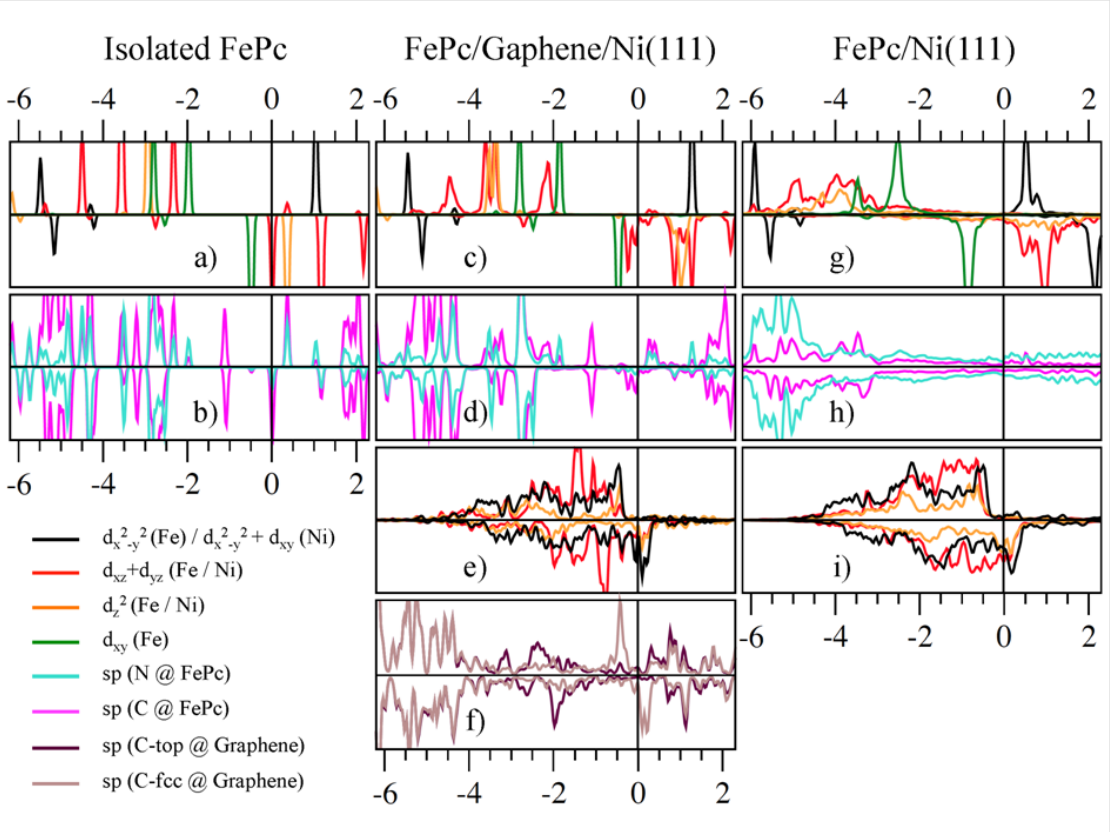

Figure 4.21.: Spin-resolved LDOS projection onto different orbitals of isolated FePc molecule [panels (a) and (b)], for the FePc/graphene/Ni(111) [panels from (c) to (f)] and FePc/Ni(111) [panels from (g) to (i)] systems. In panels (a), (c) and (g) the projection onto Fe-d orbitals of different symmetries [$b_{1g}/d_{x^2-y^2}$ (black), $e_g/d_{xz}+d_{yz}$ (red), a_{1g}/d_z^2 (orange) and b_{2g}/d_{xy} (green)] is given. Similarly in panels (b), (d) and (h) the projection onto N-*sp* (turquoise) and C-*sp* (magenta) is supplied. Panel (f) depict the sp-projected DOS onto the two different (by symmetry) C atoms of the graphene layer [top (dark brown) and fcc (light brown)] for the FePc/graphene/Ni(111) system, while panels (e) and (i) shows the d-projected DOS of the Ni top-most metal layer [$d_{xy}+d_x^2-y_2$ (black), $d_{xz}+d_{yz}$ (red) and d_{z^2} (orange)] in presence and absence of the graphene layer, respectively [125].

panel (b)), for the FePc/graphene/Ni(111) (Fe-d in panel (c), N-sp, C-sp in panel (d), Ni-d of the top-most metal layer in panel (e) and C-sp of the graphene layer in panel (f)) and for the FePc/Ni(111) (Fe-d in panel (g), N-sp, C-sp in panel (h) and Ni-d of the top-most metal layer in panel (i)) systems. Under D_{4h} ligand field, the d-orbitals of Fe splits into d_{xy} (b_{2g}), d_{xz}+d_{yz} (e_g), d_z^2 (a_{1g}) and $d_{x^2-y^2}$ (b_{1g}) symmetry, with x and y axes are along the Fe-N bonds. The LDOS in figure 4.21 (a) and (b) shows a hybridization between the Fe d orbitals and the sp states of C and N. This leads to a further splitting of the energy levels so that several peaks are observed in figure 4.21 (a). A small antiparallel moment of $\approx 0.02\ \mu_B$ is induced on the four N atom which bonds to Fe, while residual small polarization is present in the rest of the molecule. The LDOS of the isolated molecule is consistent with a ^3E_gA electronic configuration, which is one of the configurations reported in the literature [138–140].

If the molecule is not isolated, but adsorbed on the graphene/Ni(111) substrate, hybridization between the out-of-plane orbitals e_g (red) and a_{1g} (orange) occurs, visible in figure 4.21 (c). The broadening and further splitting of the relative peaks give a clear indication for the hybridization. The hybridization of graphene and Ni depends on the stacking, as shown in the LDOS of graphene (figure 4.21 (f)) and Ni (figure 4.21 (e)). Graphene in the top stacking hybridizes between -3.5 eV and -1.5 eV, while the hybridization between graphene in Ni in the fcc stacking is in the vicinity of the Fermi level [141].

The N and C atoms of the adsorbed FePc molecule which hybridize with the Fe d orbitals show similar behavior (figure 4.21 (d)). A strong interaction is observed, when the molecule is directly adsorbed on the Ni surface. The a_{1g} (orange) peak of Fe broadens out and only some character in the majority channel around -4 eV from the Fermi level is retained (figure 4.21 (g)), where hybridization with the lower energy part of the Ni d states takes place (Figure 4.21 (i)). A sensible interaction between the π electron system of the organic part and the Ni states can be observed from the LDOS of the N and C atoms of the molecule (figure 4.21 (h)). A continuum of states above -3 eV from E_F matches the continuum of the sp metal states below.

To study the coupling mechanism in more detail, the spin-density distribution at the molecule-surface interface is calculated. Figure 4.22 shows the three-dimensional isosurfaces and zooming in the molecule-graphene contact region. The figure visualizes the spin communication channels which form in the ferromagnetic case (figure 4.22 (a)). The extended π orbitals of the C atoms outstretch farther in the spin-up polarization (light green lobes) than in the spin-down polarization (light blue lobes). The channels are non-existent in the antiparallel case (figure 4.22 (b)), because of the mismatch of the spin index between electrons belonging to the molecule and to the graphene layer. In figure 4.22 (c) and (d), the matching

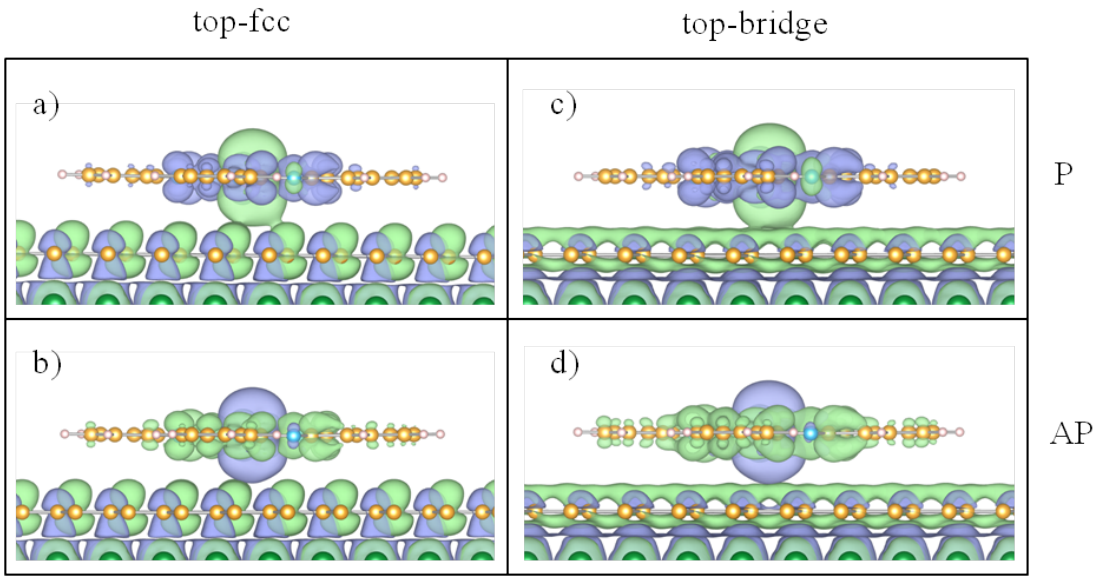

Figure 4.22.: Three-dimensional contour plots of the spin density distribution at the FePc/graphene/Ni(111) interface for top-fcc (a) and (b) and top-bridge (c) and (d) stacking; (a) and (c) are for the parallel, (b) and (d) for the antiparallel coupling between the Fe and Ni spin moments. Light green (light blue) color refers to an excess of spin up/majority (down/minority) electrons. An isovalue of ± 0.0003 electrons has been considered [125].

is similar when the graphene stacks in the top-bridge registry on Ni and the ferromagnetic alignment is preferred.

For Co porphyrin, the insertion of a graphene layer was shown to switch the coupling from ferromagnetic to antiferromagnetic [98, 99, 142], while for Fe porphyrin on graphene/Ni behaves similar to the present system. The different coupling mechanisms result from different orbitals of the $3d$ ion involved in the spin communication between the molecule and the magnetic substrate. It is also worth to mention that the sign of the coupling is independent of the type of stacking of graphene on Ni, in contrast to what was calculated in reference [98].

In conclusion, the coupling type of FePc and the ferromagnetic substrate is different when the graphene interlayer is inserted into the system compare to the O interlayer in the previous section. The O interlayer forms a superstructure of half a monolayer O on Co(100) with atomic character. In contrast, the C atoms form a monolayer of graphene which behaves as continuous layer that becomes polarized due to the hybridization with the substrates and mediates the magnetic interaction by its extended orbitals. This demonstrates the possibility to engineer the coupling interaction between a magnetic substrate and a molecule by changing the interlayer

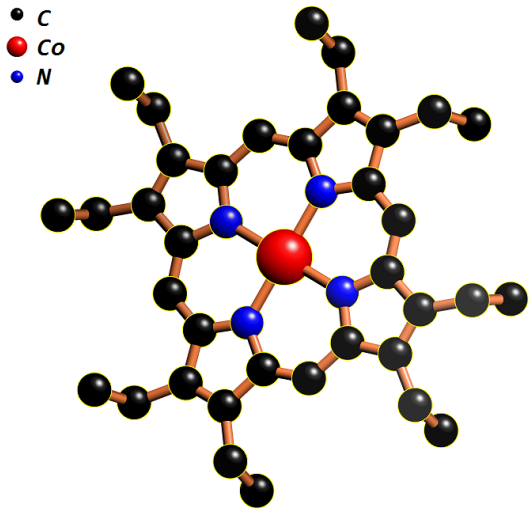

Figure 4.23.: Sketch of the CoOEP molecule.

or the molecular components. After the coupling of molecules via graphene was only reported very recently, publications followed with different approaches to study the coupling effects of this promising hybrid metal-organic system [24, 98, 99, 142].

4.2. Tuning the magnetic properties of Co-porphyrin

After the presentation of the successful magnetic coupling of FePc to ferromagnetic substrates in the previous section, here a similar study on CoOEP molecules is presented. It was clearly shown for the systems with FePc that the substrate has a huge impact on the coupling mechanism. While porphyrin an phthalocyanine molecules couple ferromagnetically, when they are in direct contact with a ferromagnet, it was shown in the previous sections that an interlayer of O switches the coupling between FePc and Co(100) from ferro- to antiferromagnetic, while the ferromagnetic coupling between the molecules and a Ni(111) substrate is retained by insertion of an interlayer of graphene.

Keeping the substrate and replacing the molecule will reveal the role of the molecular components involved in the magnetic coupling. Not only the ligand, but also the metal center is different in CoOEP and FePc. A sketch of the molecule is presented in figure 4.23, showing the eight ethyl groups with some perpendicular components and only four N atoms compared to eight in a Pc molecule. This section is based on reference [99]: [D. Klar *et al.*, Phys. Rev. B, **89**, 144411 (2014)].

4.2.1. Magnetic coupling of CoOEP to a ferromagnet via graphene

Experimental details

The XAS measurements in total electron yield were performed at the undulator beamline DEIMOS at SOLEIL. In the cryomagnet a magnetic field up to 7 T can be applied and a temperature of 2 K at the sample holder can be reached. This results in a temperature of approximately 2.8 K on the sample surface. With the element-specific XMCD technique at the Co and Ni $L_{2,3}$ edges the magnetic field dependence of the net magnetization of the Ni(111) crystal and the CoOEP molecules was analyzed. The samples were prepared *in situ* at a base pressure of 10^{-10} mbar in the DEIMOS preparation chamber. An epitaxial layer graphene on top of the clean Ni(111) single crystal *in situ* was produced by heating the crystal in a propylene atmosphere, see 4.1.3. Subsequently the CoOEP molecules were thermally evaporated onto the graphene covered Ni(111) crystal while the substrate was held at room temperature.

Computational details

The calculations supporting the experimental data have been performed by Dr. Sumanta Bhandary and Dr. Biplab Sanyal in the group of Olle Eriksson at Uppsala University. First principle DFT calculations have been performed with a full potential plane wave based code VASP [106, 143]. The unit cell used consisted of a slab of three Ni layers in the (111) direction having 108 atoms along with a graphene monolayer with 72 atoms (6×6 supercell) on top of the slab. The molecule was modeled with 37 atoms, building a CoP (not a CoOEP). The CoP is a simpler form without the eight outer ethyl groups. The simulation cell therefore consists of 217 atoms. The magnetic centers are chosen to be at least 15 Å apart from each other in the lateral direction. The lowest Ni layer was fixed with the in-plane bulk Ni constant and all the other atomic positions were relaxed. A DFT+U approach was employed within the Hubbard model [144] to incorporate strong Coulomb interaction with the Coulomb parameter U and exchange parameter J fixed as 4 and 1 eV respectively for Co d-orbitals. These parameters have been shown [145] to reproduce certain experimental results for $3d$ transition metal centered porphyrin molecules. All the calculations were performed including an empirical form of dispersion correction given by Grimme [132].

Orientation of the adsorbed molecules

Porphyrin and phthalocyanine molecules have a similar planar structure with a four-fold symmetry and therefore the porphyrin molecule is expected to adsorb in a

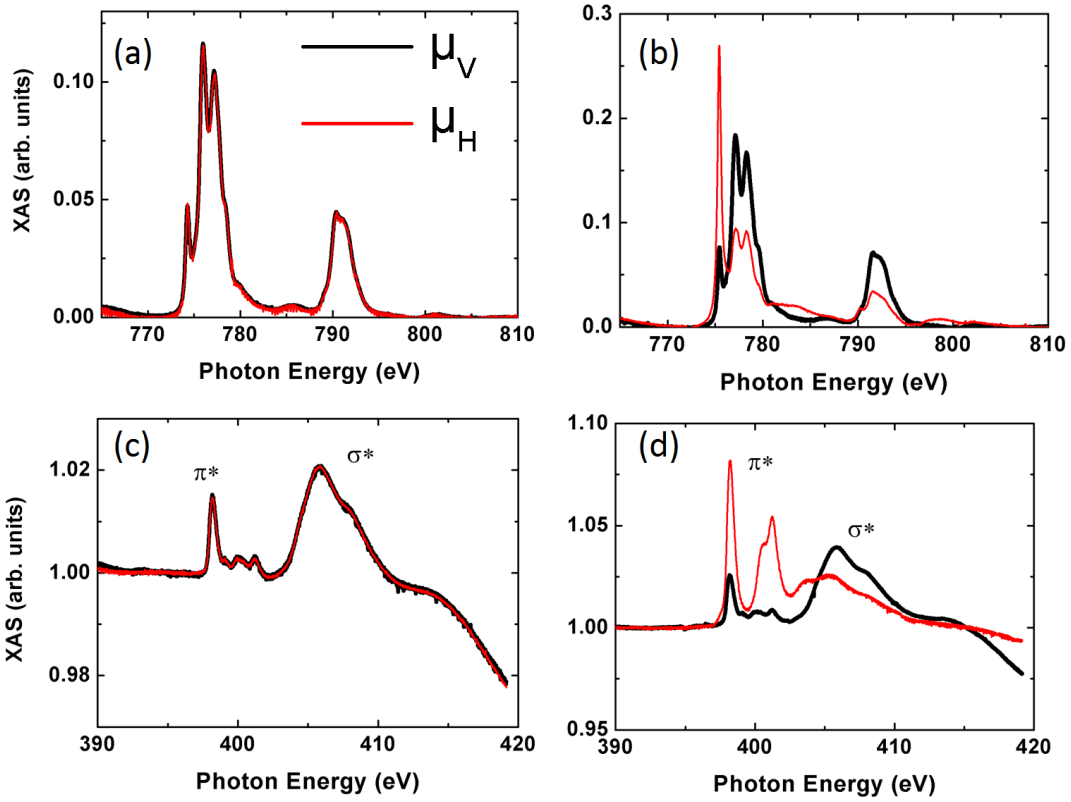

Figure 4.24.: (Absorption spectra for $\Theta = 0°$ (left) and $\Theta = 70°$ (right) incidence with linearly vertically (μ_V, black) and horizontally (μ_H, red) polarization at the Co $L_{2,3}$ edges (a) and (b) and the N K edge (c) and (d) [99].

lying configuration as well. However, due to the additional out-of-plane ligands, the molecule is not perfectly planar and can therefore show a different orientation on the surface. Hence, the orientation of CoOEP/graphene/Ni(111) is studied via XLD at the Co $L_{2,3}$ and N K edges for normal and grazing incidence. Figure 4.24 shows the results of the XLD measurements which clearly indicate a lying configuration of the molecule. While for $\theta = 0°$ the absorption spectra of horizontally and vertically polarized are identical at both, the Co $L_{2,3}$ (a) and N K (c) edges, there is a clear difference under $\theta = 70°$ incidence (b) and (d). Here the symmetry of the molecule is important, which is four-fold in the Pc plane, but only two-fold perpendicular to the Pc ring. The $\boldsymbol{E}$ vector of the x-ray is turned by 90° between vertical and horizontal polarization and will therefore not detect any dichroism, if $\boldsymbol{E}$ is parallel to the Pc ring, corresponding to perpendicular x-ray incidence. However, for grazing incidence there must be dichroism due to the lower symmetry. The XLD detects the element-specific anisotropy in the electronic distribution. If the molecules are not oriented, but are random on the surface, no dichroism will appear. Since the XAS is the integration over billions of molecules in all possible adsorption geometries, the

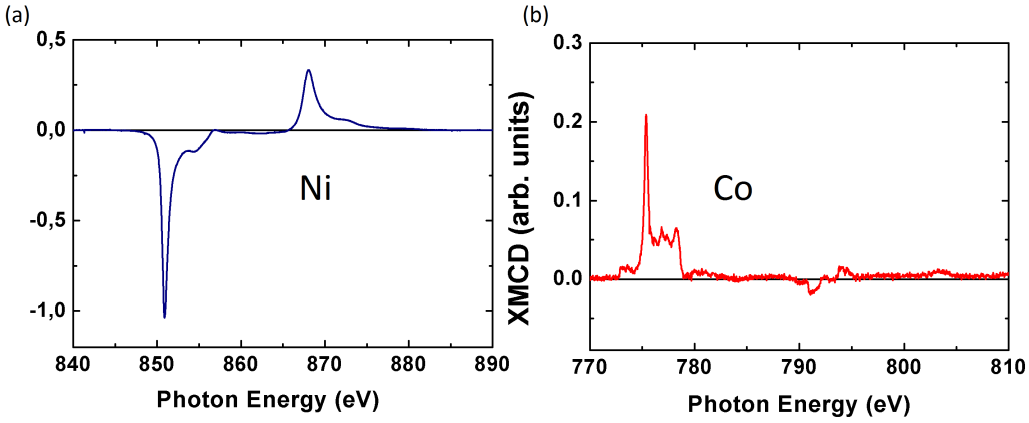

Figure 4.25.: XMCD spectra of at the Ni (a) and Co (b) $L_{2,3}$ edges of CoOEP molecules on a graphene covered Ni(111) single crystal. The spectra have been recorded under grazing x-ray incidence ($\theta = 70°$) at $T = 2.8\ K$ in an external magnetic field of $B = 100$ mT to saturated the magnetization of the Ni crystal.

electronic distribution of randomly oriented molecules is isotropic. The symmetry argument of σ^* and π^* orbitals of the N atoms from the previous section is valid also for the CoOEP molecule. However, the fine structure of the N K edge is slightly different between the two molecules. This is certainly a result of the two non-equivalent N orbitals in the Pc molecules, resulting in a superposition of different absorption contributions, as in detail discussed for the FePc molecule. The σ^* and the π^* contributions are more pronounced than for the FePc molecule at grazing incidence. For a perfect planar molecule adsorbed flat on the surface, no π^* contributions are expected for normal incidence. Either the binding angles within the molecules are tilted due to the surface interaction or the whole molecule is tilted with respect to the surface. The ladder assumption is more likely, since the interaction with the graphene surface is expected to be weak, but the ligands of the OEP can cause a tilting of the molecules.

Results on the magnetic coupling

Unlike the FePc molecules, which couple ferromagnetically to the Ni(111) via graphene, the CoOEP molecule are antiferromagnetically coupled as show in figure 4.25. The figure shows the XMCD spectra for the underlying Ni film and the CoOEP molecules at $B = 100$ mT and $T = 2.8$ K. Since the easy axis of the Ni single crystal as well as the CoOEP molecules is parallel to the surface, the absorption spectra are recorded under grazing incidence ($\theta = 70°$). The sign of the XMCD at the $L_{2,3}$ edges of the two spectra are opposite, clearly

indicating antiparallel magnetization of the Ni crystal and the CoOEP molecules. This has also been shown by Hermanns *et al.* [98]. Instead of a Ni(111) single crystal, in their experiment they prepared a Ni film on a W(110) surface, resulting in a Ni(111) surface similar to the experiment presented here. The Co XMCD shows the typical fine structures of a CoOEP molecule with Co in a 2+ oxidation state. It is noticeable that the L_3 XMCD is infinitesimally small, indicating a large orbital moment of Co in comparable size to the spin moment [142].

DFT+U calculations have been performed to investigate the magnetic coupling between the molecules and the substrate and the role of graphene. The antiferromagnetic coupling between the Ni surface and the Co moment demonstrated in the experimental data is confirmed by the calculations. However, the coupling strength is much smaller compared to chemically adsorbed molecules on magnetic surfaces [146]. The graphene layer weakens the interaction of the substrate and the molecules significantly, resulting in physisorbed CoOEP molecules. The C atoms in graphene on Ni(111) form two sublattices with non-equivalent C atoms, C_A and C_B. The C_A sublattice atoms are chemically bonded to Ni atoms due of a perfect lattice matching. The C_B sublattice atoms remain sp^2 bonded. Consequently on the different sublattices one finds different induced magnetizations. To better understand the effect of the molecules adsorption position on the magnetic coupling, three different adsorption geometries are studied. The CoP can adsorb on top of C_A, C_B and in the middle of the graphene hexagon, which I will refer to as Top-A, Top-B, and Hexagon, respectively. The induced moment of C_A is calculated to 0.018 μ_B and aligns antiparallel to the Ni moment while C_B gets magnetized parallel to the Ni moment with a moment of 0.03 μ_B, yielding a ferrimagnetic graphene layer. The most stable adsorption position is the Top-A with a distance of 3.07 Å over the graphene layer, while the Top-B layer is 14.6 meV higher in energy with an adsorption distance of 3.04 Å. The Hexagon position results in the highest energy (23.5 meV higher than Top-A) and the largest distance to the graphene layer (3.11 Å).

Despite the fact that the three adsorption geometries are non-equivalent and the magnetization within the two C sublattices is antiparallel, the magnetic coupling between the Ni substrate and the CoP molecules is antiparallel for all three adsorption positions. The total energy calculations reveal exchange coupling energies $E_{ex} = E_{FM} - E_{AFM}$[1] of 4.2, 9.9 and 3.1 meV/cell for Top-A, Top-B and Hexagonal adsorption sites respectively. These values for E_{ex} are much smaller than the ones calculated for the similar system in reference [98]. While O as a buffer layer has a saturation coverage at half a monolayer, e.g. on Co/Cu(100) [21, 27], leading to well separated and localized O p_z orbitals, the C π orbitals build a delocalized π-band. Due to this delocalization, the molecules couple antiparallel, independent

[1] where E_{FM} and E_{AFM} represent the total energies in the ferromagnetic and the antiferromagnetic orientation, respectively

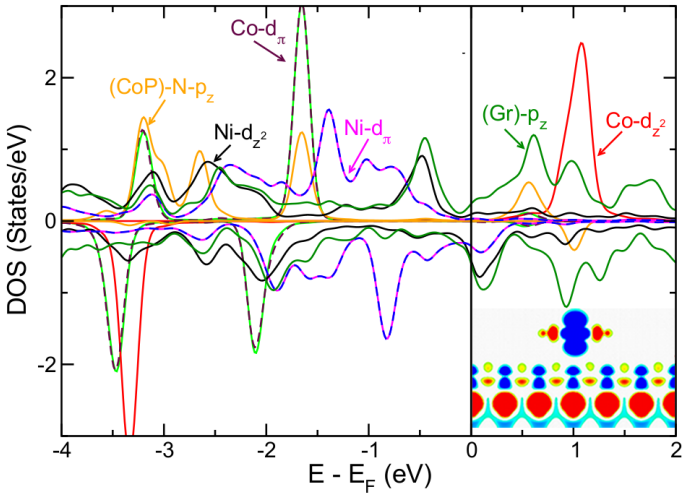

Figure 4.26.: Out-of-plane contribution to the DOS, resolved on C, N and Co states projected onto the Co porphyrin molecule, labeled (CoP)-Co, (CoP)-C, (CoP)-N. Also shown is a projection of graphene C atoms, labeled (Graphene)-C atoms. Projections are done on specific m_l projected orbitals. (Inset) Magnetization density cross section, which depicts antiferromagnetic coupling between Ni and Co along with graphene sublattice magnetization. Red and blue colors indicate positive and negative densities on CoP (on top), graphene (middle layer) and first Ni layer of the unit cell [99].

of their adsorption site.

The density of states of the out-of-plane orbitals for (CoP)-Co, (CoP)-C, (CoP)-N, (Graphene)-C, and surface layer Ni for the most stable Top-A configuration have been calculated to get a deeper understanding of the exchange interactions (figure 4.26). The inset shows the magnetization density plot, where the antiferromagnetic coupling is clearly visible by the colors of Ni (red) and Co (blue). The magnetization density in Co comes solely from the singly occupied d_{z^2} orbital, which couples antiferromagnetically with the Ni moments. The Ni $3d$ and the graphene p_z states hybridize, resulting in a stronger chemical interaction than between graphene and CoP. Since there is no hybridization between Ni and Co visible, a direct exchange can be excluded. The magnetic coupling is solely mediated via the graphene states.

The orbital dependence of the susceptibility is presented in figure 4.27. Interestingly the in-plane orbital contributions are almost zero, while the out-of-plane (d_π=d_{xz}+d_{yz}) contribution is significant below the Fermi energy. At the Fermi energy d_{xz} and d_{yz} have only very small contributions, the major contribution comes

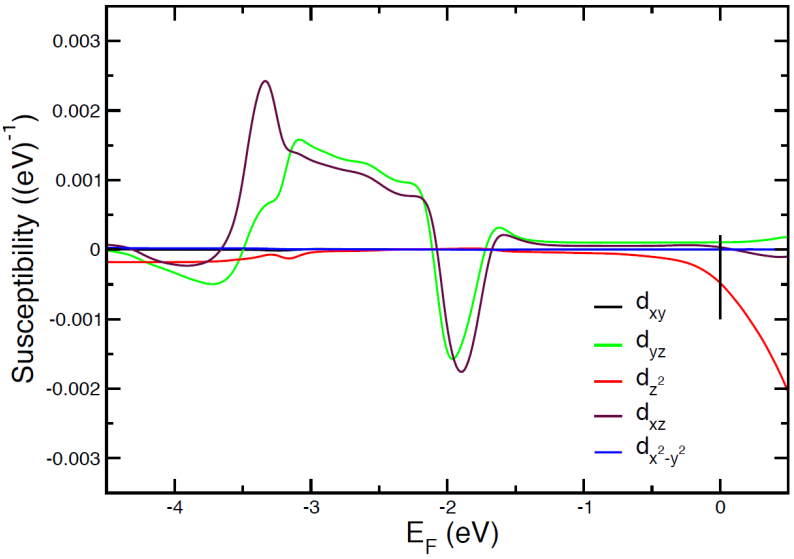

Figure 4.27.: Orbital-dependent susceptibility as a function of Fermi energy. Note the dominance of the d_z^2 orbital at the Fermi energy E_F=0, relevant for the present system [99].

from the d_{z^2} orbital (red line). Also the contributions for d_{z^2} and $d_{xz/yz}$ orbitals are of different sign meaning that the total contribution will be slightly reduced.

4.2.2. Field-regulated switching in a molecular multilayer system

The antiferromagnetic coupling between the molecules and the magnetic substrate via graphene enables further investigations of coupling effects in this spin-hybrid system. In the following, the molecular interlayer coupling is studied for three layers of CoOEP molecules on graphene/Ni(111). Field-dependent XMCD measurements determine the coupling between the molecular layer and the results are supported by DTF calculations.

Figure 4.28 shows the normalized XMCD spectra at the Ni and Co $L_{2,3}$ edges for the system 3 ML CoOEP/graphene/Ni(111) for two different magnetic fields of 500 mT and 5 T. Sketches of the sample design are given on top of the figure. The black arrows illustrate the magnetic moments of each Co ion, while the white arrow represents the macroscopic magnetization of the Ni crystal. The spectra have been recorded at T = 2.8 K and $\Theta = 70°$. The change of the magnetic field does not affect the Ni XMCD (inset, blue line), but has a drastic effect on the Co XMCD (red line). The XMCD changes the sign from positive to negative at the L_3 edge and *vice versa* at the L_2 edge, while the line shape remains unchanged. Why does the orientation of the Co magnetization changes, while both, the external

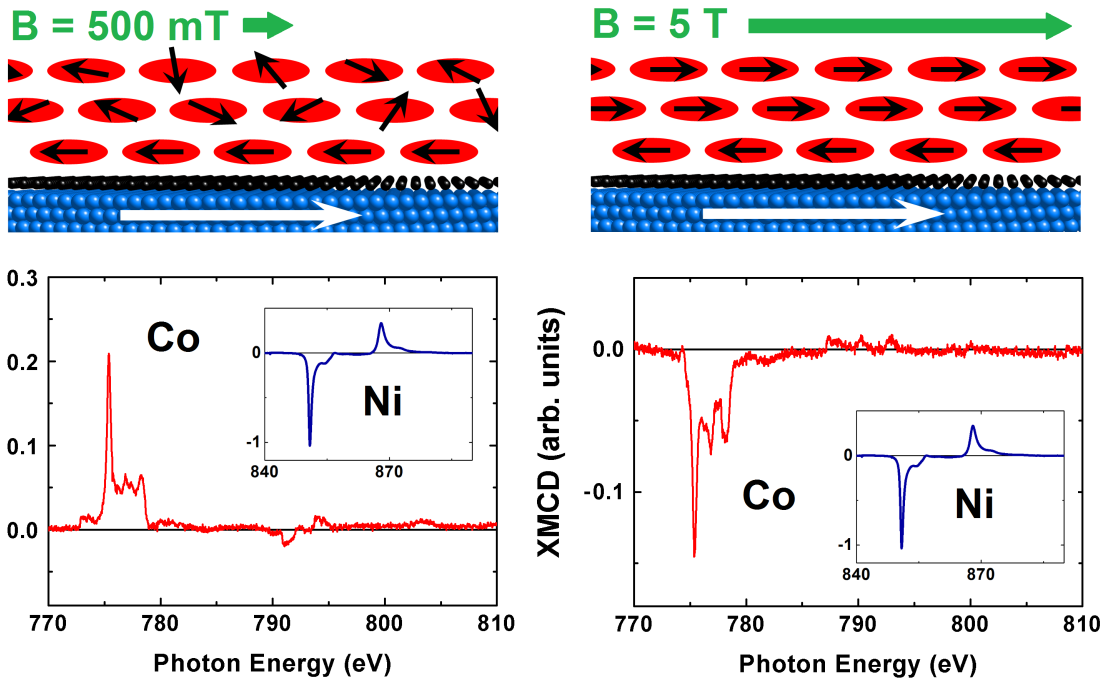

Figure 4.28.: Top: Sketch of the sample: 3 ML CoOEP/graphene/Ni(111). The white and black arrows indicate the directions of the magnetic moments of Ni (blue) and Co (red) in a low magnetic field of 500 mT (left) and in a high magnetic field of 5 T (right). Bottom: XMCD at the Co $L_{2,3}$ edges of the CoOEP molecules in the low magnetic field (left) and in the high magnetic field (right). Insets show the XMCD at the $L_{2,3}$ edges of the saturated Ni crystal at 500 mT and at 5 T. All spectra are recorded at T = 2.8 K and $\Theta = 70°$ [99].

magnetic field and the Ni magnetization remain in the same direction. The only changing parameter is the strength of the external field. The origin of the behavior of the Co magnetization is the existence of two individual contributions which have completely different dependence on the external magnetic field. The Ni film is fully saturated in a field of $\approx$ 200 mT and as discussed in the previous chapter, the first molecular layer is antiferromagnetically coupled to the Ni film. This coupling is rather weak, but very large compared to the Zeemann energy of the magnetic field ($E_{ex} >> E_{Zeemann}(5T)$). Hence, the first molecular layer is not affected by the external field and remains antiferromagnetically coupled to the Ni film which, in turn, is parallel to the external field. The second contribution comes from the second and third molecular layers. These layers are not (or very weakly) coupled to the first layer. Hence, they behave like paramagnetic molecules and show a strong field dependence. Figure 4.29 shows a detailed field dependence of the XMCD at the Co L_3 edge for various external magnetic fields. Between 2 T and 3 T the XMCD changes its sign, meaning that the Co magnetization switches. XMCD

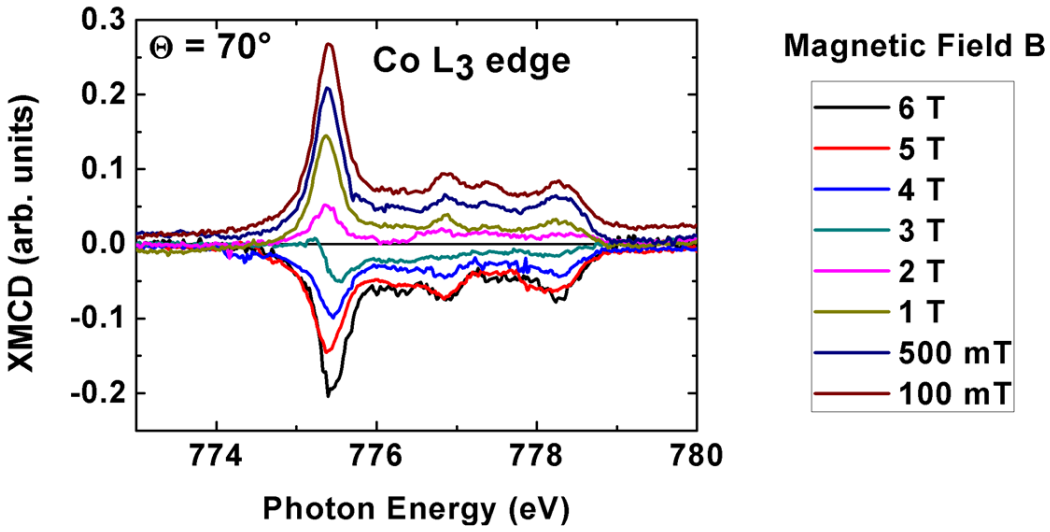

Figure 4.29.: XMCD spectra at the Co $L_{2,3}$ edges of 3 ML CoOEP molecules on graphene/Ni(111) for eight different magnetic fields between 100 mT and 6 T. The spectra have been recorded at an x-ray incidence angle of $\Theta = 70°$ and at $T = 2.8$ K [99].

cannot distinguish between the individual layers and images the net magnetization of all CoOEP molecules. The first layer is oriented antiparallel to the Ni film in a small external field and the other two layers are randomly oriented due to spin fluctuations of the paramagnetic molecules (figure 4.28 (left)). These Co magnetic moments point into various directions and add up to a negligibly small magnetization in the field direction, so the net magnetization is dominated by the first layer and is therefore antiparallel. If a high magnetic field is applied, the second and third layers are aligned parallel to the external field, while the first layer still remains antiparallel. The net magnetization is however, parallel to the Ni magnetization (figure 4.28 (right)). The value of the magnetization is approximately the same as for the low field case. One layer compensates the magnetization of the first layer and the magnetization of the other layer is detected as the net magnetization.

To confirm this assumption from the experimental data, the interaction between the molecular layers has been calculated, shown in figure 4.30. In a perfectly aligned sample with three layers of CoP molecules, the calculations reveal an antiferromagnetic interlayer coupling between CoP molecules. The coupling energy is large enough to be stable in magnetic fields up to 5 T and therefore no field-dependent net magnetization would be expected. The optimized geometry has the two Co atoms in two consecutive layers shifted laterally, which is also discussed

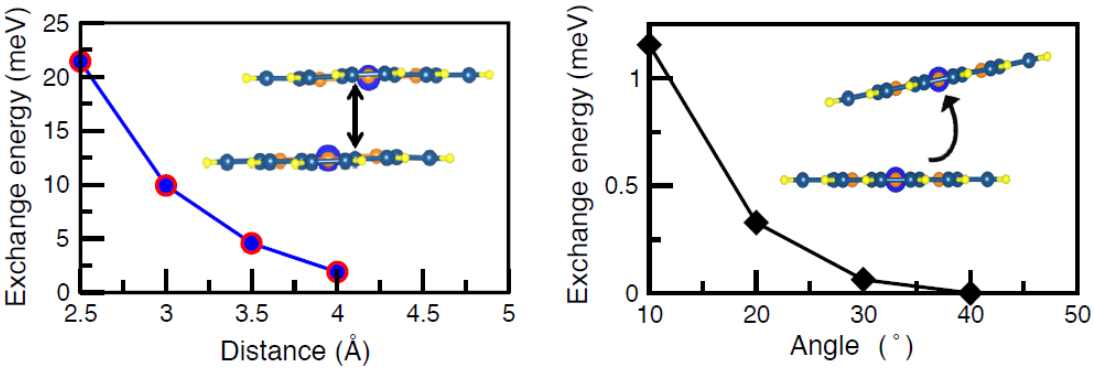

Figure 4.30.: Exchange energy between the molecular layers depending on the distance and the relative angle and schematic views of relative separation and rotation between two CoP [99].

in literature for CoPc [147]. These theoretical findings clearly do not agree with the experimental data presented in figure 4.29. To understand potential differences between the experiment and the calculations, the effect of slight variations from the perfect geometry were implemented for the determination of the exchange energy. The spatial separation between the parallel layers reduces the exchange strength considerably due to lowering of orbital overlap, while randomness in the orientation has a higher impact in reducing interlayer exchange coupling. In figure 4.30, the sharp fall of exchange energy due to increasing separation between two CoP layers and angular deviations between them is shown. An increased distance between two Co atoms and a relative rotation of some degrees between two molecules reduces the exchange energy to a fraction of the value and also causes the type of orbitals participating in the exchange to be modified. Here it is important to mention that the model assumed a CoP, a flat molecule without any out-of-plane components. In the experiment, however, CoOEP molecules are studied, whose ligands are partially out-of-plane and therefore cause different adsorption angles and distances. This results in a drastic decreasing of the exchange interaction between the layers.

In figure 4.31 the net magnetization of the system is shown for Co and Ni in dependence of the external magnetic field for -5 T$< B <$ 5 T. In both cases, the measurements were performed at constant photon energies of 775.4 eV for Co and 850.9 eV for Ni, at which the XMCD intensity is maximum, and normalized to pre-edge energies of 772.0 eV and 845.0 eV, respectively, while the magnetic field was varied. As already discussed in figures 4.28 and 4.29, the Ni magnetization is constant for external field values above $\approx$ 200 mT and the Co magnetization switches in increasing fields from antiparallel to parallel. The switching field is approximately $B_S = 2.5$ T. At $\approx$ 200 mT, where Ni reaches the saturation value, the Co magnetization rises to its maximum value, antiparallel to the field, demonstrating the antiferromagnetic coupling. In higher fields, the Ni magnetization

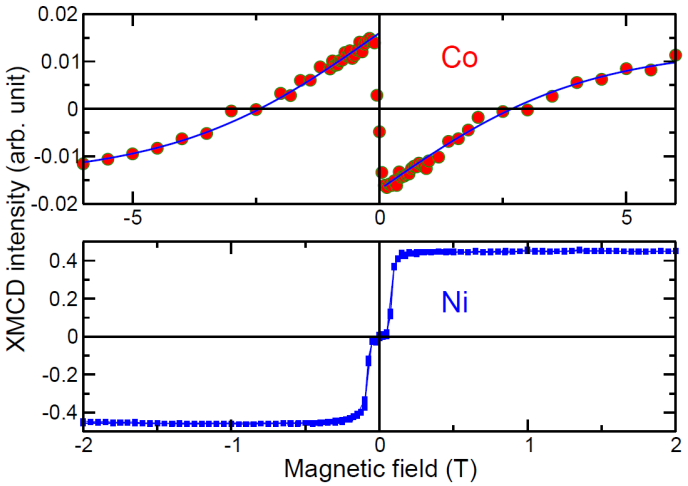

Figure 4.31.: Magnetization curves between -2 T and +2 T for Ni (blue) and between -6 T and +6 T for Co (red), measured at $\Theta = 70°$ and $T = 2.8$ K. The continuous line shows the fitted Co magnetization (see text for details) [99].

remains constant, while the absolute value of the Co XMCD signal decreases and reaches zero at a field of nearly 2.5 T. At this point, the magnetization of the molecules in the second and third layers annihilate the magnetization of the first one. In higher fields, the net magnetization switches its sign, because the amount of parallel aligned magnetic moments is higher than the antiparallel magnetic moments of the first layer. The experimental findings and interpretations of the data can be represented by a simple Brillouin function describing a paramagnetic behavior. The Brillouin function of the first layer is modified with the exchange field B_{ex} representative for the antiferromagnetic coupling with the Ni substrate:

$$M(B) = M_1 tanh(\mu_B(B - B_{ex})/k_B T) + M_{2,3} tanh(\mu_B B/k_B T) \tag{4.3}$$

The equation gives a superposition of the two different contributions with S=$\frac{1}{2}$ and $B_{ex} = 72$ T, the exchange field between the Co moment of the first molecular layer and the Ni surface, obtained from the DFT+U calculations. The fitting parameters M_1 and $M_{2,3}$ represent the saturation magnetizations of the first layer and the second and third layers, respectively. Since the exchange field is much larger than the external magnetic field, $tanh((B - B_{ex})/k_B T)$ is approximately -1, leading to a field-independent antiparallel contribution $-M_1$ originating from the first layer. The fit directly leads to the ratio between M_1 and $M_{2,3}$ which is $M_{2,3} = 1.8\,|M_1|$, indicating that the film thickness is approximately 2.8 ML which is in good agreement to the assumption of 3 ML. The calculated field-dependence and experimental results fit almost perfectly. The assumption of two different contribution, a constant antiparallel magnetization plus a paramagnetic contribution is supported by this good agreement.

5. Magnetic properties of single molecule magnets of the type $LnPc_2$

5.1. Introduction

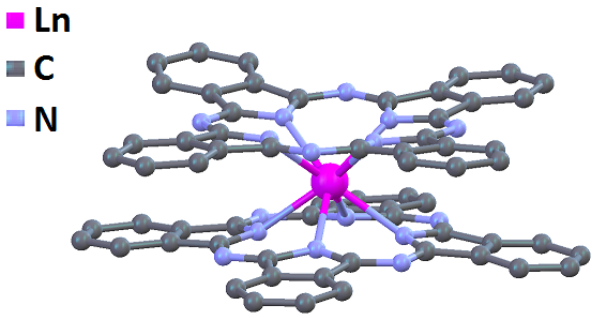

Figure 5.1.: Sketch of the $LnPc_2$ molecule.

In this chapter the focus is on spin-hybrid systems, including $LnPc_2$, a class of SMM or single ion magnets. These molecules have obvious structural similarities with the FePc molecules described in the previous chapter. A $LnPc_2$ consists of two parallel Pc rings at a distance of approximately 4 Å and a Ln^{3+} ion centered in between (figure 5.1). Though there are structural similarities, the magnetic properties are mainly given by the central Ln ion. The magnetism of Ln in contrast to Fe is given by $4f$ electrons, leading to its characteristic properties that differ completely from $3d$ transition metal magnetic properties. The $4f$ electrons are strongly localized and protected from the environment by the $5d$ electrons. Consequently a magnetic coupling to ferromagnets, if present, is expected to be much weaker. However, Ln can have a large, unquenched orbital moment, whose value is therefore close to the one of a free Ln ion, in which the electrons occupy the orbitals according to Hund's rules. In table 5.1, the spin, orbital and angular momentum are given for the three molecules $TbPc_2$, $DyPc_2$ and $ErPc_2$, which have been studied as part of this work. It also provides with information about the easy

Molecule	S	L	J	easy axis/ easy plane
$TbPc_2$	3	3	6	perpendicular to Pc plane
$DyPc_2$	5/2	5	15/2	perpendicular to Pc plane
$ErPc_2$	3/2	6	15/2	parallel to Pc plane

Table 5.1.: Comparison of S, L, J and the easy magnetization axis of the three investigated $LnPc_2$ molecules.

magnetization axis of the molecules, which is crucial with regards to the magnetic coupling mechanism, described in this chapter. $TbPc_2$ exhibits the largest magnetic anisotropy, perpendicular to the Pc rings [39]. $DyPc_2$ has a clearly weaker, but still perpendicular anisotropy, while Er has the easy axis parallel to the Pc rings. The systematic investigation of these three different molecules can provide the fundamental information about the properties and interaction of the $LnPc_2$-based spin-hybrid system (see chapter 5.5).

The unique properties of SMMs have attracted the attention of scientists for more than two decades. They are considered to be predestined for very small molecular spintronic devices because of their magnetic hysteresis without the need of long range ordering combined with a high anisotropy and large magnetic moments [10, 15, 17, 53, 148]. Even for quantum computing SMMs are considered as a result of their coherence properties [149–151]. Most SMMs consist of several magnetic ions, e.g. Mn_{12} complexes [37, 38, 152, 153] or Fe_4 complexes [148, 154–156], while in bis(phthalocyaninato) Lanthanide complexes ($LnPc_2$) there is only one single Ln ion (Dy^{3+}, Tb^{3+}, Er^{3+}) centered in the molecule coordinated by two organic phthalocyanine ligands consisting of nitrogen, carbon and hydrogen atoms (figure 5.1). The remanent magnetization arises from the single ion anisotropy [39, 53, 157]. However, despite these promising properties, the use of SMMs for spintronic devices remains an extremely demanding challenge. In the first place there is the general challenge for all SMMs to conserve their SMM behavior at high enough temperatures to make them valuable for potential applications. Magnetic remanence for finite times has been observed at a temperature of only a few K. The spin relaxation of $TbPc_2$ molecules above 4 K is already too fast to detect a remanent magnetization by x-ray absorption spectroscopy (XAS), a rather slow experimental method [42]. Magnetization curves of $TbPc_2$ molecules show typically butterfly shape hysteresis even at very low temperatures, originating from the spin quantum tunneling at zero magnetic fields [41, 158, 159]. At temperatures below 4 K the relaxation is slow enough to identify these quantum tunneling effects with ac susceptibility measurements [40]. A second challenge is the contact and interaction with the environment. When SMMs are considered to serve as single molecule storage, single molecule switch or similar devices, it soon becomes clear that for these purposes, the molecule cannot be isolated, but must be in contact

with the device. However, it is not obvious that the SMM properties are preserved when the molecule is in contact with a surface. It was shown that the open hysteresis vanishes for $TbPc_2$, when it is in contact with non-magnetic metallic surface [41, 42]. Controlling the magnetic interactions at the molecular level and at interfaces is a challenge involving fine tailoring of materials/surfaces and the use of dedicated experimental and theoretical tools. Understanding the exchange mechanism between magnetic centers and a substrate is also fundamental in order to control processes at organic-inorganic magnetic interfaces [13]. Contact magnetic interaction occurs when electrons share the same orbitals, as a consequence of the Pauli exclusion principle. As described by the Heisenberg-Dirac-van Vleck (HDvV) model, the exchange interaction between two magnetic centers is isotropic and involves only the spin of the electron wave function. Yet, when the orbital moments of the magnetic centers are not quenched, anisotropic exchange may as well occur [160, 161].

In the work described in this chapter, these issued have been tackled. The first goal is to demonstrate that it is possible to preserve the magnetic remanence even for a $LnPc_2$ molecule deposited on a surface. A second goal is to use the surface to manipulate the SMM's properties in order to benefit from them. A third goal is a systematic study of the interaction mechanism that will help future studies to engineer spin-hybrid systems with the desired characteristics.

5.2. Synthesis and characterization of the $LnPc_2$ molecules

The $LnPc_2$ (Ln = Tb, Dy, Er) molecules have been synthesized by Dr. Svetlana Klyatskaya in the group of Prof. Dr. Mario Ruben at the Karlsruhe Institute of Technology (KIT). A brief description of the synthesis is given in the following according to reference [162]. The reagents used for the synthesis have been purchased by Sigma-Aldrich and Acros Organics and have not been further purified. At first the systhesys starts with the reaction of the phthalonitrile precursor *o*-dicyanobenzene and the lanthanide acetylacetonate $Ln(acac)_3{\cdot}nH_2O$, in the presence of a strong base and high-boiling solvents. A mixture of 1,2-dicyanobenzene, $Ln(acac)_3{\cdot}4H_2O$ and 1,8-diazabicyclo[5,4,0]undec-7-ene in 1-pentanol was refluxed for 36 h. The solution cooled down to room-temperature and was heated up to 100 °C for 0.5 h after adding acetic acid to the mixture. The precipitate was collected by filtration and washed with *n*-hexane and diethyl ether. After redissolving the purple product in $CHCl_3$/MeOH, the undissolved H_2Pc was filtered off. Purification was carried out by column chromatography on basic alumina oxide with chlorophorm-methanol mixture as eluent. By means of additional radial chromatography on silica gel followed by recrystallization from chloroform-hexane mixture, analytically pure

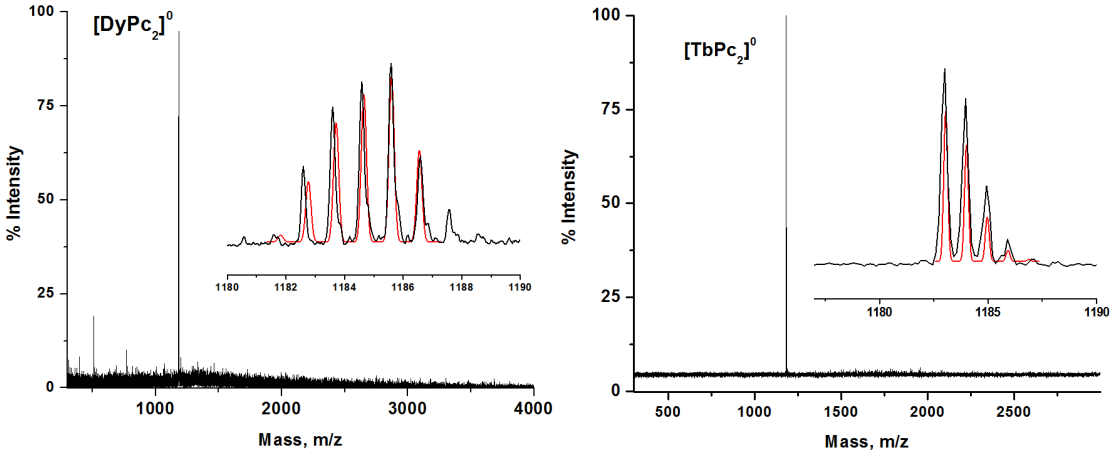

Figure 5.2.: MALDI - TOF - MS of $TbPc_2$ and $DyPc_2$ complexes. The insets show the expanded view of the peak to determine the isotope contributions [36].

powder samples were achieved.

The characterization of the molecules after the synthesis has been carried out in Prof. Rubens group as well and can be found in reference [36]. Matrix-assisted laser desorption/ionization - time of flight - mass spectrometry (MALDI-TOF-MS) has been used to determine the composition of the product. This is a powerful method for the analysis of materials such as MPc and $LnPc_2$. The instrument was calibrated with known standard (2,5-dihydrobenzoic acid, DHB) to obtain a 5 ppm mass accuracy of the mass spectra. The mass spectra were acquired in positive ion mode using resolution mode configuration. Figure 5.2 shows the detected intensity per mass for $DyPc_2$ and $TbPc_2$ with sharp maxima at the expected values $m/z = 1187$ and $m/z = 1183$, respectively. Each inset of the figures shows an expanded view in the mass region of the peak. One can clearly identify correspondent isotopic envelopes, which and are in good agreement with literature [163, 164].

A second method to determine the purity of the powder is ultraviolet - visible - near infrared spectroscopy (UV-Vis-NIR). Figure 5.3 shows the spectra from $DyPc_2$ and $TbPc_2$, which appear in the neutral form $[LnPc_2]^0$ according to reference [165]. The highest intensity is at a wavelength of 672 nm, while two main bands are observed at higher energies, 906 nm and 1300-1800 nm. The high-energy band is related to the radical part and attributed to the $e_g(\pi) \rightarrow a_{1u}(\pi)$ transition, while the lower energy band is assigned to an intramolecular charge transfer. These signals are fingerprints for the neutral $LnPc_2$ and confirm therefore the high purity of the neutral compound [166–169].

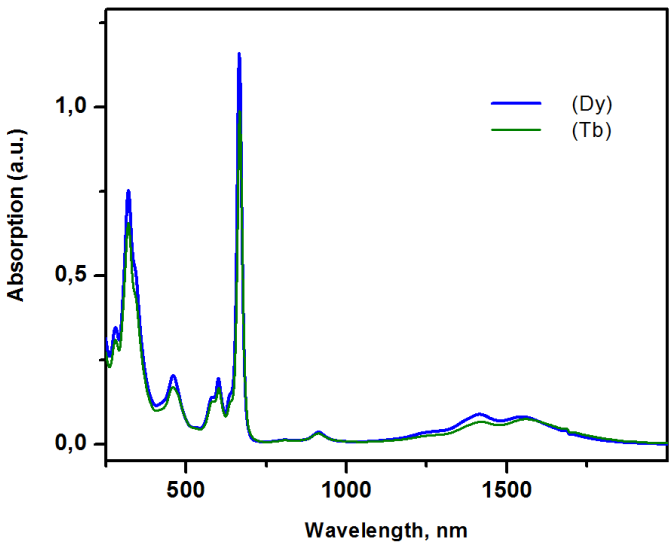

Figure 5.3.: UV-VIS-NIR spectra of $TbPc_2$ and $DyPc_2$ in CH_2Cl_2 [36].

5.3. Magnetic memory of a single ion magnet

As already mentioned in the introduction of this chapter, one challenge concerning the realization of SMM-based spintronic application is the direct contact between the molecules and certain surfaces. The hybridization with metallic surfaces, even noble metals like Au, leads the hysteresis opening disappear [41, 42], whereas in powder samples the opening has been observed [40, 170] (see also figure 5.4). The results in this section show that the magnetic remanence of $TbPc_2$ and $DyPc_2$ molecules can be preserved on an inert surface for very low temperatures. The section is based on reference [36] [D. Klar, *et al.*, Dalton Transactions **43**, 10686 (2014)].

As a reference measurement to the magnetization behavior of the $TbPc_2$ molecules in a submonolayer, figure 5.4 shows the magnetic field-dependent magnetization $M(B)$ of a $TbPc_2$ single crystal. This hysteresis loop was recorded by Dr. Andrea Candini at the Centro S3, Instituto Nanoscienze - CNR in Modena by means of a home-made Hall probe magnetometer [171]. The easy magnetic axes of the molecules are aligned with the external magnetic field. At a temperature of $T = 2$ K the $M(B)$ curve was recorded from -2 T to 2 T, where the magnetization is close to saturation. The hysteresis is clearly open and shows neither narrowing at zero magnetic field as expected for thin layers [41, 159], nor steps as consequence of spin quantum tunneling, which have been detected for very fast measurements at sub-kelvin temperatures [40].

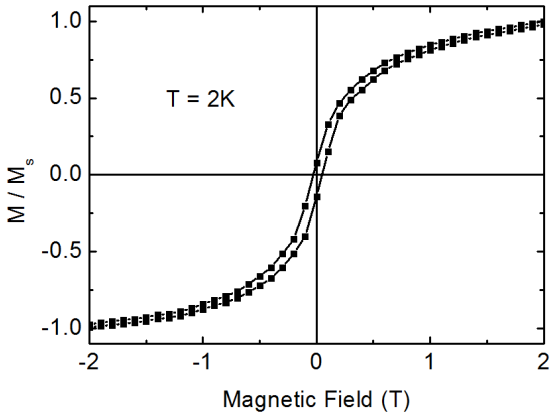

Figure 5.4.: Magnetization (M(B)) measurement on a single crystal of $TbPc_2$. The hysteresis loop was recorded in a home-made Hall probe magnetometer [36].

The electronic and magnetic characteristics of the $LnPc_2$ vary strongly between in-plane and out-of-plane direction. To use the molecules' properties for spintronic application, e.g. as storage media or switch, a well-defined orientation of the molecule on the surface is of high priority. The determination of the orientation is described in the following based on figure 5.5. This figure shows a sketch of one molecule on the HOPG surface and the incident photon beam. θ is defined as the angle between the surface normal and the $\boldsymbol{k}$ vector of the incident photon. Hence, for perpendicular irradiation $\theta = 0°$, whereas for grazing irradiation, like in figure 5.5, $0° < \theta < 90°$. The possibility to detect XAS for both, linearly horizontal and linearly vertical polarized light, enables a simple method to to determine how the molecules are oriented on the surface (chapter 4.2.1). A vanishing XLD at $\theta = 0°$ combined with a distinct XLD under grazing incidence, clearly indicate an adsorption with the Pc plane parallel to the surface.

In the following, results from the XAS and XMCD measurements on submonolayers of $TbPc_2$ and $DyPc_2$ on highly ordered pyrolytic graphite (HOPG) are described. The HOPG single crystal was cleaned by removing a few top layers with standard adhesive tape. A clean, smooth , glossy surface appears. The HOPG was immediately introduced afterward to the UHV chamber. During the subsequent 24 h bake out of the UHV system, physisorbed contaminations, e.g. H_2O, have been thermally desorbed from the HOPG surface. A submonolayer (0.5 ± 0.2 ML) coverage of $LnPc_2$ was prepared *in situ* by thermal evaporation of the molecules onto the HOPG crystal held at room temperature. The low amount of molecules guarantees that nearly all molecules are isolated on the surface and not interacting with each other. The amount of molecules was precisely controlled with a microbalance on top of the molecule evaporator during the evaporation process. Previously the sublimation rate ($\approx= 0.1$ ML/min) was calibrated with a second microbalance placed at the sample

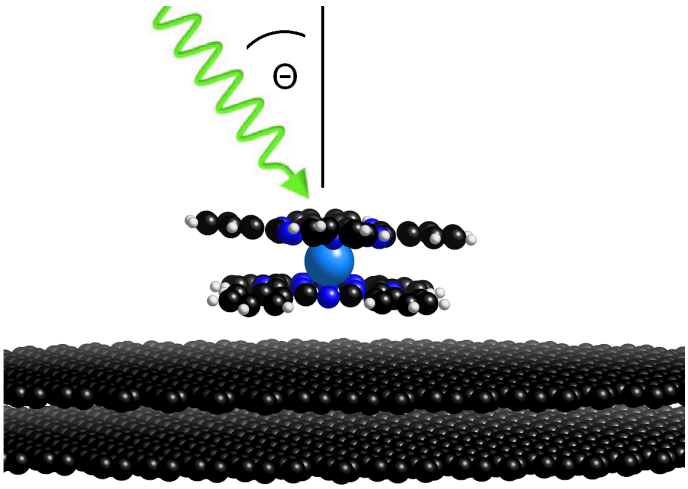

Figure 5.5.: Sketch of the x-ray absorption of one $LnPc_2$ molecule on HOPG. θ is defined as the angle between the surface normal and the $\boldsymbol{k}$ vector of the incident photon [36].

position. Eventually, the prepared sample was transferred to the superconducting magnet. The measurements relative to the $TbPc_2$ molecule were performed at the DEIMOS [172] beamline at synchrotron SOLEIL, while $DyPc_2$ molecules were studied at the SIM beamline at SLS synchrotron, Paul Scherrer Institut in Villigen, Switzerland, with the unique possibility to perform XMCD experiments at sub-Kelvin temperatures [74]. The temperature of 0.5 K is crucial for the detection of the open hysteresis curve of $DyPc_2$ because of its very low blocking temperature [40].

In figure 5.6 the absorption spectra for μ_H (black line), μ_V (red line) and the XLD (green line) are presented for normal x-ray incidence [(a) Dy, (c) Tb] and grazing x-ray incidence [(b) Dy, (d) Tb]. The absorption spectra at both edges show the identical characteristics with regards to the linear dichroism. For normal x-ray incidence both polarizations lead to identical absorption spectra, which means that there is no in-plane anisotropy regarding 90° rotation. The Tb edge is rather noisy due to some unknown problems during the recording of these spectra, and therefore they do not match perfectly. However, the differences are exclusively consequences of noise and not of anisotropic origin, which is obvious, because the lineshape of both spectra is practically the same. However, there is a clear anisotropy at grazing incidence (45° for Dy, 60° for Tb[1]), meaning that the electronic distribution in-plane is different to the out-of-plane one. Combining these two results, it is clear that all molecules are oriented with the Pc plane parallel to the graphite surface. This result has been observed for very thin layers of $LnPc_2$ molecules on various

[1]The reason, to chose different grazing angles is the different sample holder construction. At the SLS the sample edge was covered with a mask and therefore it was not possible to reach angles larger than 45° without irradiation on part of this mask.

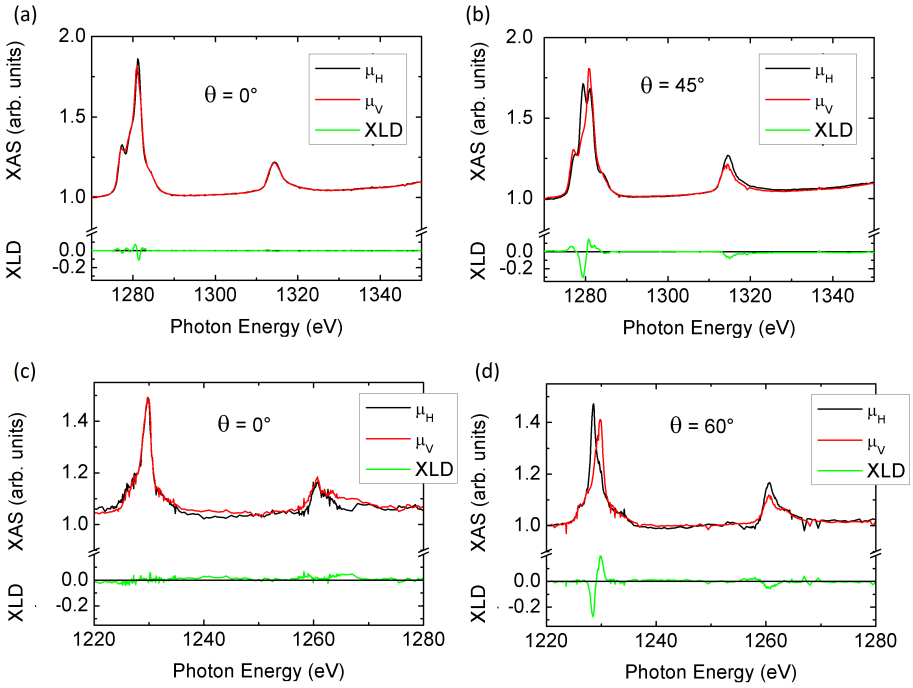

Figure 5.6.: Absorption spectra at the $M_{4,5}$ edges of Tb and Dy for μ_H (black line), μ_V (red line) and the XLD (green line) under normal x-ray incidence [(a) Dy, (c) Tb] and grazing x-ray incidence [(b) Dy, (d) Tb] [36].

surfaces [25, 41, 42, 159, 173, 174], but not on Lanthanum strontium manganite (LSMO), where the molecules are oriented perpendicular to the surface (standing up configuration) [174].

A proper confirmation of the molecules' alignment is given by the XLD spectra at the N K edge, similar to what is discussed in chapter 4 for FePc and CoOEP molecules. The $LnPc_2$ molecules are not planar, like the previously discussed ones, and they have sixteen N atoms per molecule instead of eight or four, respectively. Therefore, it is expected to reveal slightly different fine structures at the N K edge, but still the π^* and σ^* contributions are assignable with the identical argumentation as before. The lineshape of the spectra in figure 5.7 is very similar to the shape of FePc. Small differences occur due to the inner eight N atoms which are bound to the Ln ion. The electronic contribution is different not only because the N atoms are bound to a Ln ion instead of $3d$ transition metal, but also due to the different binding angle in the non-planar geometry of the $LnPc_2$ molecule.

Figure 5.8 shows the angle-dependent circular polarized spectra at the Tb and the Dy $M_{4,5}$ edges for different x-ray incidence angles, normal (0°) and grazing (60° or 45°) at T = 2 K or 0.5 K and external magnetic field B = 6 T or 1 T. The

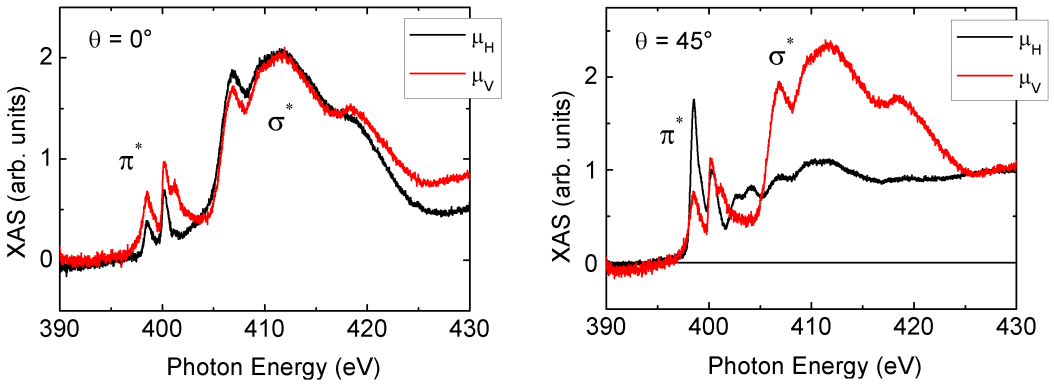

Figure 5.7.: Absorption spectra at the N K edge for μ_H (black line) and μ_V (red line) under normal and grazing (45°) x-ray incidence. π^* and σ^* contributions ca be clearly assigned to the peaks [36].

black line represents the circular right polarization μ^+, the red line the circular left polarization μ^- and the green line the difference of the two spectra, the XMCD signal. The XMCD intensity reveals information about the anisotropy. For a precise comparison, the spectra have to be normalized by their integral, because the finestructures of the XAS depend strongly on the incidence angle. A normalization to a certain value of the XAS is therefore not meaningful concerning the comparison of different angles. Hence, the shown spectra are normalized in such procedure that the integral over the M_5 edge of the non-dichroic spectrum, the so-called whiteline $(\mu^+ + \mu^-)/2 = 1$. Since the shape of the XMCD is obviously not angle-dependent, this normalization allows the direct comparison of the absolute values of the XMCD. For Tb the quotient $\frac{XMCD(60°)}{XMCD(0°)} = 0.497$, corresponding to $\cos(60.2°)$. This is a perfect match to the incidence angle of the measurement and the 0.2° are clearly below the error bar. The reason for this scaling of the XMCD intensity with the cosine of the incidence angle is the large uniaxial anisotropy of $TbPc_2$. Though the shape of the XAS is angle-dependent, the XMCD shape remains unchanged. The magnetic moment is not rotated by the magnetic field, even though the field has a large in-plane component. The behavior of the magnetic moment is Ising-like, either up or down, but without an in-plane component. The XMCD measurement however, can only detect the magnetization in the incidence direction, which is the projection of the perpendicular moment onto the grazing incidence photon beam. From simple trigonometry one can deduce that the XMCD scales with the $\cos(\theta)$. This angle dependence was shown for $TbPc_2$ molecules on other substrates as well [26, 36, 41, 42]. A similar dependence is visible for the Dy XMCD, for which the normalization was performed identical. In this case the quotient $\frac{XMCD(45°)}{XMCD(0°)} = 0.680$ and corresponds to $\cos(47.2°)$. The angle of 47.2° is also close to the incidence angle of 45° and the origin is the same as discussed for Tb. A potential error source aside noise, measurement artifacts and the accuracy

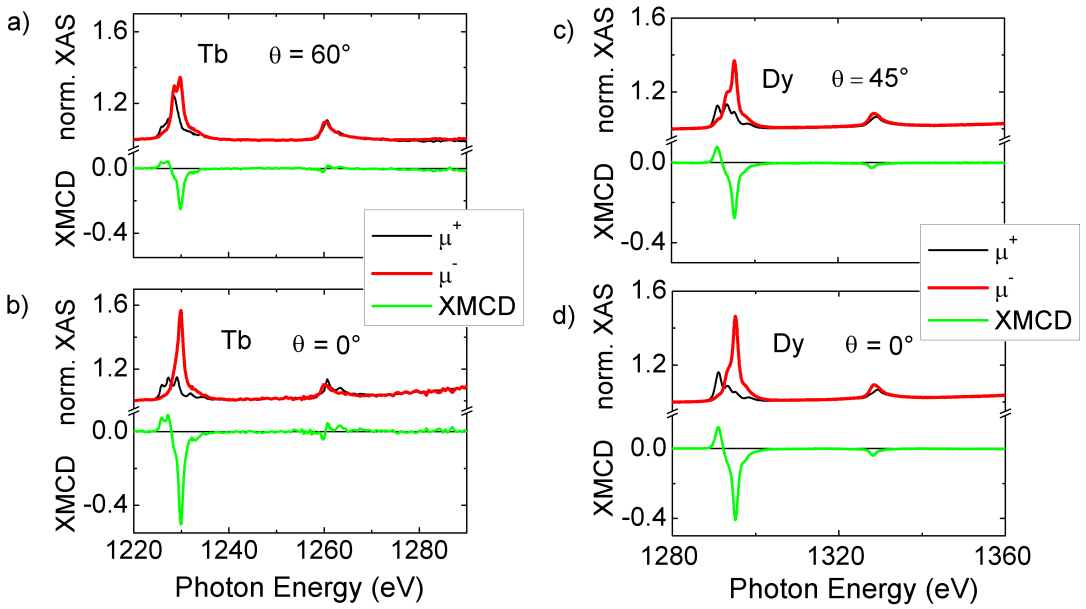

Figure 5.8.: (a) and (b): Normalized XA spectra at the Tb $M_{4,5}$ edges for left (red) and right (black) circularly polarized x-rays and the dichroic spectra (green) for the angles of 60° and 0° recorded in a magnetic field of 6 T and at a temperature of 2 K. (c) and (d): Normalized XA spectra at the Dy $M_{4,5}$ edges for left (red) and right (black) circularly polarized x-rays and the dichroic spectra (green) for the angles of 45° and 0° recorded in a magnetic field of 1 T and at a temperature of 0.5 K [36].

of the data evaluation, which can be responsible for the deviation of 2.2°, is the accuracy of the adjusted angle. The anisotropy of $DyPc_2$ is clearly weaker than the one of $TbPc_2$, but in a field of 1 T the magnetic moments are not forced into the plane[2].

The field dependence of the Tb magnetization is given in Fig. 5.9 (a). The curves show the maximum of the M_5 edge (1229.8 eV) normalized to the pre edge (1220 eV) at a temperature of $T = 2$ K. The hysteresis measurement program at the DEIMOS beamline records only these two points and enables a very quick measurement of the magnetization cycle. Four loops in total are recorded , for both polarizations from negative magnetic field to positive magnetic field and *vice versa*. The loops for the different polarizations have been averaged and normalized to exclude polarization-dependent artifacts. The opening of the hysteresis is clearly visible between the approximate saturation values $B = -1$ T and $B = 1$ T. Though the butterfly shape as consequence of spin quantum

[2]During this specific beamtime, magnetic field above 1 T were not possible due to problems with the superconducting magnet

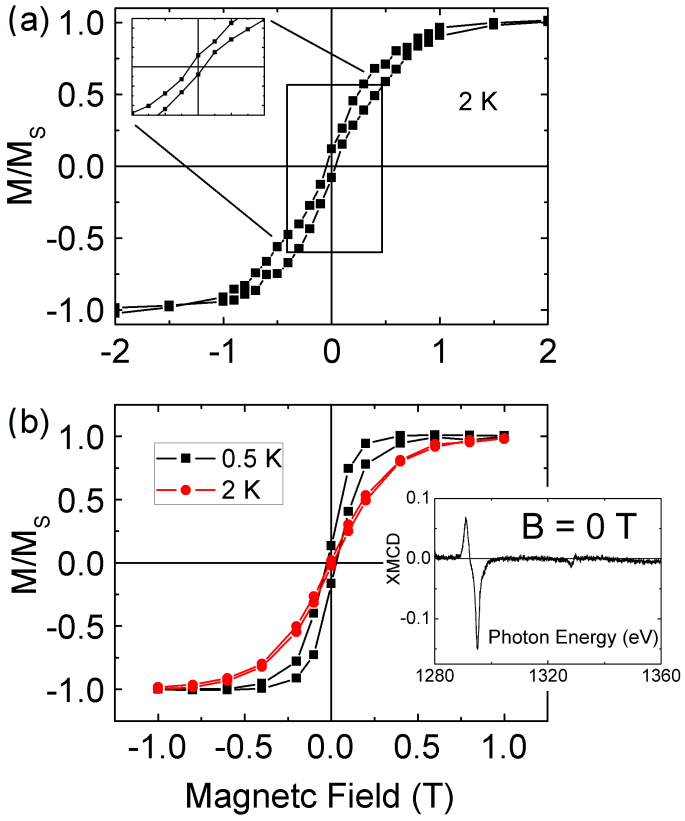

Figure 5.9.: Field-dependent magnetization measured at the maximum of (a) the Tb M_5 edge XMCD at T = 2 K and (b) the Dy M_5 XMCD edge at T = 0.5 K (black) and T = 2 K (red), normalized to the saturation magnetization [36].

tunneling is apparently present, the inset showing an enlargement around zero magnetic field reveals that remanent magnetization exists at $B = 0$ T and the magnetization curves do not cross at zero field as shown on other substrates [41, 159].

The measurement procedure for the field dependence of the magnetization of $DyPc_2$ was different from the one described for $TbPc_2$. Each data point in figure 5.9 (b) corresponds to a complete measured XMCD pair, one μ^+ and one μ^- spectrum. The XMCD signal was calculated and normalized according the earlier described analysis and all 26 data points were plotted as field-dependent magnetization. This way of measuring the field dependence takes much longer and delivers less data points. However, the curves reveal a clear magnetic remanence as well. A butterfly shape is not visible, which can be related to the lower resolution because of less data points. In any case the relaxation is very slow and therefore remanent magnetization can be detected with this rather slow measurement method. Since for each magnetic field point the XMCD was determined, the XMCD

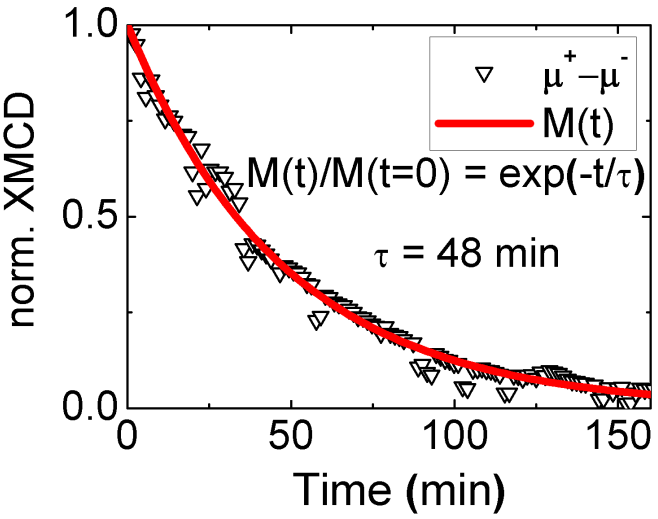

Figure 5.10.: Time dependence of the normalized XMCD intensity at the maximum of the Dy M_5 edge without external magnetic field at a temperature of 0.5 K. The red curve is an exponential function with a half life of 48 minutes [36].

without applied field is shown as inset in figure 5.9 (b). The XMCD is small, but doubtless recognizable and the shape still matches the XMCD in figure 5.8 (d). At $T = 2$ K the remanent hysteresis vanishes, confirming the strong temperature sensitivity of the spin relaxation time and the lower blocking temperature of $DyPc_2$ compare to $TbPc_2$, for which at $T = 2$ K the hysteresis is still open (see figure 5.9(a)).

To make a quantitative statement about the relaxation time of the $DyPc_2$ magnetization, the XMCD intensity was recorded by time-dependent measurements after switching off the magnetic field. With alternating polarizations the intensity at the XMCD maximum of 1295.1 eV was detected. The difference of two subsequent measurement points is plotted versus the time axis in figure 5.10. The time interval between two consecutive data points was approximately 90 seconds. In this graph the relaxation is easily perceptible, following an exponential decay, which is fitted with the simple function

$$\frac{M(t)}{M(t=0)} = \exp\left(\frac{-t}{\tau}\right), \tag{5.1}$$

where $\tau = 48$ min is the half life of the XMCD intensity. 48 min is easily in the region of a typical XMCD measurement and even some hours after switching off the magnetic field, a detectable XMCD signal is still present. This confirms the result which was already observed by the field dependence. The spin relaxation time in $DyPc_2$ molecules on HOPG at $T = 0.5$ K is slow enough to be detected by XMCD.

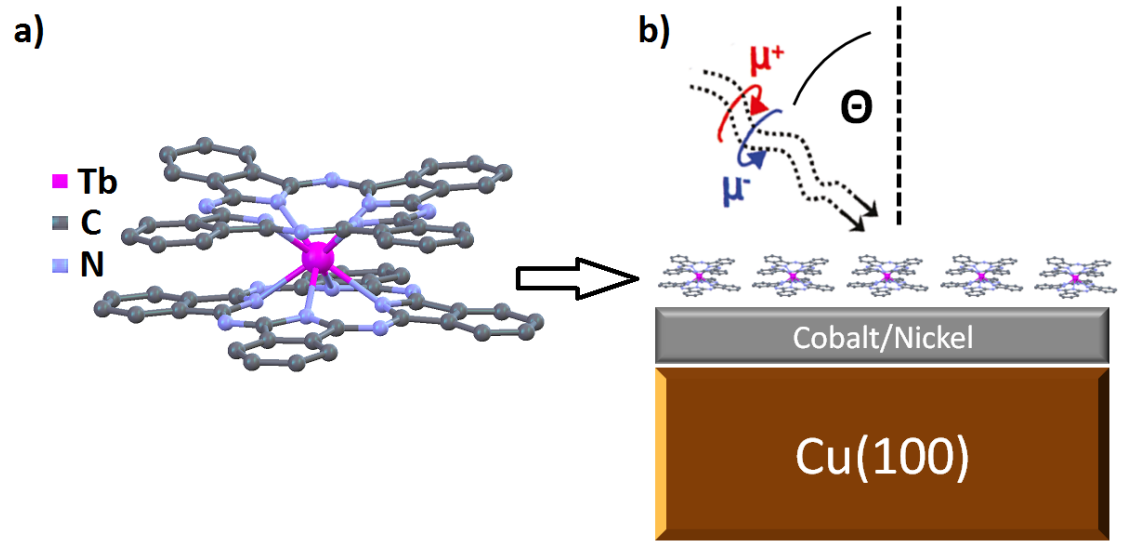

Figure 5.11.: The $TbPc_2$ molecule (a), consisting of two parallel phthalocyanine planes with the Tb ion centered in between, and (b) a schematic illustration of the studied sample [26].

5.4. Remanent magnetization of $TbPc_2$ by coupling to ferromagnetic films

The section is based on reference [26] [D. Klar *et al.*, Beilstein J. Nanotechnol. **4**, 320 (2013).]. As seen in the previous chapter 4, the planar transition metal complexes CoOEP and FePc couple magnetically to ferromagnetic surfaces. The situation for $LnPc_2$ molecules however is different. The double-decker structure causes a clearly larger distance between the magnetic Ln ion and the surface. A direct exchange between the Ln and the ferromagnetic surface can therefore be excluded. However, in chapter 4 it was also demonstrated that not only direct coupling is possible, but also coupling via the N atoms of the ligand, or graphene and oxygen interlayers. Another crucial point is the difference between the electronic structure of $3d$ transition metals, like Fe, and $4f$ lanthanides, like Tb. The $4f$ electrons are shielded from their environment and are strongly localized in contrast to the delocalized $3d$ electrons of Fe. A coupling mechanism analog to the one in the previous chapter is therefore not self-evident. However, a magnetic coupling was found experimentally and is presented in the following.

The samples, sketched in figure 5.11 (b) were prepared *in situ* at a base pressure of 10^{-10} mbar directly before the measurements. By cycles of Ar^+ bombardment and annealing, the Cu(100) surface was cleaned and subsequent the ferromagnetic films

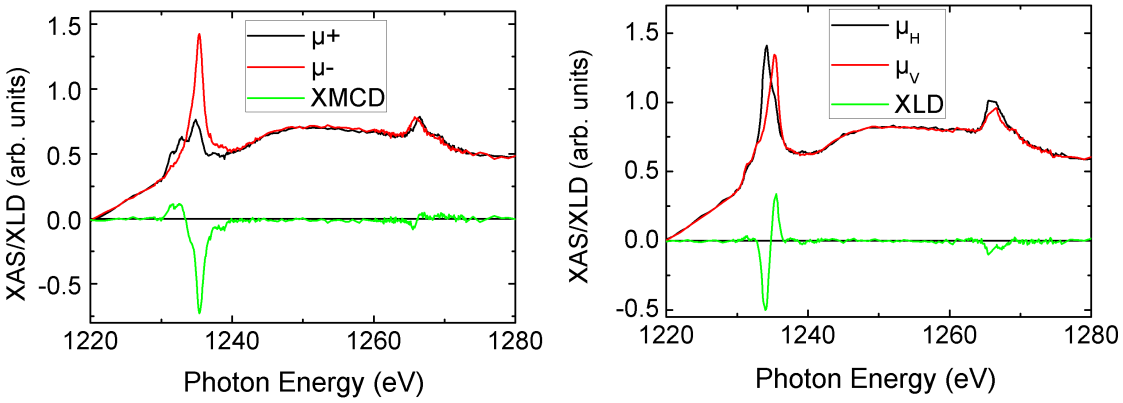

Figure 5.12.: X-ray absorption spectra of the Tb $M_{4,5}$ edges for a submonolayer $TbPc_2$/Cu(100), measured at $T \geq 10$ K and $B = 6$ T. The left figure shows the spectra for circularly polarized x-rays (black and red) and the XMCD (green) at perpendicular photon incidence (0°). The right figure shows the linearly polarized absorption spectra for an incidence angle of 45°. The red line corresponds to vertical polarization, the black line corresponds to horizontal polarization and the green line represents the XLD [26].

were grown epitaxially via electron beam evaporation. The 10 ML thick Co film was produced with a rate of 0.5 ML/min and the 15 ML thick Ni film with a rate of 0.3 ML/min. By means of AES and LEED the surface quality was controlled to guarantee an epitaxial ferromagnetic film without impurities. $TbPc_2$ molecules were thermally evaporated at a temperature of about 400°C from a Knudsen cell onto the substrate held at room temperature.

The XAS measurements of the system $TbPc_2$/Co/Cu(100) were performed in a magnetic field up to 6 T at the DEIMOS beamline at the synchrotron SOLEIL, the XAS measurements of the system $TbPc_2$/Ni/Cu(100) in a magnetic field up to 4 T at the ID08 beamline at the ESRF. The lowest possible temperature was reached by cooling in a liquid Helium bath cryostat[3] (T = 4.2 K), while the real temperature at the sample was limited by the quality of the thermal contact, leading to temperatures above 4.2 K. In detail we were able to measure at T ≈ 8 K at the ESRF and T ≥ 10 K at SOLEIL, although the temperature at the sample holder was at 4.2 K.

Figure 5.12 shows the XLD and XMCD of $TbPc_2$ molecule on Cu(100) at a magnetic field of $B = 6$ T and a temperature of $T \geq 10$K. Both the XMCD and the XLD confirm the expected results on a non-magnetic metallic surface [41, 42]. The spectra for left and right circularly polarized x-rays and the XMCD show the

[3]The evaporation cryostat at the DEIMOS beamline was installed after these measurements.

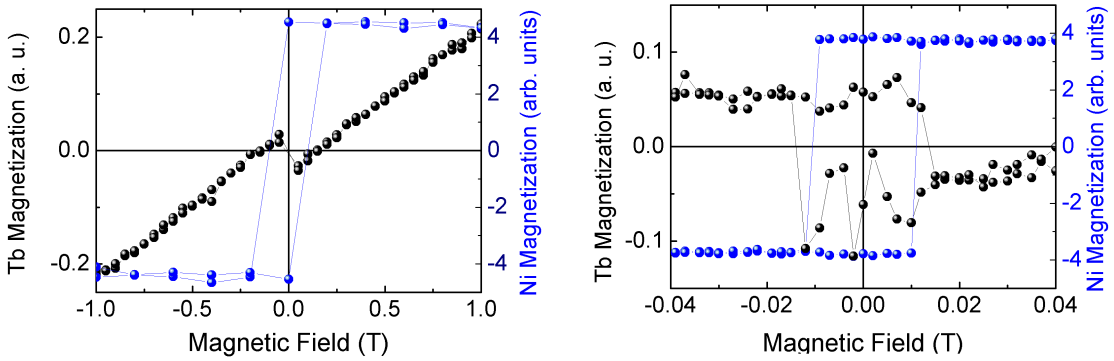

Figure 5.13.: Element-specific field-dependent magnetization for the sample $TbPc_2$/Ni/Cu(100). The blue line is the magnetization curve at the maximum XMCD intensity of the Ni L_3 edge (852.5 eV), the black line is at the Tb M_5 edge (1235.4 eV). The left figure shows the curves from -1 T to 1 T and the right figure presents a zoom between -0.04 T and 0.04 T. The measurements were performed at T = 8 K under normal x-ray incidence (0°) [26].

characteristic line-shape and amplitude for $TbPc_2$ at normal incidence. At grazing incidence the absorption of linearly vertically and horizontally polarized light show the same differences as already presented for $TbPc_2$ on HOPG in the previous section in figure 5.6 (d). Hence, the molecules orient on the Cu(100) surface in the same lying configuration as on HOPG.

To detect a magnetic coupling between a ferromagnetic substrate and $TbPc_2$ molecules, a 15 ML thin Ni film was epitaxially grown on Cu(100) via MBE. This Ni film has a well-defined easy magnetic axis perpendicular to the surface [175] and is therefore ideally suited for potential magnetic coupling to $TbPc_2$ molecules, whose easy magnetic axis is also perpendicular to the surface in the preferred lying configuration. The magnetic field dependence of the element-specific magnetization was recorded. In figure 5.13 (a) the magnetization of Ni (blue) and Tb (black) is shown for magnetic fields between -1 T and 1 T for a $\theta = 0°$ at $T = 8$ K.

The field dependence for Ni is characteristic for the easy axis of a ferromagnet. The coercive field is not representative because of the very low density of data points. However, the field-dependence of the $TbPc_2$ shows some features which are clearly not characteristic for the $TbPc_2$ molecule. The high field behavior seems completely regular, as expected for this molecule at a temperature as high as 8 K. The magnetization shows paramagnetic behavior and follows the field linearly. Around zero magnetic field the characteristics of the curve are different. The magnetization crosses the zero value three times: at $B = 0$, and just before and after $B = 0$. This implies that the magnetization is antiparallel to the external

magnetic field for the low magnetic field region. This field dependence must be a consequence of an antiferromagnetic coupling to the substrate. To shed more light on this coupling, the zero-field region was studied with a higher density of points, presented in figure 5.13 (b). In this illustration, the coupling between Ni and Tb is even more evident. At the coercive field of approximately $B = \pm 10$ mT the Ni magnetization switches its direction and simultaneously the Tb magnetization also switches, but in the opposite direction. The antiferromagnetic coupling is therefore perfectly proven. The high field behavior is also interesting and requires further interpretation. In contrast to what has been reported about the coupling of planar molecules, as shown in chapter 4, the magnetization of the molecules does not strictly follow the magnetic behavior of the substrate, but shows a clear field dependence. This field dependence is somehow similar to the one shown in chapter 4.2.2 for a trilayer system of CoOEP molecules. However, the origin here is completely different and not a consequence of different contributions from coupled and uncoupled molecules. The reason for the switching is a much weaker coupling strength. While the coupling energy for planar molecules is reported to be in the order of $B_{exchange} \approx 100$ T$>> B_{applied}$, here the coupling energy is in the same order of the external magnetic field and the Zeemann energy overcomes the coupling energy in the high field region. The magnetic moments of Tb align parallel to the magnetic field and the field dependence shows a paramagnetic characteristic. Since the identical system was investigated by [25], it is remarkable that we obtain a significant difference in the exchange field and the amplitude of the antiparallel signal at the Tb M_5 edge, probably a result of a weaker coupling. However, the main issue of the presented results is the demonstration of an antiferromagnetic coupling of $LnPc_2$ molecules to ferromagnetic substrates. A detailed presentation of the theoretical description is given is chapter 4.

To further investigate the nature of coupling, a second magnetic film was produced, i.e. 10 ML Co/Cu(100). The Co film grows epitaxial on the Cu, but in contrast to Ni the easy magnetic axis is in the plane [102]. As consequence of the large magnetic anisotropy of the $TbPc_2$ molecules, a different coupling mechanism in this spin-hybrid system is expected. The graph of figure 5.14 (a) shows the magnetic signal of Tb in an external field between -6 T and 6 T. The shape is dominated by a paramagnetic signal as expected for a free molecule at a temperature of $T \approx 10$ K. But close to zero field the superposition of a second contribution becomes visible. In order to highlight the contribution, the paramagnetic background was removed by subtracting a linear signal. The outcome is the graph of figure 5.14 (b). Compared to the Co magnetization curve (red line), one can see the antiparallel signal of the Tb magnetization. This antiferromagnetic contribution is very small compared to the dominating paramagnetic signal, because the Co magnetization direction is not the direction of the molecules' easy axis. If a very large coupling strength between the molecules and the Co substrate exceeds the magnetic anisotropy barrier, the magnetic moment of Tb could be forced in the plane. However, because of the large magnetic anisotropy barrier of the $TbPc_2$ molecules of 73 meV [25, 53], the

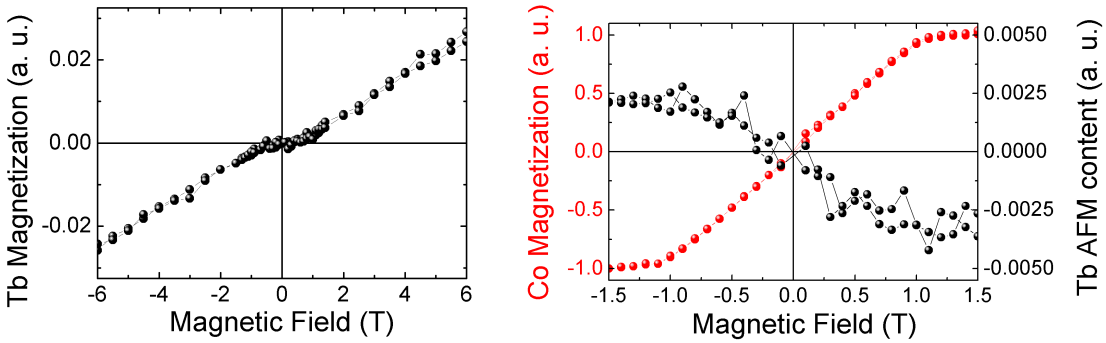

Figure 5.14.: Magnetization curves for the sample $TbPc_2$/Co/Cu(100). The left figure shows the magnetization curve at the maximum of the M_5 edge of Tb (1235.4 eV) from -6 T to 6 T. In the right figure one can see the magnetization curve at the maximum of the L_3 edge of the Co XMCD signal (778 eV) (red line) and the Tb M_5 curve after subtraction of a linear signal (black curve). The measurements were performed at perpendicular x-ray incidence at $T \geq 10$ K [26].

magnetic moment of the Tb ions is expected not to be forced to the in plane direction by the Co magnetization since the coupling energies presented in Ref. [25] are in the regime of 1 meV. The magnetic coupling between the Co substrate and the molecules is therefore only between the out-of-plane component of the Co magnetization and the Tb ion.

5.5. Case study of anisotropic exchange on a Ni(111) single crystal

The section is based on reference [65] [A. Candini, D. Klar *et al.*, submitted]. After demonstrating the magnetic coupling between $TbPc_2$ molecules and ferromagnetic substrates, in this chapter this coupling is discussed under more general aspects. The focus is on the origin of the coupling, the coupling mechanism and a qualitative and quantitative description of the interaction within this spin-hybryd system. Therefore, DFT calculations complement the XAS and XMCD investigations for a accurate understanding of the system. The DFT calculations were performed by Dr. Simone Marochhi and Dr. Valerio Bellini at the Centro S3, Instituto Nanoscienze - CNR in Modena.

For this purpose the selected substrate is a Ni(111) single crystal. The achievement of a clean and smooth surface of the crystal is easy, quick and reliable as already described in chapter 3. An important advantage of the Ni(111) single crystal

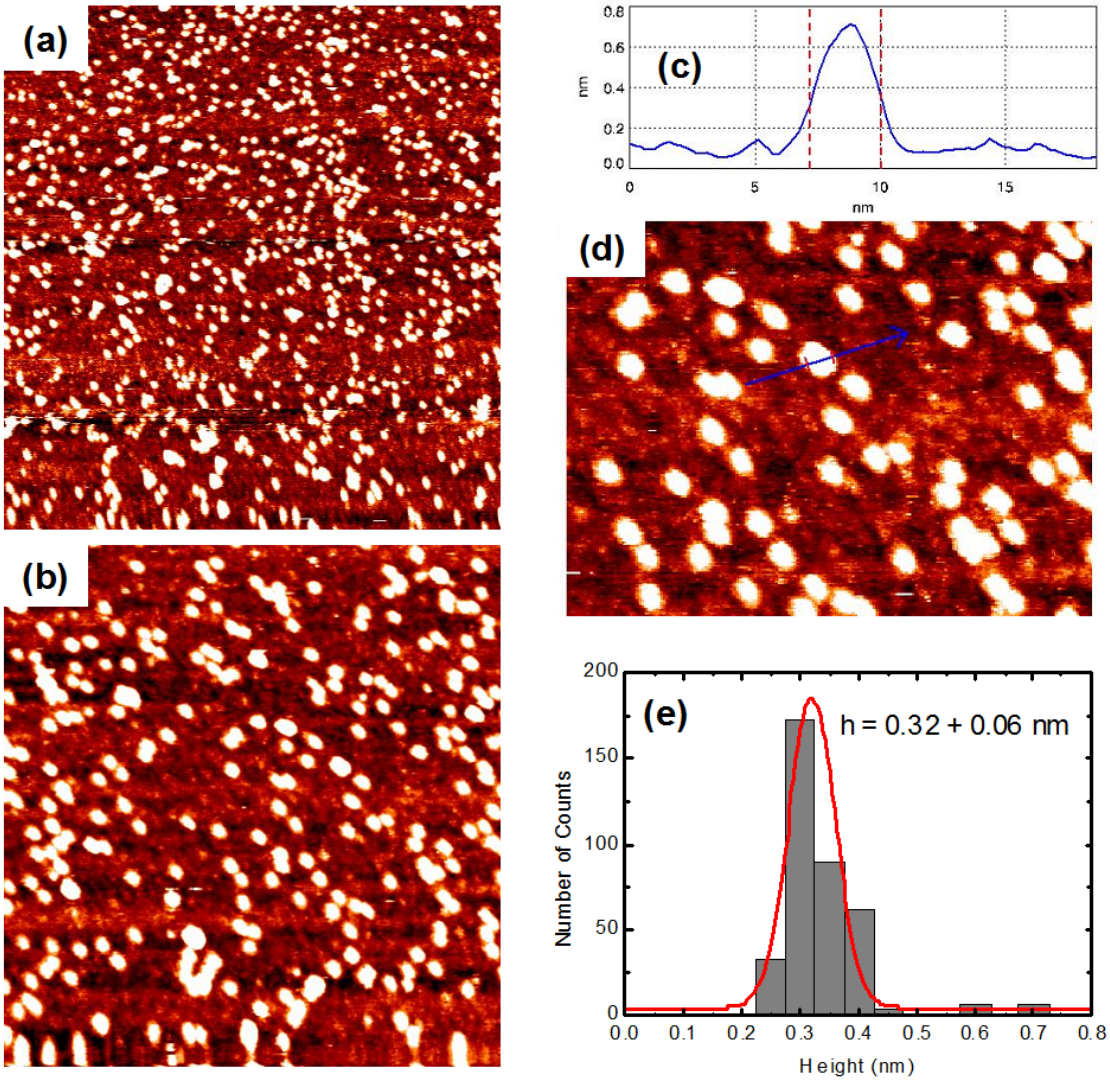

Figure 5.15.: (a) 200 × 200 nm^2, (b) 100 × 100 nm^2 STM images of the $TbPc_2$ molecules on Ni(111). (c) Typical height profile measured along the line in panel (d) 30 × 30 nm^2 STM. (e) Histogram plot of the height profiles of more than 300 molecules [65].

compared to the Ni and Co films on Cu(100) is the possibility to grow graphene, which has also been shown in chapter 3. In this chapter, it was presented that the graphene interlayer has a significant impact on the coupling between planar molecules and the ferromagnetic substrate. Hence, the influence on $LnPc_2$ molecules will be studied in the following section as direct comparison to the results on bare Ni(111) in this section. Moreover the use of a single crystal as the substrate, displaying non-saturating magnetization at finite fields, provides the direct proof that the coupling strength is proportional to the substrate magnetization. To make a general statement about the coupling nature of the molecule, different $LnPc_2$ molecules were studied, i.e. $TbPc_2$, $DyPc_2$ and $ErPc_2$. The main reason to select these three is the difference in their magnetic anisotropy. As already mentioned, $TbPc_2$ and $DyPc_2$ have out-of-plane anisotropies, $TbPc_2$ clearly stronger than $DyPc_2$. In contrast $ErPc_2$ shows in plane anisotropy. Differences in the magnetic coupling can help modeling and understanding the general interaction of $LnPc_2$ molecules with their environment.

Measurements were performed at the ID08 beamline of the ESRF. The samples were prepared *in situ* by evaporating ≈ 0.3 monolayers of $LnPc_2$ molecules on a freshly prepared Ni(111) surface. Before deposition of molecules, the surface was cleaned by repeated cycles of Ar^+ sputtering (Energy = 2 keV for 20 minutes and E = 0.8 keV for 10 minutes) and annealing (Temperature = 800°C for 5 minutes). The quality of the surface was checked by LEED. A molecular coverage of ≈ 0.3 monolayers of $LnPc_2$ molecules was produced on the Ni(111) surface via thermal evaporation after long degassing of the powders. The evaporation temperature of the molecules, whose sublimation rate was monitored with an *in situ* quartz microbalance to determine the thickness precisely, was constantly 420 °C at a base pressure of 1.0×10^{-9} mbar, while the Ni(111) single crystal was held at room temperature. After the deposition of the molecules on the substrate, STM images show isolated spots with reproducible lateral size of 2 - 3 nm and height of 0.3 - 0.4 nm (figure 5.15) compatible with the molecule sizes assuming that the Pc ring lies flat on the surface, as also demonstrated in the previous sections on HOPG and ferromagnetic films. From a statistical analysis applied to the STM images, it came out that about 20 - 40% of the surface is occupied by a 2D distribution of isolated clusters.

XMCD measurements at the $L_{2,3}$ absorption edges of Ni and the $M_{4,5}$ absorption edges of Ln were performed in TEY mode. An external magnetic field $\boldsymbol{B}$ can be applied parallel to the incident photon beam, at an angle θ with respect to the normal of the sample surface, as defined previously in figures 5.5, 5.11. In order to minimize the effects of field inhomogeneity, measurements have been carried out by switching both the helicity and the applied field to obtain the dichroic spectrum ($\mu^+ - \mu^-$). In contrast to the absorption spectra on graphite, a strong non-linear background is visible at Ln $M_{4,5}$ energies coming for the Ni substrate. The final XMCD values are obtained by normalizing the difference

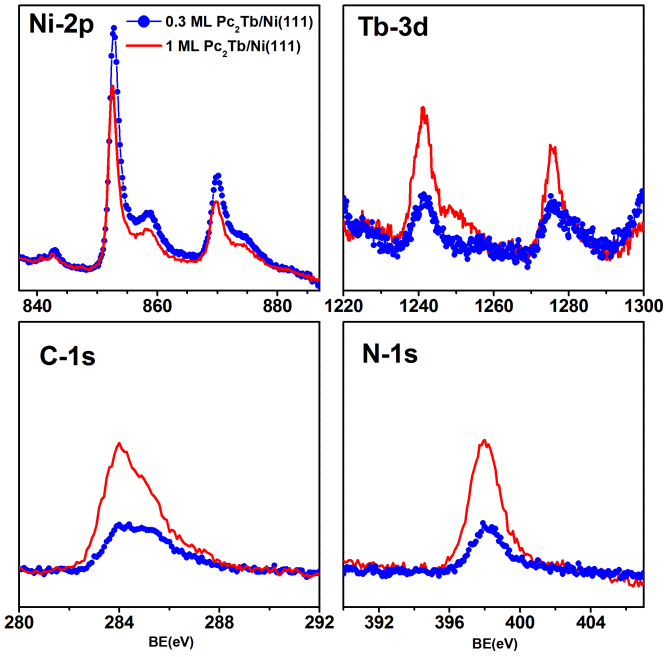

Figure 5.16.: XPS core levels for the $TbPc_2$ deposited by sublimation on the Ni(111) surface for two different coverages (0.3 ML and 1 ML) [65].

$\mu^+ - \mu^-$ by the height of the XAS $(\mu^+ + \mu^-)/2$ edge. To plot the magnetization curve as a function of the external magnetic field, the XMCD intensity was recorded at different field points. In the case of Ni and Tb, in order to make faster data acquisition for each field point only the intensities of the $L_3(M_5)$ edge (E) at 853(1243) eV and pre-edge (P) at 845(1232) eV were measured for the two polarizations for each element under investigation, since the XAS and XMCD line-shapes do not change with the field. The resulting magnetization value is defined as: $(E^+/P^+ - E^-/P^-) / \frac{1}{2} (E^+/P^+ + E^-/P^-)$. Due to technical issues concerning the stability of the monochromator, this procedure was not possible for Dy and Er, where complete XMCD spectra have been taken for each field point. After the analysis and normalization of the spectra for each magnetic field, the maximum absolute value of the XMCD M_5 edge is plotted in dependence of the magnetic field.

Besides STM and LEED, the sample quality was also controlled by means of XPS, i. e. the chemical composition of the $TbPc_2$ molecules deposited on the Ni(111) surface. In figure 5.16 the core levels of the $TbPc_2$ /Ni(111) interfaces for two different coverages of the $TbPc_2$ deposited by sublimation are shown. Core level intensities have been analyzed taking into account the atomic sensitivity and the attenuation of the electronic signals. The Tb-3d, N-1s and C-1s core level line shapes measured for all the depositions fit well with the corresponding data obtained on a thick film deposited from the liquid phase (not shown). The

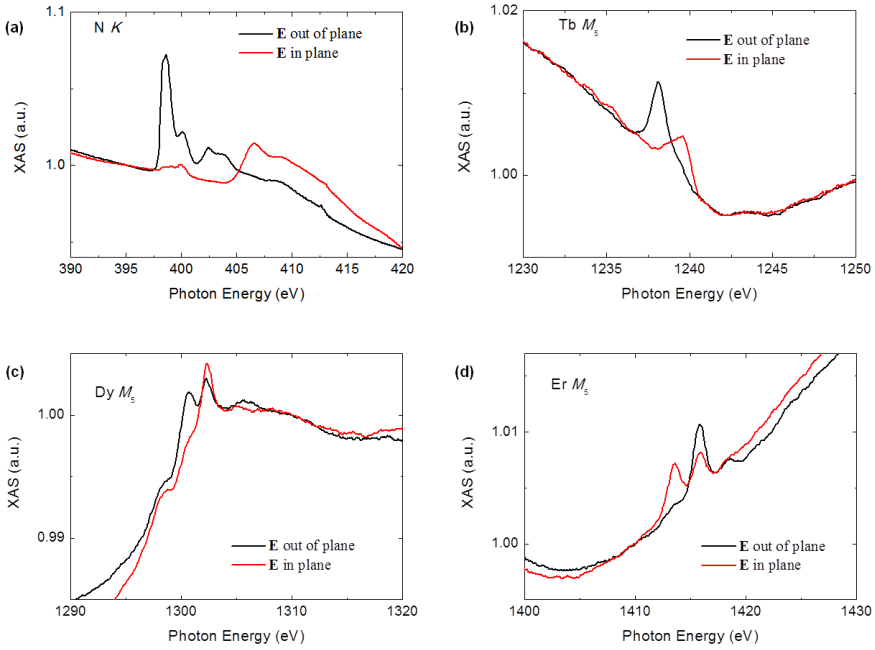

Figure 5.17.: X-ray linear dichroism for (a) N K edge and (b-d) Ln M_5 edges (Ln = Tb, Dy, Er) [65].

N-1s/Tb-3d = 18 ± 5 and C-1s/Tb-3d = 75 ± 20 ratios are well reproducible and close to the expected ones (16 and 64), clearly indicating that the overall molecular stoichiometry is preserved during the heating and deposition processes. From the Tb-3d/Ni-2p ratio and by taking into account the Ni signal attenuation due to the overlayer, the average area occupied by one $TbPc_2$ is obtained. Assuming that the complete coverage is made by molecules lying flat on the surface and considering an area of 2 nm^2 for each molecule, we derived a thickness of 0.3 - 0.5 ML for the $TbPc_2$ film, in quite agreement with the quantity read by the quartz microbalance (30%) and with the coverage derived by STM (20 - 40%).

Figure 5.17 shows XLD on the N K and Ln $M_{4,5}$ edges which are found in agreement with what was reported in previous works, where $TbPc_2$ [41, 42, 176], porphyrins [20, 21] or Pc molecules [27] were deposited on substrates. This indicates that the $LnPc_2$ molecules are isolated and flat on the substrate with the Pc plane parallel to the surface. The angle dependence of the N K edge in figure 5.17 (a) coincide with the one in section 5.3. However, the fine structures in figure 5.7 are more distinct due the weak hybridization with the substrate, whereas the strong interaction with the metallic Ni leads to delocalized states and broadened structures in the XAS.

Figure 5.18 shows the XAS and XMCD spectra of Ni and $LnPc_2$ taken at

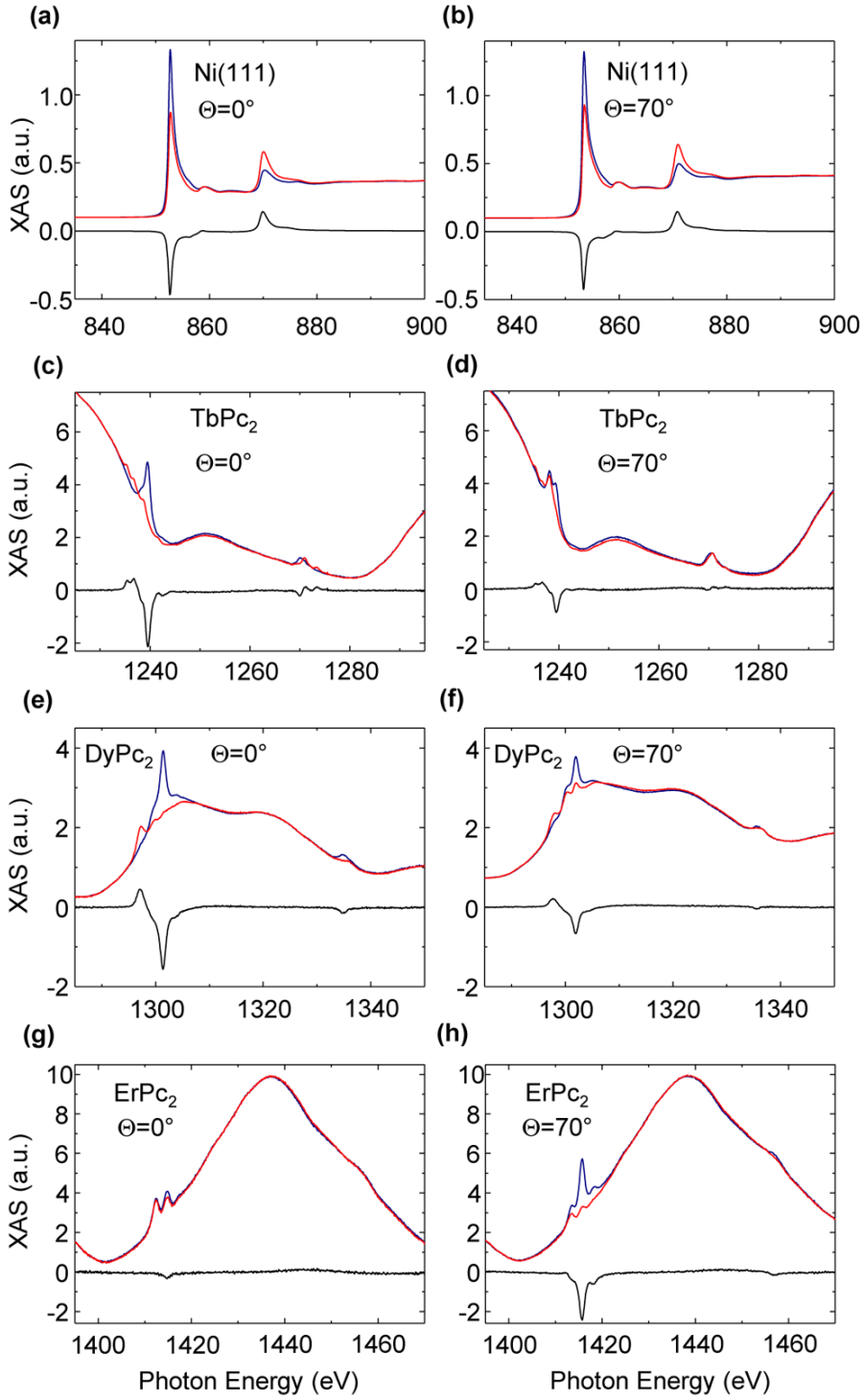

Figure 5.18.: XAS and XMCD spectra for Ni (a-b), Tb(c-d), Dy(e-f), Er(g-h) edges in $LnPc_2$/Ni(111) at $\theta = 0°$ (left panels) and $\theta = 70°$ (right panels) incidence angles, taken at an applied external field $B = 5$ T. XAS spectra have been normalized with respect to the average L_3 (M_5) intensity $(\mu+ + \mu-)/2$, which has been set to 1 [65].

normal and grazing incidence at a magnetic field $B = 5$ T for two photon incidence angles, $\theta = 0°$ (left column) and $\theta = 70°$ (right column). These spectra compare well with the ones already reported [25, 26, 36, 41, 42, 159, 173, 176, 177], demonstrating the relatively robust character of these molecules. The Ni XAS and also the XMCD are identical for both angles, (a) and (b), at the high field of $B = 5$ T, since the magnetization reaches saturation irrespective if the magnetic field is applied along the easy or hard magnetic axes. The six spectra below correspond to $TbPc_2$, (c) and (d), $DyPc_2$, (e) and (f), and $ErPc_2$, (g) and (h). In all spectra, a clear non-linear background is visible, which is characteristic for the Ni substrate. Though these EXAFS structures are energetically far away from the Ni absorption edges, the background is in the same order of magnitude of the Ln $M_{4,5}$ edges, because the amount of Ln ions is only a fraction of a monolayer and causes only a very small signal. Due to the low noise level of the beamline and the large XMCD of the Ln ions, the XMCD is easy to identify and shows clear fine structures. The angle dependence trends for $TbPc_2$ and $DyPc_2$ are identical to the ones of the molecules on HOPG in chapter 3 and previous publications on various surfaces [25, 26, 36, 41, 42, 159, 173, 176, 177]. The surface has apparently no impact on the molecules orientation on that surface or the magnetic anisotropy. A clear difference concerning the angle dependence is visible for $ErPc_2$ in figures 5.18 (g) and (h). The XMCD at the Er $M_{4,5}$ edges is large at grazing incidence and vanishingly small for $\theta = 0°$. In contrast to Tb and Dy, Er has the easy direction of magnetization parallel to molecular plane as observed in bulk Ln(III) bis-phathalocyanines [53].

Figure 5.19 shows the isothermal magnetization cycles M(B) plotting the XMCD signals as a function of the external magnetic field (B) at fixed temperature (T = 8 K) with the field applied perpendicular (left panels) and at grazing angle (right panels) to the sample surface. For the $ErPc_2$ molecules, only the curve at $\theta = 70°$ has been recorded, given the vanishingly small signal observed at normal incidence. Along with the Ln magnetization of the $LnPc_2$ molecules, the corresponding magnetization for the Ni substrate is shown in figure 5.19 (a) and (b). The Ni single crystal used here is the same that has been used for the studies in chapter 3. Hence, the field dependence reveals the same behavior, an easy magnetic axis in-plane and a hard magnetic axis perpendicular to the surface. For the easy axis of magnetization, a non-linear behavior for small magnetic fields is observed and no magnetic remanence occurs as expected for a ferromagnet. This is a result of magnetic domains with different orientation, which add up to a macroscopic magnetization of $M = 0$. The saturation field is ≈ 0.2 T for $\theta = 70°$ and ≈ 0.5 T for $\theta = 0°$. The field dependence of the Tb magnetization shows some characteristic features. For both angles, $\theta = 0°$ and $\theta = 70°$, an antiferromagnetic coupling is visible, analog to the magnetization cycles in section 3. The curves cross zero field three time, revealing antiparallel magnetic moments of Tb and Ni at small external fields. For higher magnetic fields, the Tb moments are parallel oriented and the magnetization curve has a paramagnetic shape. Since the Ni(111) single crystal - in

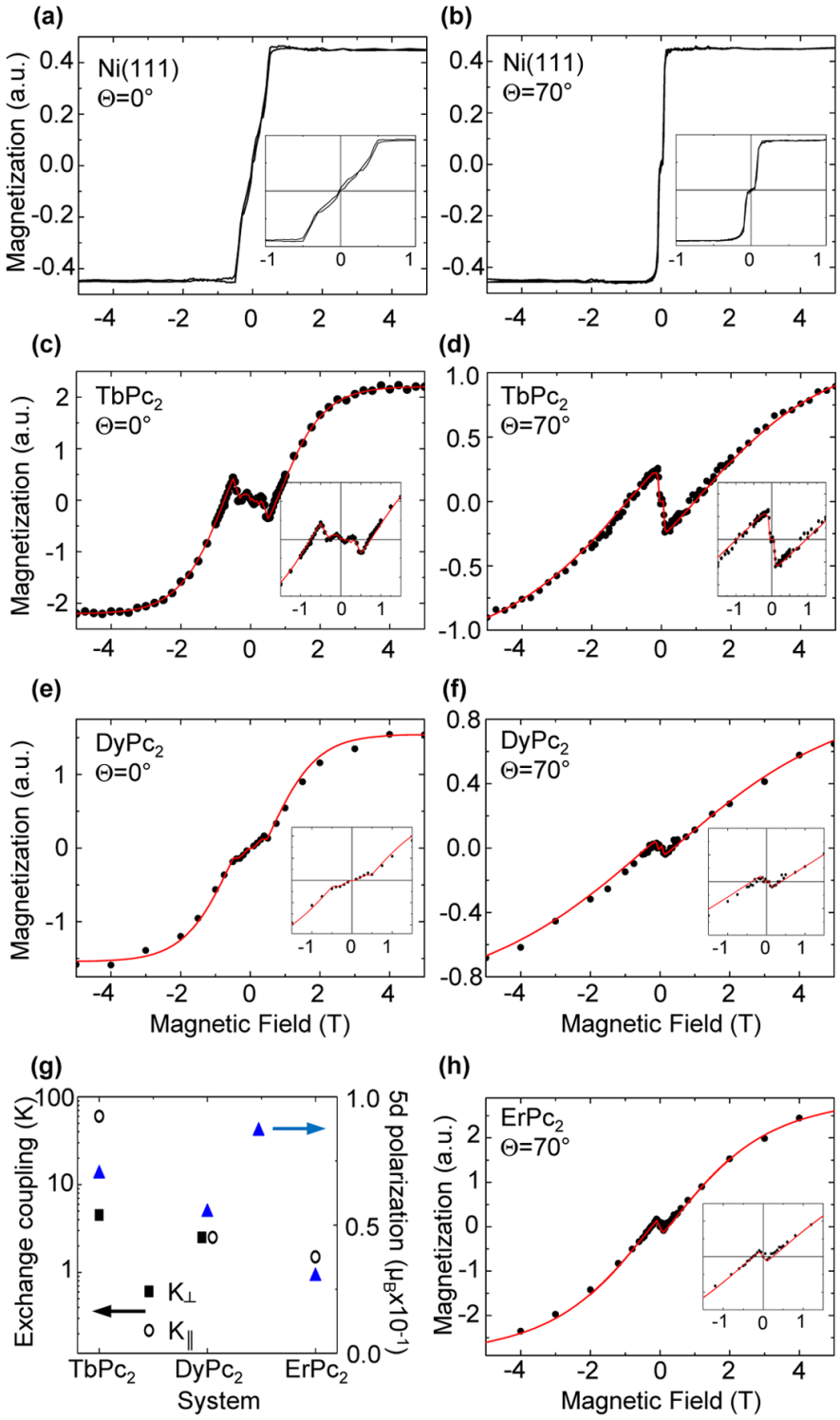

Figure 5.19.: Element-resolved magnetization measurements of Ni(a-b)(inset: magnification of the low field region), Tb(c-d), Dy(e-f), Er(h) for $LnPc_2$/Ni(111) systems, taken at $\theta = 0°$ (left panels) and $\theta = 70°$ (right panels) incidence angles. Experimental data are shown as black dots, while the theoretical fit as the continuous red line)(insets: magnification of the low field region). Panel (g): exchange coupling constant (left axis) as determined from the fit and magnitude of the magnetic polarization (right axis) induced on the $5d$ orbitals for each Ln compound [65].

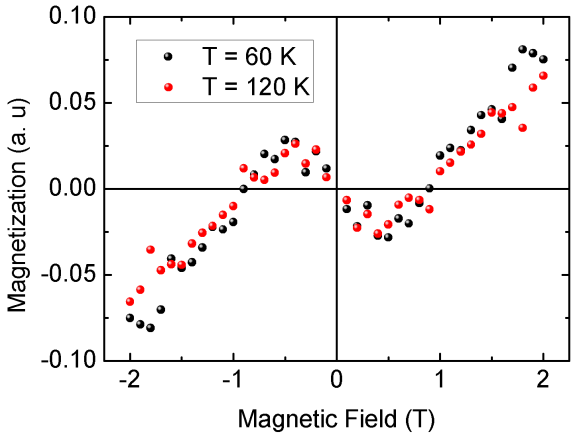

Figure 5.20.: Temperature-dependent magnetization of Tb. The antiferromagnetic coupling remains visible at $T = 60$ K (black) and $T = 120$ K (red).

contrast to the thin Ni film on Cu(100) - does not show a remanent magnetization , remanence of the Tb ions can neither be observed. The magnetization curves of Tb between the Ni saturation fields reflect the main features of the magnetization curves observed for the Ni substrate: an abrupt change in the slope of the magnetization is observed at B_S. These features confirm the antiferromagnetic character of the coupling of the Tb's magnetic moment to the Ni substrate consistently with what has been recently reported in Ref. [25].

The magnetization curves corresponding to the Dy magnetization show a very similar trend as the ones for Tb. However, the characteristic features for the magnetic coupling are less pronounced. Both, the coercive field and the maximum antiparallel magnetization are clearly smaller than for Tb. While the slope of the curve for grazing incidence still changes the sign for low field, leading to three zero crossings, at normal incidence the curve only becomes flatter around zero field, indicating the antiferromagnetic coupling. For $ErPc_2$ only the magnetization curve for $\theta = 70°$ is presented, since no evident coupling is identifiable for $\theta = 0°$ as result of the in-plane magnetization of Er. For grazing incidence, a similar shape of the magnetization curve is observed, revealing also antiferromagnetic coupling between Ni and $ErPc_2$.

One reason for the approach of coupling SMM molecule to a ferromagnet, is the extremely low blocking temperature of the $LnPc_2$ molecules. In chapter 3 it was already shown that the coupling of planar molecules is strong enough to observe remanent magnetization of the molecules at room temperature. The coupling between the ferromagnetic substrate and the $LnPc_2$ is clearly weaker. However, temperature-dependent hysteresis measurements have been performed to determine the coupling at higher temperature. Figure 5.20 shows the magnetization curves

taken at the Tb edge normalized to the pre-edge as described before. Since several temperature points have been measured, only one part of the magnetization curve ($-2 \leq B \leq 0$ T) was measured and for the optical presentation symmetrically added on the other side ($0 \geq B \geq 2$ T). For the qualitative presentation this method is reasonable and will not distort the result. At 60 K and even at 120 K, the coupling is clearly visible by the characteristic shape of the magnetization curve. Though at room temperature the coupling cannot be identified, a magnetization at 120 K is an important improvement compared to the blocking temperature of the molecule, since a temperature of 120 K can be achieved by cooling with liquid nitrogen, which is easier and much cheaper than cooling to 4 K or lower temperatures.

In contrast to $3d$ transition metal systems, the orbital moment in such $4f$ systems is not negligible. $\boldsymbol{L}$ can even overcome $\boldsymbol{S}$, e.g. for Dy $\boldsymbol{L} = 5$, $\boldsymbol{S} = 5/2$. In order to quantify the strength of the molecules-substrate magnetic coupling, the system with the following spin Hamiltonian was modeled [25]

$$\boldsymbol{H} = \mu_{\mathrm{B}}(\boldsymbol{L} + 2\boldsymbol{S}) \cdot \boldsymbol{B} - \lambda \boldsymbol{L} \cdot \boldsymbol{S} + V_{CF} + \boldsymbol{M}_{Ni} \cdot \boldsymbol{K} \cdot \boldsymbol{S}_{Ln}, \tag{5.2}$$

where μ_{B} is the Bohr magneton, **S** and **L** the spin and orbital moments of Ln, λ the spin-orbit constant, and $\boldsymbol{V}_{LF}$ is the contribution from the LF and can be written as [53, 178, 179]:

$$\boldsymbol{V}_{LF} = A_2^0 \left\langle r^2 \right\rangle \alpha \boldsymbol{O}_2^0 + A_4^0 \left\langle r^4 \right\rangle \beta \boldsymbol{O}_4^0 + A_4^4 \left\langle r^4 \right\rangle \beta \boldsymbol{O}_4^4 + A_6^0 \left\langle r^6 \right\rangle \gamma \boldsymbol{O}_6^0 + A_6^4 \left\langle r^6 \right\rangle \gamma \boldsymbol{O}_6^4 \tag{5.3}$$

with $A_k^q \left\langle r^k \right\rangle$ parameters to be determined, α, β and γ constants, see reference [178] and the $\boldsymbol{O}_k^q$ matrices are polynomials of the total angular momentum matrices $\boldsymbol{J}^2$, $\boldsymbol{J}_z$, $\boldsymbol{J}_-$ and $\boldsymbol{J}_+$ [179].

$$O_2^0 = 3J_z^2, \tag{5.4}$$

$$O_4^0 = 35J_z^4 - [30J(J+1) - 25]J_z^2, \tag{5.5}$$

$$O_6^0 = 231J_z^6 - (315J - 735)J_z^4 + (105J_2 - 525J - 294)J_{z^2}. \tag{5.6}$$

Assuming no particular distortion of the molecules when deposited on surface, the values reported for molecules on bulk [53] have been taken for the parameters in V_{LF}. The magnetic coupling between the Ln and the magnetic substrate is modeled with the exchange-like term $\boldsymbol{M}_{Ni} \cdot \boldsymbol{K} \cdot \boldsymbol{S}_{Ln}$. This model implies that isolated magnetic moments of the Ln molecules are coupled to the nearest atoms of the substrate for which the vector $\boldsymbol{M}$ represents an average, going beyond the simple Heisenberg model for the exchange developed for two isolated magnetic centers [180]. The components of the diagonal tensor **K** are $K^{\perp}$ and $K^{||}$, which correspond to the fitting

parameters. Because of the large spin-orbit coupling in all Ln (212 meV for Tb and even higher for Dy and Er), L and S are parallel aligned and therefore

$$J = J_{max} = L + S \tag{5.7}$$

and the introduction of the operator $\boldsymbol{n}$

$$\boldsymbol{n} = \boldsymbol{J}/J = \boldsymbol{L}/L = \boldsymbol{S}/S \tag{5.8}$$

results in the following expression of the Hamiltonian

$$\boldsymbol{H} = \mu_{\mathrm{B}}(L + 2S)\boldsymbol{B_{eff}} + \boldsymbol{B} - \lambda \boldsymbol{L} \cdot \boldsymbol{S} + V_{CF} \equiv \boldsymbol{B}_T \cdot \boldsymbol{n} - \lambda \boldsymbol{L} \cdot \boldsymbol{S} + V_{CF}, \tag{5.9}$$

where

$$\boldsymbol{B}_{eff} \equiv (SK^{||}(M_{Ni,x}, M_{Ni,y}, M_{Ni,z})/[\mu_B(L + 2S)]. \tag{5.10}$$

For $\boldsymbol{M}_{Ni}$ the experimental determined magnetization $M(B)$ of Ni is taken, leaving only $K^{\perp}$ and $K^{||}$ as fitting parameters. For $TbPc_2$ and $DyPc_2$ the curves at $\theta = 0°$ were first used to determine $K^{\perp}$. Subsequent the values for $K^{||}$ became accessible by fitting the curves at grazing photon incidence. As consequence of the Er in-plane magnetization, no reasonable $M(B)$ curve for θ= 0° is available. Hence, only $K^{\perp}$ was used to fit the experimental data, finding the best fit for $K^{||}$ = 1.5 K. With this result it was verified that $K^{\perp}$ has no effect on the calculated curve, even for chosen values as large as 20 K. The fits from the described model Hamiltonian are shown in figures 5.18 (c)-(f), (h) as continuous red line. The fit matches the experimental data extremely well. The precise congruence even in the low field region ($B < B_S$) clearly confirms the assumption of an exchange coupling with an intensity proportional to the magnetization of the substrate. Hence, all the characteristic kinks in the magnetization curve of the Ni single crystal are visible in both, the experimental and fitted magnetization curve of the Ln magnetization. Though the use of a macroscopic single crystal instead of a thin film has the disadvantage of the absent magnetic remanence, the characteristic features in the low field range help to determine and confirm the coupling. The specific values of $K^{\perp}$ and $K^{||}$ for $TbPc_2$, $DyPc_2$ and $ErPc_2$ are summarized in figure 5.18 (g). The anisotropic coupling is clearly shown by the difference between $K^{\perp}$ and $K^{||}$. The values of the K component along the molecules easy axis, i.e. $K^{\perp}$ for Tb and Dy and $K^{||}$ for Er, display a clear trend going from Tb (maximum) to Er (minimum), while however they are in the same order of magnitude. These results show that the interaction between $LnPc_2$ molecules and the magnetic substrate depends on the specific lanthanide ion. Since the organic ligand is identical for the three molecules, the character of the Ln orbital wave-function should play a key role in determining the magnetic anisotropy and interactions [39, 181, 182].

A simple description of the anisotropic coupling is given by the experimental data 5.18 (c-f), the Hamiltonian in equation 5.9 and the illustration in figure 5.21.

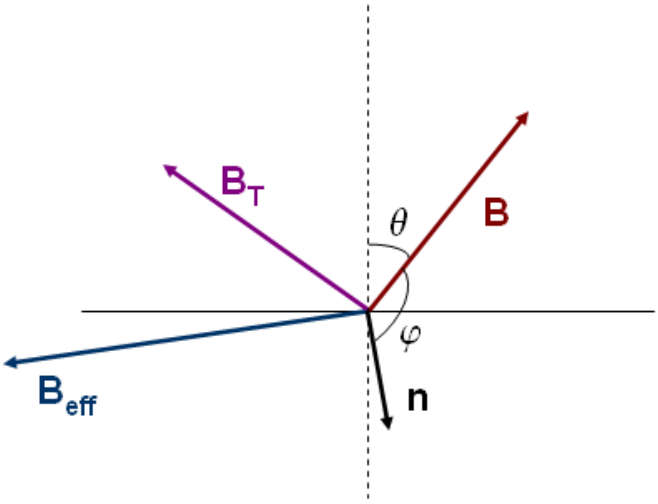

Figure 5.21.: Qualitative representation of the magnetic field ($\boldsymbol{B}$), the effective field related to the molecule-substrate coupling ($\boldsymbol{B}_{eff}$), their sum ($\boldsymbol{B}_T$) [65].

Let's assume an isotropic coupling, which is tantamount to $K^{\perp} = K^{||} = K$ and $\boldsymbol{B} \,||\, \boldsymbol{B}_{eff} \,||\, \boldsymbol{B}_T$. In general, the expectation values of the molecules spin and orbital moment are tilted with respect to $\boldsymbol{B}_T$ because of the ligand field anisotropy. $\boldsymbol{B}_T \cdot \boldsymbol{n} = 0$ only for $\boldsymbol{B}_T = 0$, which means the crossing field can be written as

$$B_C = \frac{SMK}{\mu_B(L + 2S)} \tag{5.11}$$

and does not depend on the orientation of $\boldsymbol{B}$. However, a clear difference in the crossing fields is observed at $\theta = 0°$ compared to $\theta = 70°$ (figure 5.21), excluding the assumption of an isotropic coupling.

Figure 5.21 shows qualitatively the orientation of $\boldsymbol{B}$, $\boldsymbol{B}_T$, $\boldsymbol{B}_{eff}$ and $\boldsymbol{n}$ for an anisotropic coupling. In this case, $K^{\perp} \neq K^{||}$ and $\boldsymbol{B}_{eff}$ is tilted with respect to $\boldsymbol{B}$. The following example illustrates the interplay between the anisotropy induced by the ligand field and the one related to the anisotropic molecule-substrate coupling. Let's assume an applied magnetic field parallel to the xz-plane and a ligand field with an axial symmetry. Then the y-component can be neglected and the vectors in figure 5.21 can be written as

$$\boldsymbol{B} = (B_x, B_z) = (B\sin\theta, B\cos\theta) \tag{5.12}$$

$$\boldsymbol{B}_{eff} = (B_{eff,x}, B_{eff,z}) = (SK^{||}M\sin\theta, SK^{\perp}M\cos\theta)/[\mu_B(L + 2S)]. \tag{5.13}$$

The crossing field B_C corresponds to a vanishing expectation value of the molecule angular momentum along the field direction

$$\boldsymbol{B}\cot\langle\boldsymbol{n}\rangle \propto (SK^{||}M + b_c)M\sin^2\theta + \beta(SK^{\perp}M + b_c)\cos^2\theta = 0, \tag{5.14}$$

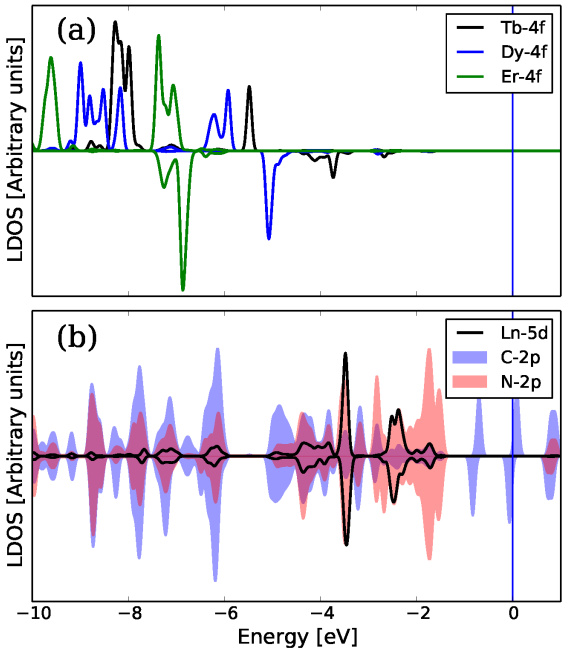

Figure 5.22.: Spin-resolved local density of states (LDOS) of the $LnPc_2$ molecules as calculated by DFT. In panel (a) the projection on the $4f$ orbitals of Ln = Tb, Dy and Er is given, while in panel (b) the projections on the $5d$ orbital of Tb (the one for Dy and Er is very similar) and on the $2p$ orbitals of the nearest-neighbors (to the Ln ions) N and C atoms (which is only weakly modified by the choice of the Ln) in the phthalocyanine planes are superimposed. In each panel, the upper (lower) side is relative to the majority (minority) spin channel. d-character in panel (b) has been enhanced for better comparison [65].

where β is a factor taking into account that z is the easy axis ($\beta > 1$) or the hard axis ($\beta < 1$) and $b_c = \mu_B(L + 2S)B_C$. Equation 5.14 is satisfied for

$$\tan^2\theta = -\beta(SK^{\perp}M + b_c)/SK^{||}M + b_c. \tag{5.15}$$

This equation states that $\langle \boldsymbol{n} \rangle$ is only orthogonal to the applied field, if the molecule-substrate coupling overcompensates the Zeeman energy in one direction.

To get a deeper insight DFT calculations were performed on $TbPc_2$, $DyPc_2$, $ErPc_2$ molecules in gas phase with the Perdew-Burke-Ernzerhof (PBE) [131] exchange correlation functional as implemented in Quantum Espresso [183] including static correlation effects using the LDA+U formalism [184]. The calculations were performed using the projector augmented wave method (PAW) [185] as recently implemented in the pseudopotentials made by Andrea Dal Corso [186]. The influence of

the on-site Coulomb interaction imposing static correlation effects on the f electrons of the Ln ions was taken into account [184] (the values of U and J have been taken by Reference [187]. The same values for $U = 9$ eV and $J = 1$ eV were chosen for all three different ions, Tb, Dy and Er). No spin-orbit coupling is included in the calculation. The systems were modeled with a tetragonal supercell of $20 \times 20 \times 14$ Å. Regarding the kinetic and charge density cutoffs, 121 and 620 Ry, 125 and 499 Ry, 135 and 578 Ry, respectively have been chosen for $TbPc_2$, $DyPc_2$ and $ErPc_2$. A smearing parameter of 8×10^{-4} Ry ensured a correct description of the spin radical in the two Pcs. The version of Quantum Espresso used in all the calculations was the 5.0.3.

Figure 5.22 shows the spin-resolved projected local density of states (LDOS) of the $LnPc_2$ complexes. The $4f$ states for each of the three Ln ions are presented in (a), the Ln-$5d$, C-$2p$ and N-$2p$. The $2p$ states are the ones close the Ln ion, which basically carry the spin-polarization of $S = 1/2$ delocalized over the two Pc rings. Tb^{3+} has eight $4f$ electrons, Dy and Er have nine and eleven, respectively. The more electrons occupy the $4f$ electrons, the further down in energy are the electronic levels. For all three Ln, the $4f$ levels are clearly below the Fermi level. In (b) a partial occupation of the $5d$ orbitals together with a small spin polarization is observable in all the three cases with the same sign of the f spin moments. The $5d$ electrons, in turn, occupy the same energy regions as the p states of C and N. This indicates the most likely exchange path between the ferromagnetic substrate and the Ln ion. The Ni $3d$ state hybridize with the N and C $2p$ states, since the C and N atoms of the lower Pc ring are in direct contact with the surface. Furthermore the $2p$ states of C and N hybridize with the Ln $5d$ states, which in turn, hybridize with the $4f$ states. The induced polarization values being given in figure 5.19 (g), being 0.07 μ_B, 0.06 μ_B and 0.03 μ_B, respectively for Tb, Dy and Er. Despite the values are very small, they confirm the experimental findings for the coupling strengths, which is strongest for Tb and weakest for Er. These theoretical findings are not limited to this specific system, but may help to develop a more general understanding of the communication of $LnPc_2$ molecules or other Ln-based complexes with their environment. This result has direct implications for recently published studies focusing on $LnPc_2$ and analogue compounds, where the magnetic coupling between the Ln ions to the external world is important [14, 15, 17, 25, 173, 188].

The general origin of the anisotropic coupling is also studied with supporting calculations. In previous publication this was just attributed to the large unquenched orbital moment of the Tb ion [25]. However, the more general approach with three different Ln ions in the here presented study demonstrates that despite the fact that all Ln ions have large orbital moments, the anisotropic character of the coupling reveals major differences. Figure 5.23 shows the spin-resolved charge density for all three molecules, $TbPc_2$ (a), $DyPc_2$ (b) and $ErPc_2$ (c). The orbital part of the total moment of the Ln ions is carried by the minority f states. Only the orbitals, which are in the energy window, where these minority $4f$ states are present, were summed up to the spin-resolved partial charge density. The charge

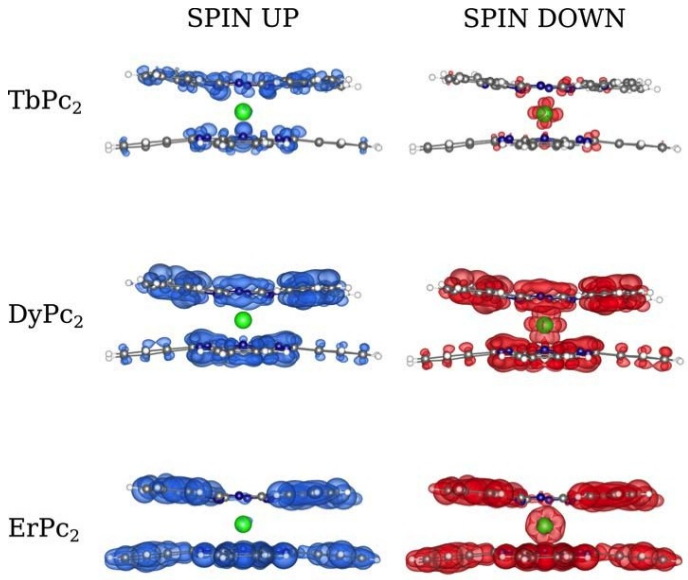

Figure 5.23.: Spin-resolved charge density integrated in an energy window of ≈ 0.3 eV around the minority f states of the $LnPc_2$ systems, for Ln = Tb, Dy and Er. Left (right) panels refer to the majority/up (minority/down) spin component, depicted in blue (red). The C, N, H, are colored dark gray, dark blue and white, respectively, while the Ln ion are all in light green [65].

density becomes more spherical with increasing number of electrons, or in other words, less unoccupied $4f$ orbital. A more symmetric charge density results in a weaker dependence of the overlap with the phthalocyanine orbitals on the magnetic quantum number of the Ln. Hence, for $TbPc_2$ the depends relatively strong on m_l, while $ErPc_2$ is relatively independent on m_l.

5.6. Tuning the magnetic properties with an interlayer of graphene

As seen in chapter 4, an interlayer of graphene can have a remarkable influence on the coupling. The coupling strength changes and the coupling can even be switched from ferromagnetic to antiferromagnetic for CoOEP on Ni(111), if the graphene layer is placed between the molecules and the Ni substrate. Consequently it is important to study the influence of the graphene interlayer also on the coupling between the Ni substrate and the $LnPc_2$ molecules. The spin-hybrid systems are very similar to each other. However, the coupling mechanisms are complex and depend strongly on small changes, e.g. the exchange of the central $3d$ ion in the molecules' center. Especially for the $LnPc_2$ molecules the coupling mechanism is

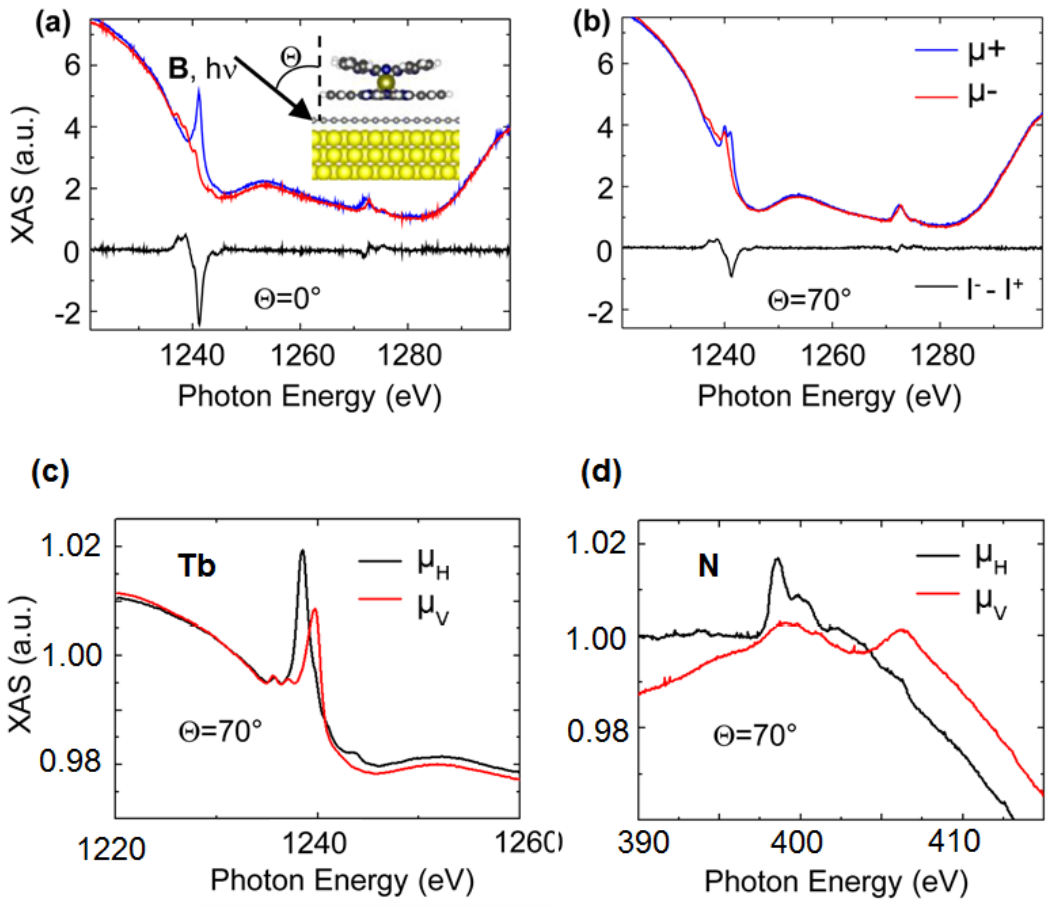

Figure 5.24.: (XAS and XMCD spectra for $TbPc_2$ in $TbPc_2$/SLG/Ni(111) at $\Theta = 0°$ (a) and $\Theta = 70°$ (b). XLD at the Tb (c) and N (d) edges.

different compared to the planar $3d$ metal complexes, since the strongly localized $4f$ electrons are responsible for the magnetic properties of the Ln.

The x-ray absorption results on the sample $TbPc_2$/SLG/Ni(111) will be described in the following paragraphs.[4] The preparation and characterization of the graphene layer on the clean Ni(111) surface has been made with the same procedure described in chapter 4. Subsequently, 0.2 ML of $TbPc_2$ molecules were thermally evaporated onto the graphene surface. The experiments have been performed at the ID08 beamline at the ESRF.

Figure 5.24 shows the absorption spectra for circularly polarized x-rays and the XMCD at the Tb $M_{4,5}$ edges in an external magnetic field of $B = 5$ T at $T = 8$ K for the photon incidence angle $\Theta = 0°$ (a) and $\Theta = 70°$ (b). The spectra

[4]Theoretical studies are currently performed on this particular system for a deeper understanding.

below show the absorption spectra for horizontally and vertically polarized x-rays at the Tb $M_{4,5}$ edge (c) and N K edge (d) for grazing incidence $\Theta = 70°$. The results combined reveal that the $TbPc_2$ molecule shows the same absorption geometry and anisotropy properties as on Ni(111). The Pc plane is parallel to the surface and the strong uniaxial anisotropy is preserved on the graphene surface.

To observe the coupling between the molecules on the substrate, the intensity of the XMCD as a function of the magnetic field has been recorded and is shown as magnetization cycle in figure 5.25. The figure shows the Tb magnetization cycles for $\Theta = 0°$ (a) and $\Theta = 70°$ (b) and the Ni magnetization (c) and (d). A zoom of the low field region of (b) is shown in (e) together with the theoretical curve of non-interacting molecules (red dots). The straight red line in (a), (b) and (c) corresponds to the model fit, described in the following. The curve taken in (e) displays a small kink, which is the signature of the antiferromagnetic coupling with the underlying Ni substrate, consistently with what has been shown in the chapters 5.4 and 5.5, although here the intensity of the coupling is much reduced due to the inclusion of the graphene interlayer. In order to quantify the strength of the molecules-substrate magnetic coupling, the model from the previous chapter 5.5 is used. Since the coupling is extremely small at $\Theta = 0°$, only an upper limit for the interaction can be determined: $K^{\perp} < 0.2$ K. Below this threshold the accuracy of the fit falls below the incertitude in the experimental data. For $\Theta = 70°$ the coupling is clearly visible (e) and a value of $K^{||} = 20$ K is determined, while $K^{\perp} = 0$ K. The significant difference between the two directions can be understood considering the different M(B) curves of the Ni(111) single crystal substrate: the saturation magnetization is lost for all fields smaller than 0.5 T at $\Theta = 0°$ and 0.2 T at $\Theta = 70°$. Since the interaction is proportional to the magnetization of both Tb and Ni, it turns out the lower visibility for the $\Theta = 70°$ geometry. Due to the huge difference in the coupling constants $K^{||}$ and $K^{\perp}$, it can be concluded that the coupling is strongly anisotropic in agreement with the findings in 5.5. Though the coupling strength is extremely small, it obviously is present. The comparison of the red dots and the experimental curves in (e) clearly demonstrate that the molecules are coupled. In this spin-hybrid system, the interlayer of graphene leads to a smaller coupling than on the bare Ni(111) surface, however, the antiferromagnetic coupling is still preserved.

5.7. Integrity of the molecule

For investigations on molecular systems, especially in the monolayer regime, the integrity of the molecules always has to be guaranteed. Though $LnPc_2$ molecules are known for a high thermal and chemical stability, the integrity of the molecules was checked by different methods. There are basically three critical processes, in which the molecules can be harmed after their succesful synthesis decribed in

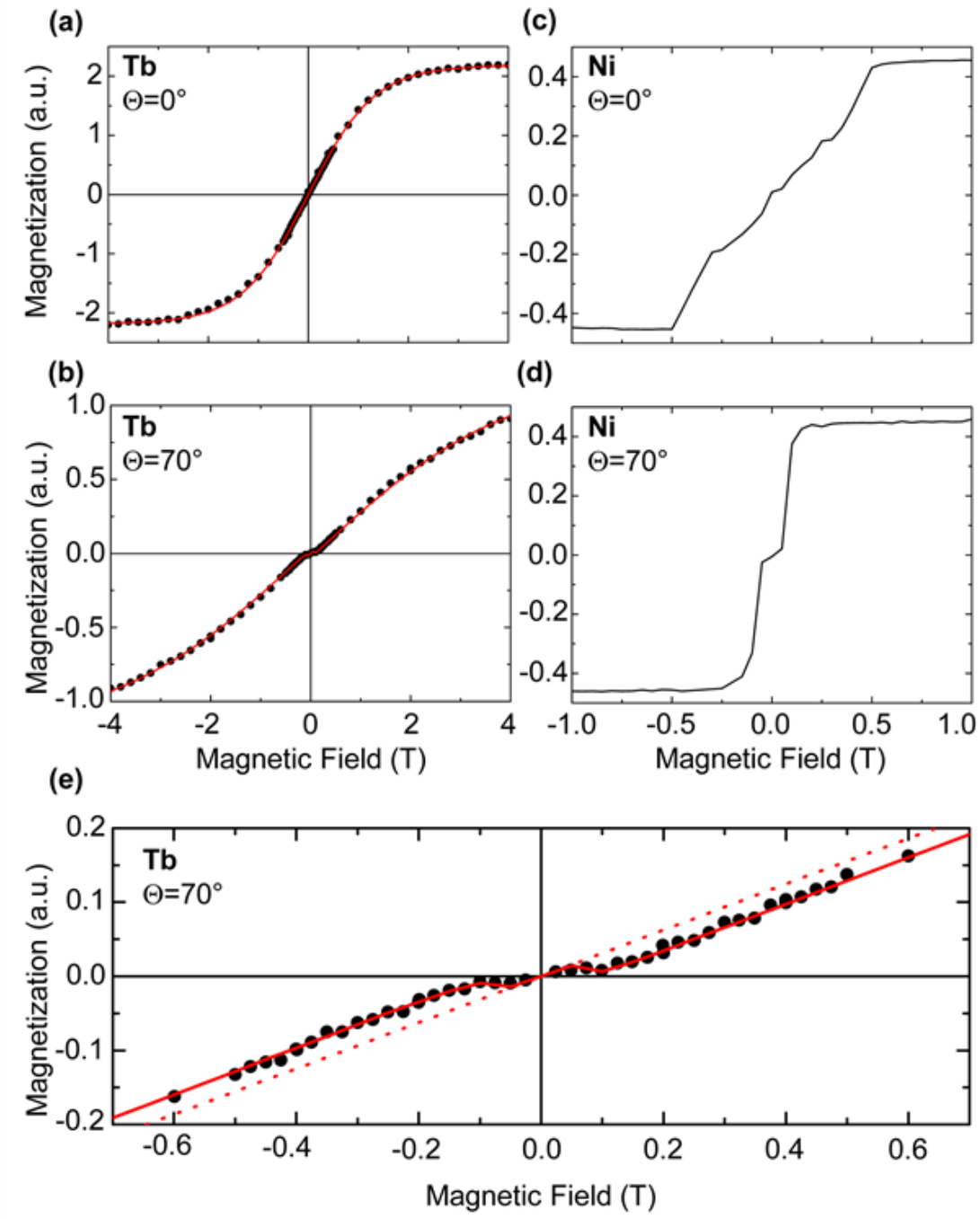

Figure 5.25.: Magnetization of the $TbPc_2$ molecules on SLG/Ni(111) for $\Theta = 0°$ (a) and $\Theta = 70°$ (b). The black dots represent the experimental results and the red line the theoretical fit. Corresponding magnetization for the Ni substrate are shown in (c) and (d). In (e) a zoom of the low field region is presented, the red dots correspond to the theoretical simulation of the magnetization of uncoupled molecules.

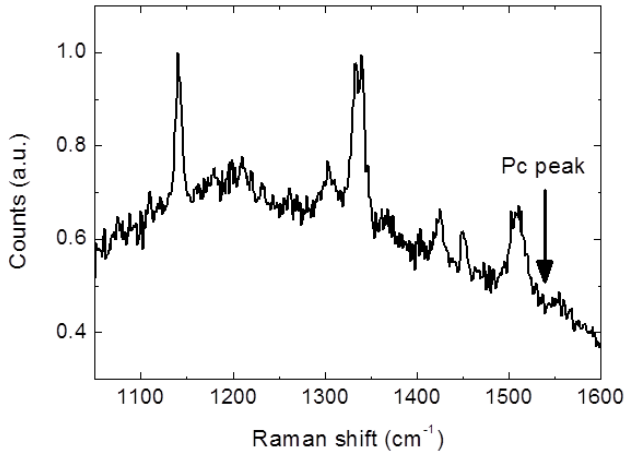

Figure 5.26.: Raman spectrum of the $TbPc_2$ molecules evaporated as described in the main text on Ni(111). We did not observe the peak associated with the presence of isolated Pc moieties.

section 5.2. The first process is during the thermal evaporation. It has to be checked if the heat only cause the subsequent sublimation of molecules or if it can also destroy individual molecules. The second process is the contact with the surface. Especially on metallic substrates, the molecules interact strongly with the surface atoms. These interaction can also affect the intramolecular bonding, e.g. bond length, angle and strength. It was previously reported that $TbPc_2$ double-decker may decompose into two phthalocyanine halves when deposited on Au(111) metal surface [189, 190]. The third process is the x-ray absorption measurement itself. Synchrotron radiation, especially at undulator beamlines, has an extreme high intensity, which can easily destroy certain molecules within seconds. Therefore the experiments with molecules have never been performed with the highest intensity and the spectra were carefully observed for time effects. However, one still has to make sure that the molecules are intact after the measurement.

For the determination of the thermal stability of $TbPc_2$, perfomed by Dr. Svetlana Klyatskaya in Karlsruhe, the sample was exposed to high temperature sublimation under high vacuum in the sublimation apparatus consisting of a tube flask dipped into a heating mantle and a condenser. This method is carried out by heating 80 mg of the crude solid, while simultaneously evacuating the system. Upon reaching 400 - 420 °C at the bottom of the round flask and at a standard pressure in the system about 2.8×10^{-2} mbar, the sublimate appears on the cooled condenser. After 40 min about half of the crude solid was collected on the condenser. Both the sublimate and the residual molecules in the tube flask were exposed to mass-spectrometric and spectroscopic analysis as well as the rest of the sample from a Knudsen cell. Maldi-ToF and UV-VIS spectra did not reveal any difference

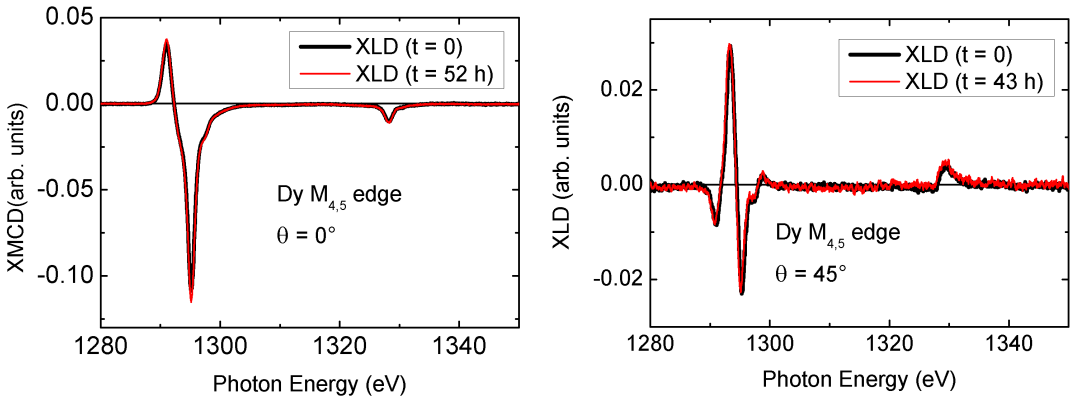

Figure 5.27.: Time dependence of XMCD and XLD to determine the resistance of the molecules against radiation. The black line shows the XMCD (XLD) at the beginning, the red line represents the XMCD (XLD) after 52 (43) hours of irradiation.

comparing to the initial sample. Presence of binuclear complex (Tb_2Pc_3) in the Maldi-ToF spectrum as an evidence of thermal degradation was detected only in the rest of the sample in the tube flask after exposure at more than 450 °C for no less than 30 min. This allows us to assert that sublimation at 400 °C leaves the molecules unaffected.

In addition, Raman spectroscopy on the submonolayer of $TbPc_2$ evaporated on Ni(111) was performed, shown in Figure 5.26. Raman spectra clearly show the presence of all the peaks associated with the thin film $TbPc_2$ molecules at 1140, 1302, 1335, 1425, 1450 and 1515 cm^{-1} as previously reported in Reference [191] for molecules deposited on graphene from solution, while the peak associated with the Pc species [192] at 1540 cm^{-1} is absent. It is therefore shown that the molecules remain in the double-decker structure on the Ni(111) surface and do not break into two separate Pc rings.

In figure 5.27 the time dependence of the spectra is shown to see the effect of long irradiation on the molecules. The spectra of the sample $DyPc_2$/HOPG were recorded at the SLS (results discussed in section 5.2). Most of the samples described in this thesis were measured between 8 and 16 hours, before a new sample is prepared. However, the sample corresponding to the spectra in figure 5.27 was cooled down in the dilution refrigerator (see chapter 3.2.3) and it was measured for a few days.[5]) The spectra do not show any changes even after this permanent

[5]Warming up and cooling down again the dilution refrigerator takes about 24 hours and in the meanwhile no measurements can be recorded. This delay of time is not affordable during a beamtime.

irradiation of about two days. No indication of radiation damage can be observed. Similar results have been seen on a shorter time-scale for all $LnPc_2$ molecules on different substrates. No published material was found reporting about synchrotron radiation damaging $LnPc_2$ molecules, which confirms their high stability.

Another indication of the integrity of the molecules at all times are the STM images taken at the ID08, ESRF. The images of $TbPc_2$/Ni(111) are shown in the previous section in figure 5.15. Though the resolution is not high enough to see the individual atoms of the molecules, the lateral size and height of the molecules clearly suggest that the molecules are intact on the surface. No changes in the STM patterns occur after the x-ray absorption experiment and therefore it can be concluded that the molecules resist the radiation and remain unharmed.

6. Conclusion

Molecular spin-hybrid systems are a fascinating topic of modern research. The interaction between substrates and molecules has been proved to allow the modification of structural, electronic and magnetic properties of both, the molecules and the underlying substrate. This and the possibility to change the magnetic properties by small variations of the systems have been investigated within this work. State of the art technologies make it possible to prepare samples with a precision of a submonolayer (MBE, micro balance), to characterize lateral structures (LEED) and even to observe the surface in atomic resolution (STM). The main experimental techniques used to study the electronic, magnetic and structural properties of the molecular spin-hybrids in this work were element-selective XAS, XLD and XMCD. The selectivity of these techniques enables to differentiate the elements in a sample and magnetic properties can therefore be studied separately for all included elements. This is crucial to determine magnetic coupling phenomena. Thanks to the extreme sensitivity of synchrotron radiation, it was possible to analyze submonolayers of atoms and molecules, including planar molecules (FePc and CoOEP) and single molecular magnets ($LnPc_2$) deposited on various substrates and study the magnetic coupling mechanisms. The variety of investigated systems enables to determine the impact of the individual contributions on the coupling. DFT calculations have been performed and they confirmed the experimental XAS findings, but also provided with complementary results helping to describe the coupling phenomena.

The properties of FePc molecules have been investigated on four different substrates: Co/Cu(100), O/Co/Cu(100), Ni(111) and graphene/Ni(111). In direct contact with the magnetic substrate, the system showed the expected ferromagnetic coupling. This coupling results mainly from a direct interaction between the Fe ion and the underlying Ni atoms, but is also mediated in a 90° exchange interaction via the C and N atoms of the ligand, which carry small magnetic moments. Interestingly an interlayer of oxygen modifies the coupling from ferromagnetic to antiferromagnetic, while the insertion of a graphene layer between the molecules and the substrates maintains the ferromagnetic character of the system. The oxygen layer forms a $(\sqrt{2} \times \sqrt{2})$ superstructure on the surface with well separated O atoms, resulting in localized p orbitals. The Fe ions, located above the O atoms, couple antiferromagnetically to the substrate. This indirect coupling via the O atom can be understood as a 180° superexchange coupling. According to DFT calculations, the spin state is unaffected by the O layer, i.e. with and without

O the FePc molecule is in an $S = 1$ spin state. On graphene the scenario is different because the C atoms form a continuous graphene layer instead of isolated atoms. DFT calculations revealed that the extended π orbitals of the C atoms combined with the contributing Fe orbitals are responsible for the ferromagnetic coupling in this system. Due to the continuous layer character of graphene, the ferromagnetic coupling is robust with changing the adsorption position of the molecule.

The adsorption structure has been studied by means of LEED, XLD and DFT. The LEED analysis showed a self-assembled layer of the molecules in two domains on an O/Cu(100) surface. However, due to the mobility of the molecules, clear LEED patterns are only visible for a temperature of $T = 80$ K. The determination of the π^* and σ^* resonances from angle-dependent XAS at the N K edge clearly showed the lying orientation of the molecules on all investigated substrates. In paralell, DFT was able to distinguish between the two non-equivalent N atoms and separate their contribution to the spectra. All calculated results match well the experimental data. In addition, the molecule-surface distances have been calculated for all substrates. While on the bare metal surface the distances are small, revealing chemisorbed molecules, on oxygen and graphene the distances are rather large, indicating only a physisorption of the FePc molecules. These theoretical findings are supported by the structures in the spectra on the metal and more pronounced fine structures on graphene and oxygen, closer to the spectra of a free molecule.

The second planar molecule studied in this work, the CoOEP molecule, has been deposited on the same substrate (graphene/Ni(111)) as FePc. In contrast to FePc, the CoOEPs couple antiferromagnetically to the Ni substrate via graphene. Both, the different ligand and the central ion have been considered to be the origin of the different coupling type. DFT studies confirmed the experimental findings and revealed that the central ion plays the major role in determining whether the coupling is ferromagnetic or antiferromagnetic. The orbitals included in the magnetic coupling are responsible for the preferred spin alignment, parallel or antiparallel. While in the Co ion only the d_z^2 is involved in the magnetic interaction, several orbitals of the Fe contribute significantly to the coupling. Consequently, Co couples antiferromagnetically and Fe ferromagnetically. Both, the graphene and the oxygen layers have a decoupling effect. Hence, the coupling energies are significantly lower than on bare metallic surface.

The intermolecular coupling of molecules has been studied in a triple layer of CoOEP deposited on graphene/Ni(111). The element-specific field-dependent study of the magnetization clearly showed a decoupled system. The Co magnetization curve revealed a superposition of two contributions. One contribution is (above the saturation field of the Ni substrate) a constant magnetization antiparallel to the applied magnetic field. The second contribution observed is a paramagnetic signal, described by a Brillouin function. This Brillouin function represents the molecules in the second and third layer which are decoupled from

the first layer and behave paramagnetically. In high magnetic fields, the moments are aligned parallel to the field. The constant magnetization value is coming from the first molecular layer, which is coupled antiferromagnetically to the Ni substrate in any applied magnetic field. DFT calculations revealed an antiferromagnetic interlayer coupling between CoP molecules. However, it could be shown that slight changes of distances and tilting of the molecules cause a drastic reduction of the exchange energy. It is likely that the OEP ligands with their out-of-plane components lead to such an arrangement that differs from the perfectly aligned CoP multilayer. The two completely different magnetic behaviors of CoOEP molecules in the sample enable to switch the magnetic field by variation of the magnetic field. In the presented case of three layers, the switching fields occur at ± 2.5 T.

Aside the planar molecules, single molecule magnets of $LnPc_2$ type (Ln = Tb, Dy, Er) have been investigated as second class of molecules. These molecules are known to have finite blocking temperatures in bulk samples and therefore magnetic remanence is observed. However, the interaction with surfaces has a strong impact on the molecules causing the magnetic remanence to vanish on metallic surfaces. In this work submonolayers of $DyPc_2$ and $TbPc_2$ has been studied on HOPG, a very inert substrate which is expected to interact only weakly with the molecules. Field-dependent XMCD studies clearly revealed remanent magnetizations for both molecules on HOPG. The temperature has to be as low as $T \approx 4$ K for $TbPc_2$ and $T < 1$ K for $DyPc_2$, known to have a lower blocking temperature than $TbPc_2$. Even though the experimental temperatures are extremely low, it could be shown that the SMM properties can be maintained for the isolated molecules in contact with a surface. The relaxation times were estimated around an hour. This enables the detection of the remanence by XMCD. As expected, since the interaction between the substrate and the ligand must be similar to the planar molecules, the adsorption orientation of the molecules on HOPG, determined by XLD, showed that all molecules adsorb with the Pc ligand flat on the surface. The flat adsorption geometry was shown for all investigated $LnPc_2$ systems in this work.

However, in order to use the spin of the molecules in future applications, a stabilized magnetization at room temperature is one requirement. This requirement has led to the study of the manipulation of the molecular spin induced by its interaction with the substrate. The successful coupling of planar molecules has encouraged the study of SMMs on similar substrates including thin layers of Co and Ni films on Cu(100). The two systems have been chosen for their in-plane easy axis for Co and out-of-plane for Ni. An antiferromagnetic coupling was clearly shown for $TbPc_2$ on Ni/Cu(100) by field-dependent XMCD studies. The exchange energy is some orders of magnitude lower than determined for the planar molecules with 3d centers. As a consequence, the coupling energy can be overcome by the Zeemann energy in a magnetic field of a few Tesla, switching the magnetization of the molecules from antiparallel to parallel with respect to the applied field. The high single ion anisotropy of Tb prevents the magnetic moments to rotate

into the molecules' plane. Therefore the detection of a coupling to the in-plane magnetized Co film is not as clear as in the Ni system, but still possible. The out-of-plane components of the Co magnetization in the low-field region are coupled antiferromagnetically to the Tb ions.

The magnetic coupling mechanisms between magnetic substrates and $LnPc_2$ mole-cules, whose magnetism originates from $4f$ electrons, has to be different from the coupling to $3d$ ions, e.g. Fe or Co. To better understand the magnetic coupling between a magnetic substrate and $LnPc_2$, systematic studies of XMCD combined with DFT calculations of the system $LnPc_2$/Ni(111) (Ln = Tb, Dy, Er) have been performed. An antiferromagnetic coupling could be detected for all molecules despite their different magnetic properties. $TbPc_2$ and $DyPc_2$ exhibit a perpendicular anisotropy and $ErPc_2$ has a parallel anisotropy with respect to the Pc plane. The study shows a consistant trend for the coupling strength going from the strongest coupling for Tb to the weakest coupling for Er. Another important contribution of the DFT calculations was the determination of the communication channels in the system. The microscopic origin of the spin communication between the central Ln ion and its environment in the $LnPc_2$ compounds was identified as the spin polarization induced by the f-electrons on the $5d$ orbitals which in hybridize with the organic part of the molecules. The magnetic coupling mechanism differs clearly from the coupling of the planar molecules as expected due to the difference in the orbitals carrying the magnetic moments. The magnetic coupling was too weak to stabilize the Ln moments at room temperature, but for a temperature of $T = 120$ K an antiferromagnetic coupling could be detected making it possible to cool down with liquid nitrogen instead of liquid helium.

An interlayer of graphene has a decoupling effect similar to what was observed for the planar molecules. The weak coupling of $LnPc_2$ molecule with the magnetic substrate, combined with the decoupling effect of the graphene makes the experimental detection of a magnetic interaction extremely challenging. A very small antiferromagnetic coupling is however observed, showing that the magnetic coupling between the Tb ion and the Ni atoms is mediated via graphene and the Pc ring.

The presented results show the variety and the potential of molecular spin-hybrid systems, whose properties can be tailored by small modifications of the architecture. It is possible to engineer the desired properties by selecting the magnetic substrate, the crystallographic orientation and adlayers, combined with the choice of the molecule type. The systematic studies in this work delivered answers to the questions of assembly and orientation geometry of the molecules, molecule-surface distance, coupling mechanisms and communication channels. This is an important contribution to a global understanding of the magnetic interactions defining the magnetic properties in such a molecular spin-hybrid system. The research in this field has not reached an end yet, since many challenges have to be addressed on the way to future molecular spintronic applications. A

major challenge is a more detailed theoretical description of the $LnPc_2$ molecules interacting with surfaces. Chemistry designs and synthesizes new types of molecules with new properties, such as triple-decker molecules with two magnetic centers. Intramolecular exchange between the two centers has been presented in a recent publication [193] on Ln_2Pc_3 with two Ln ions instead of one in double-decker molecules. New systems need to be created and investigated in theory and experiment. These systems should combine both, a stable and a tunable magnetization at room temperature, which has not been discovered for $LnPc_2$ molecules. The fact that graphene mediates magnetic information between the substrate and the molecules enables several new approaches such as the intercalation of atoms to tune the electronic structure and magnetic properties of graphene. A multilayer system graphene/1 ML Eu/15 ML Ni/Ir(111) has been recently studied, showing that one ML of Eu can be stabilized via antiferromagnetic coupling to Ni up to $T > 450$ K [194]. Another major goal is to address and manipulate the spin of an individual molecule. In this work the preparation, manipulation and metrology was only executed on ensembles of molecules. For future molecular size devices, e.g. switches or data storage, a single molecular spin needs to be accessible. Further progress in preparation and detection techniques, combined with a deep microscopic understanding are therefore necessary.

A. Appendix

A.1. Computational methods for chapter 4.1.3

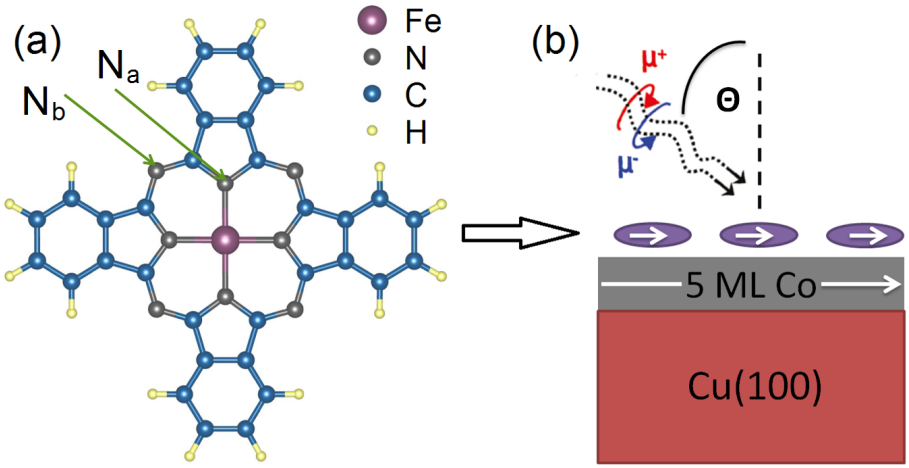

Figure A.1.: (a) Sketch of the FePc molecule composed of an Fe (purple) ion in the center, 8 N (gray), 32 C (blue), and 16 H (yellow) atoms. (b) Schematic illustration of the XMCD measurement for the sample FePc/Co/Cu(100) under the incidence angle θ.

Theoretical studies were performed by Dr. Heike .C. Herper, Dr. Biblap Bhandary and Dr. Sumantha Bhandary in the group of Prof. Olle Eriksson at the Uppsala University in Sweden. The following paragraph, which is a direct quote from reference [27] gives a detailed description about the calculations used to determine the results in chapter 4.1.2:

"The electronic and magnetic structures of FePc on bare and c(2×2)O/Co(001) have been determined from density functional theory (DFT) calculations using the VASP code [106] and the projector augmented wave approach (PAW) [107]. The localized character of the $3d$ orbitals was taken into account by the GGA+U approach. The effective $U_{\text{eff}} = U - J$ value used in the method of Dudarev [195] has been chosen to be 3 eV, which has been proven to give accurate results and is nowadays commonly used for this system [121, 140]. Van der Waals forces were incorporated using Grimme's 2nd method as implemented in VASP citeGrimme:06.

The molecule-substrate system was modeled by a 3 ML thick Co film in a $(25.527\ \text{Å})^3$ super cell with one FePc molecule on top. For the oxidized surface, 1/2 ML of oxygen was added which leads, in agreement with the experiment, to a c(2×2) reconstruction of the Co(001) surface. The calculated height of the O-atoms above the first Co layer was 0.83 Å which is close to the value observed for a c(2×2) O/Ni(001) surface [196]. In order to determine the ground state configuration, the molecule was placed on top, bridge, and hollow site positions with Fe-N_a bonds parallel to the substrate axis and 45° rotated relative to the axis. Except for the bottom Co layer, all atoms were allowed to relax until the forces are smaller than 0.02 eV/Å. All calculations have been performed with a plane wave cutoff of 400 eV and a Γ-point only k-mesh. Only for the determination of the exchange energy, a 3×3×3 mesh was adopted. The comparison of the experimental results with the theoretical NEXAFS of the distorted molecule, cut out from the VASP optimization, are used to investigate the effect of the loss of symmetry on the absorption spectra.

The NEXAFS calculations were carried out for a single FePc molecule using the DFT code StoBe [108] with the transition potential approach, which means that the core hole was described by a half filled N 1s core orbital. The structure of the gas phase molecule had previously been energy-optimized at the B3LYP/DFT level, as described in Ref. [197].

For the N K edge spectra, we have used the generalized gradient corrected exchange functional by Becke [198] and the correlation functional by Perdew [199]. The igloo-iii triple ζ basis of Kutzelnigg, Fleischer and Schindler [200] was employed for describing the core excited N atom, while the remaining N atoms were represented by effective core potentials of 5 electrons provided by the StoBe package. For the other atoms, triple ζ plus valence polarization basis sets provided by the StoBe package were used. In addition, a double basis set technique is used by StoBe to minimize the energy, as well as an augmented diffuse basis set (19s, 19p, 19d) to calculate the excitation energies and the transition moments [201].

The angle resolved spectra of the N K edge were obtained as the average of the spectra of each of the two non-equivalent N atoms in the molecule, which are the pyrrole (N_a, figure A.1) and the aza-bridge N atoms (N_b, figure A.1). Each single N spectrum was aligned to the related ionization potential (IP) calculated with the Δ KS approach. The simulated spectra were convoluted with Gaussian curves of full width at half maximum (FWHM) of 0.5 eV up to the IP, linearly increasing to 8.0 eV for an interval of 50 eV, and constant above. The spectra were moreover shifted by 0.7 eV, which include the relativistic corrections for the N atoms [202].

The two theoretical contributions have different aims, since the programs used have different capabilities. We have used the VASP calculations to accurately

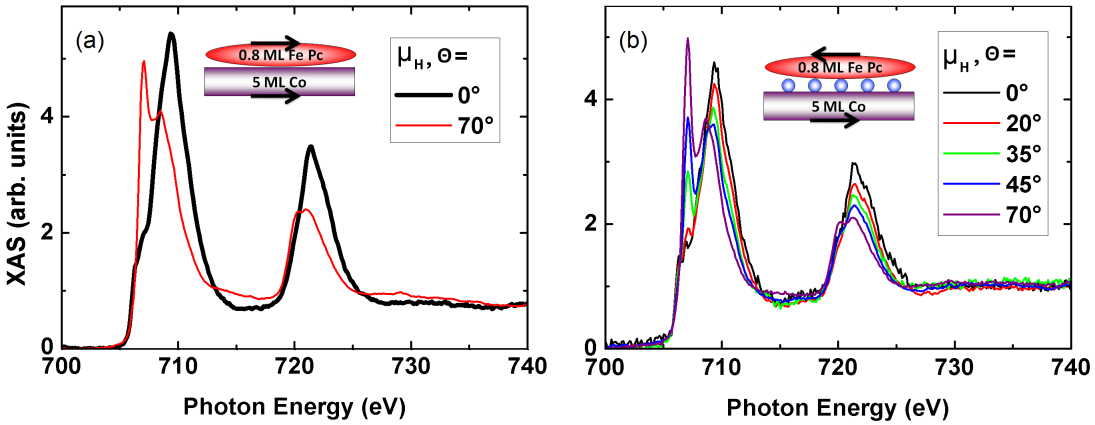

Figure A.2.: Angle-dependent Fe $L_{2,3}$ XAS spectra of 0.8 ML FePc/5 ML Co (top), 0.8 ML FePc/O/5 ML Co (bottom) measured with linearly horizontal polarized X-rays.

determine the adsorption site for the molecule plus substrate. StoBe N K edge calculations were performed instead with the aim to understand the molecular orbital origin of the absorption peaks, which could confirm the strong bonding between the molecule and the surface. With this approach we have been able to consider only the distortion of the molecule induced by the chemisorption, and we have excluded the substrate."

A.2. Angle-dependent x-ray absorption at the Fe $L_2, 3$ edge for the systems FePc/Co/Cu(100) and FePc/O/Co/Cu(100)

The following paragraph is taken from reference [27] and delivers additional information about the electronic structure of the molecule on the surface. "Figure A.2 shows the angle-dependent absorption spectra of linearly polarized photons at the Fe $L_{2,3}$ edges of the two samples 0.8 ML FePc/5ML Co/Cu(100) (a) and 0.8 ML FePc/O/5ML Co/Cu(100) (b). The pectra of the angle-dependent measurements with linearly horizontal polarized x-rays at the Fe $L_{2,3}$ edges show strong linear dichroism, see figure A.2. This confirms the known orientation of the Pc molecules lying flat on the surface [203]. This fact is also underpinned by the N K edge spectra discussed in Sec. 4.1.3. The spectra at the Fe $L_{2,3}$ edges have been recorded for two (five) photon angles in case of the bare (oxidized) Co substrate, see figure A.2. In both cases a detailed angle dependence is observed. For grazing incidence angles there is a clear double structure. For $\theta = 70°$ the sharp peak at the left side of the L_3 edge is even more intense then the broad one. With decreasing angles, the

intensity of the first peak also decreases such that for 20° and 0° it is hardly visible. The structures are sharper for the molecules on the O-covered film and the spectra look more like those of the free molecule, implying once more a weak interaction."

List of publications

Publications contributing to the thesis

D. Klar, A. Candini, L. Joly, S. Klyatskaya, B. Krumme,P. Ohresser, J.-P. Kappler, M. Ruben and H. Wende
Hysteretic behaviour in a vacuum deposited submonolayer of single ion magnets
Dalton Trans. 43, 10686 (2014)

D. Klar, S. Bhandary, A. Candini, L. Joly, P. Ohresser, S. Klyatskaya, M. Schleberger, M. Ruben, M. Affronte, O. Eriksson, B. Sanyal, and H. Wende
Field-regulated switching of the magnetization of Co-porphyrin on graphene
Phys. Rev. B 89, 144411 (2014)

D. Klar, B. Brena, H. C. Herper, S. Bhandary, C. Weis, B. Krumme, C. Schmitz-Antoniak, B. Sanyal, O. Eriksson, and H. Wende
Oxygen-tuned magnetic coupling of Fe-phthalocyanine molecules to ferromagnetic Co films
Phys. Rev. B 88, 224424 (2013)

D. Klar, S. Klyatskaya, A. Candini, B. Krumme, K. Kummer, P. Ohresser, V. Corradini, V. de Renzi, R. Biagi, L. Joly, J.-P. Kappler, U. del Pennino, M. Affronte, H. Wende and M. Ruben
Antiferromagnetic coupling of $TbPc_2$ molecules to ultrathin Ni and Co films
Beilstein J. Nanotechnol.4, 320 (2013)

A. Candini, D. Klar, S. Marocchi, V. Corradini, R. Biagi, V. de Renzi, U. del Pennino, F. Troiani, V. Bellini, S. Klyatskaya, M. Ruben, K. Kummer, N. B. Brookes, H. Huang, A. Soncini, H. Wende and M. Affronte
Spin-communication channels between Ln(III) bis-phthalocyanines molecular nanomagnets and a magnetic substrate (submitted, 2015)

A. Candini, V. Bellini, D. Klar, V. Corradini, R. Biagi, V. De Renzi, K. Kummer, N. B. Brookes, U. del Pennio, H. Wende and M. Affronte
Ferromagnetic Exchange Coupling between Fe Phthalocyanine and Ni(111) Surface Mediated by the Extended States of Graphene
J. Phys. Chem. C 118 (31), 17670-17676 (2014)

Other publications

Y. Lan, S. Klyatskaya, M. Ruben, O. Fuhr, W. Wernsdorfer, A. Candini, V. Corradini, A. L. Rizzini, U. del Pennino, F. Troiani, L. Joly, D. Klar, H. Wende and M. Affronte
Magnetic interplay between two different lanthanides in a tris-phthalocyaninato complex: a viable synthetic route and detailed investigation in the bulk and on the surface
J. Mater. Chem. C (accepted, 2015)

M. E. Gruner, W. Keune, B. Roldan Cuenya, C. Weis, J. Landers, S. I. Makarov, D. Klar, M. Y. Hu, E. E. Alp, J. Zhao, M. Krautz, O. Gutfleisch and H. Wende
Element-Resolved Thermodynamics of Magnetocaloric $LaFe_{13-x}Si_x$
Phys. Rev. Lett. 114, 057202 (2015)

B. Krumme, A. Auge, H. C. Herper, I. Opahle, D. Klar, N. Teichert, L. Joly, P. Ohresser, J. Landers, J. P. Kappler, P. Entel, A. Hütten, and H. Wende
Element-specific electronic structure and magnetic properties of an epitaxial $Ni_{51.6}Mn_{32.9}Sn_{15.5}$ *thin film at the austenite-martensite transition*
Phys. Rev. B 91, 214417 (2015)

B. Schäfer, C. Rajnak, I. Salitros, O. Fuhr, D. Klar, C. Schmitz-Antoniak, E. Weschke, H. Wende and M. Ruben
Room temperature switching of a neutral molecular iron(II) complex
Chem. Commun. 49, 10986-10988 (2013)

Conferences and workshops

2015 Summer School and Workshop on "Magnetism of novel materials - from fundamentals to applications", **two poster contributions**, Uppsala (Sweden)

2015 Evaluation of the SPP1599/2 "Caloric effects in ferroic materials:New concepts for cooling", **poster contribution**, Dresden (Germany)

2014 Heraeus seminar "Functional metalorganics and hybrids", **poster contribution**, Bad Honnef (Germany)

2014 Kick off meeting "NuMathimo", Belfast (United Kingdom)

2014 Focus meeting "Ferroic Cooling", **oral contribution**, Meissen (Germany)

2013 DPG spring meeting, **oral contribution**, Regensburg (Germany)

2013 Workshop "Martensitic transformation", **poster contribution**, Duisburg (Germany)

2013 Focus meeting "Ferroic Cooling", **poster contribution**, Dresden (Germany)

2011 DPG spring meeting, **oral contribution**, Dresden (Germany)

2010 BESSY user meeting, **poster contribution**, Berlin (Germany)

2010 International workshop on Spin Dynamics in Nanomagnets: "Dissipative versus Non-Dissipative Processes", Mülheim an der Ruhr (Germany)

2010 International workshop on "Spin-torque related phenomena in magnetic nanostructures", Mülheim an der Ruhr (Germany)

Acknowledgement

First I want to acknowledge Heiko Wende for giving me the opportunity to work in the field of molecular magnetism and for constantly supporting my research with advice and discussions.

I thank Mario Ruben for his ideas and effort to start several projects contributing to my thesis. I am grateful to Svetlana Klyatskaya for the reliable synthesis of molecules.

Thanks to Andrea Candini for a great collaboration and scientific discussions over the last years. Working together was always interesting, entertaining and also fruitful. I also would like to acknowledge the valuable scientific input from Marco Affronte in several joint projects.

I want to thank Carolin Schmitz-Antoniak for sharing her huge experience and knowledge in many discussions helping me to develop as a scientist. It was always a pleasure spending synchrotron time together.

Without Ulrich von Hörsten hardly any of my research would have been possible. His technical knowledge and skills were extremely important for the functionality of all tools in the lab.

I am thankful to Bernhard Krumme, Claudia Weis and all colleagues in the Wende group for nice collaboration over the last years.

The support from various people during synchrotron time helped to achieve these interestig result. Therefore I thank Loic Joly, Phillipe Ohresser, Eugen Weschke, Jean-Paul Kappler, Valdis Corradini, Roberto Biagi, Valentina di Renzi.

The theoretical support was crucial for a deeper understanding of the experimental results. Thanks to Bipblab Sanyal, Sumantha Bandhary, Heike Herper, Barbara Brena, Olle Erikson, Valerio Bellini, Simone Marocchi, Filippo Troiani.

Last but not least I want to acknowledge the financial support which makes my research possible. Thanks to the DFG proirity programm SPP1591 "ferroic cooling" for financing my PhD position. I also thank the synchroton facilities BESSY II (beamline UE-46_PGM1), SLS (beamline SIM), SOLEIl (beamline DEIMOS) and ESRF (beamline ID08) for providing synchrotron radiation and financial support.

Bibliography

[1] M. N. Baibich, J. Broto, A. Fert, F. N. Van Dau, F. Petroff, P. Etienne, G. Creuzet, A. Friederich, and J. Chazelas, Phys. Rev. Lett. **61**, 2472 (1988).

[2] G. Binasch, P. Grünberg, F. Saurenbach, and W. Zinn, Phys. Rev. B **39**, 4828 (1989).

[3] S. D. Sarma, Am. Sci. **89**, 516 (2001).

[4] I. Žutić, J. Fabian, and S. D. Sarma, Rev. Mod. Phys. **76**, 323 (2004).

[5] D. D. Awschalom, R. Epstein, and R. Hanson, Sci. Am. **297**, 84 (2007).

[6] B. D. Josephson, Phys. Lett. **1**, 251 (1962).

[7] M. Julliere, Phys. Lett. A **54**, 225 (1975).

[8] M. L. Plumer, J. van Ek, and W. C. Cain, arXiv preprint arXiv:1201.5543 (2012).

[9] A. R. Rocha, V. M. Garcia-Suarez, S. W. Bailey, C. J. Lambert, J. Ferrer, and S. Sanvito, Nat. Mater. **4**, 335 (2005).

[10] L. Bogani and W. Wernsdorfer, Nat. Mater. **7**, 179 (2008).

[11] P. Gambardella, S. Stepanow, A. Dmitriev, J. Honolka, F. M. de Groot, M. Lingenfelder, S. S. Gupta, D. Sarma, P. Bencok, S. Stanescu, et al., Nat. Mater. **8**, 189 (2009).

[12] H. Wende, Nat. Mater. **8**, 165 (2009).

[13] S. Sanvito, Nat. Phys. **6**, 562 (2010).

[14] A. Candini, S. Klyatskaya, M. Ruben, W. Wernsdorfer, and M. Affronte, Nano Lett. **11**, 2634 (2011).

[15] M. Urdampilleta, S. Klyatskaya, J. Cleuziou, M. Ruben, and W. Wernsdorfer, Nat. Mater. **10**, 502 (2011).

[16] S. Sanvito, Chem. Soc. Rev. **40**, 3336 (2011).

[17] R. Vincent, S. Klyatskaya, M. Ruben, W. Wernsdorfer, and F. Balestro, Nature **488**, 357 (2012).

[18] V. A. Dediu, L. E. Hueso, I. Bergenti, and C. Taliani, **8**, 707 (2009).

[19] A. Scheybal, T. Ramsvik, R. Bertschinger, M. Putero, F. Nolting, and T. A. Jung, Chem. Phys. Lett. **411**, 214 (2005).

[20] H. Wende, M. Bernien, J. Luo, C. Sorg, N. Ponpandian, J. Kurde, J. Miguel, M. Piantek, X. Xu, P. Eckhold, et al., Nat. Mater. **6**, 516 (2007).

[21] M. Bernien, J. Miguel, C. Weis, M. E. Ali, J. Kurde, B. Krumme, P. M. Panchmatia, B. Sanyal, M. Piantek, P. Srivastava, et al., Phys. Rev. Lett. **102**, 047202 (2009).

[22] S. Javaid, M. Bowen, S. Boukari, L. Joly, J.-B. Beaufrand, X. Chen, Y. Dappe, F. Scheurer, J.-P. Kappler, J. Arabski, et al., Phys. Rev. Lett. **105**, 077201 (2010).

[23] J. Miguel, C. F. Hermanns, M. Bernien, A. Krüger, and W. Kuch, J. Phys. Chem. Lett. **2**, 1455 (2011).

[24] S. Bhandary, O. Eriksson, and B. Sanyal, Sci. Rep. **3** (2013).

[25] A. Lodi Rizzini, C. Krull, T. Balashov, J. Kavich, A. Mugarza, P. Miedema, P. Thakur, V. Sessi, S. Klyatskaya, M. Ruben, et al., Phys. Rev. Lett. **107**, 177205 (2011).

[26] D. Klar, S. Klyatskaya, A. Candini, B. Krumme, K. Kummer, P. Ohresser, V. Corradini, V. de Renzi, R. Biagi, L. Joly, et al., Beilstein J. Nanotechnol. **4**, 320 (2013).

[27] D. Klar, B. Brena, H. Herper, S. Bhandary, C. Weis, B. Krumme, C. Schmitz-Antoniak, B. Sanyal, O. Eriksson, and H. Wende, Phys. Rev. B **88**, 224424 (2013).

[28] D. M. Adams, J. Kerimo, E. J. Olson, A. Zaban, B. A. Gregg, and P. F. Barbara, J. Am. Chem. Soc. **119**, 10608 (1997).

[29] J. C. Conboy, E. J. Olson, D. M. Adams, J. Kerimo, A. Zaban, B. A. Gregg, and P. F. Barbara, J. Phys. Chem. B **102**, 4516 (1998).

[30] M. Thelakkat, C. Schmitz, and H.-W. Schmidt, Adv. Mater. **14**, 577 (2002).

[31] S. Baranton, C. Coutanceau, C. Roux, F. Hahn, and J.-M. Léger, J. Electroanal. Chem. **577**, 223 (2005).

[32] P. Liljeroth, J. Repp, and G. Meyer, Science **317**, 1203 (2007).

[33] R. Wormald, J. Evans, L. Smeeth, and K. Henshaw, Cochrane Database Syst Rev **3** (2007).

[34] Y. Wang, J. Kröger, R. Berndt, and W. A. Hofer, J. Am. Chem. Soc. **131**, 3639 (2009).

[35] A. Yella, H.-W. Lee, H. N. Tsao, C. Yi, A. K. Chandiran, M. K. Nazeeruddin, E. W.-G. Diau, C.-Y. Yeh, S. M. Zakeeruddin, and M. Grätzel, Science **334**, 629 (2011).

[36] D. Klar, A. Candini, L. Joly, S. Klyatskaya, B. Krumme, P. Ohresser, J.-P. Kappler, M. Ruben, and H. Wende, Dalton Trans. **43**, 10686 (2014).

[37] R. Sessoli, D. Gatteschi, A. Caneschi, and M. Novak, Nature **365**, 141 (1993).

[38] G. Christou, D. Gatteschi, D. N. Hendrickson, and R. Sessoli, Mrs Bull p. 67 (2000).

[39] J. D. Rinehart and J. R. Long, Chem. Sci. **2**, 2078 (2011).

[40] N. Ishikawa, M. Sugita, and W. Wernsdorfer, Angew. Chem. Int. Ed. **44**, 2931 (2005).

[41] L. Margheriti, D. Chiappe, M. Mannini, P. Car, P. Sainctavit, M. A. Arrio, F. B. de Mongeot, J. C. Cezar, F. M. Piras, A. Magnani, et al., Adv. Mater. **22**, 5488 (2010).

[42] S. Stepanow, J. Honolka, P. Gambardella, L. Vitali, N. Abdurakhmanova, T.-C. Tseng, S. Rauschenbach, S. L. Tait, V. Sessi, S. Klyatskaya, et al., J. Am. Chem. Soc. **132**, 11900 (2010).

[43] J. Stöhr and H. C. Siegmann, *Magnetism: from fundamentals to nanoscale dynamics*, vol. 152 (Springer, Berlin, 2007).

[44] J. H. van Vleck, Phys. Rev. **52**, 1178 (1937).

[45] W. Kossel, Ann. Phys. **354**, 229 (1916).

[46] P. Schuster, *Ligandenfeldtheorie* (Verlag Chemie, Weinheim, 1973).

[47] J. Reinhold, *Quantentheorie der Moleküle* (Teubner, Wiesbaden, 2004).

[48] M. S. Silberberg, *Principles of general chemistry* (McGraw-Hill Higher Education, New York, 2007).

[49] B. N. Figgis, *Ligand field theory In Comprehensive Coordination Chemistry*, vol. 1 (ed. G. Wilkinson, R. D. Gillard and J. A. McCleverty, Pergamon Press: Elmsford, New York, 1987).

[50] J. B. Goodenough, Phys. Rev. **100**, 564 (1955).

[51] J. B. Goodenough, J. Phys. Chem. Sol. **6**, 287 (1958).

[52] J. Kanamori, J. Phys. Chem. Sol. **10**, 87 (1959).

[53] N. Ishikawa, M. Sugita, T. Okubo, N. Tanaka, T. Iino, and Y. Kaizu, Inorg. Chem. **42**, 2440 (2003).

[54] W. Jitschin, F. Sharipov, R. Lachenmann, and K. Jousten, *Wutz Handbuch Vakuumtechnik* (Springer, 2009).

[55] L. Meitner, Z. Phys. **9**, 131 (1922).

[56] P. Auger, Compt. Rend. **177**, 169 (1923).

[57] A. Einstein, Ann. Phys. **322**, 132 (1905).

[58] K. K. Kolasinski, *Surface Science: Foundations of Catalysis and Nanoscience*, vol. 3 (Wiley, 2012).

[59] A. Grüneis, K. Kummer, and D. V. Vyalikh, New J. Phys. **11**, 073050 (2009).

[60] W. H. Bragg and W. L. Bragg, *X-rays and Crystal Structure* (G. Bell and sons, Limited, 1918).

[61] L. De Broglie, Nobel lecture **12**, 244 (1929).

[62] D. Chylarecka, T. K. Kim, K. Tarafder, K. Müller, K. Gödel, I. Czekaj, C. Wäckerlin, M. Cinchetti, M. E. Ali, C. Piamonteze, et al., J. Chem. Phys. **115**, 1295 (2011).

[63] G. Binnig, H. Rohrer, C. Gerber, and E. Weibel, Phys. Rev. Lett. **49**, 57 (1982).

[64] G. Binnig and H. Rohrer, Rev. Mod. Phys. **59**, 615 (1987).

[65] A. Candini, D. Klar, S. Marocchi, V. Corradini, R. Biagi, V. de Renzi, U. del Pennino, F. Troiani, V. Bellini, S. Klyatskaya, et al., Sci. Rep. (2016).

[66] C. Enss and S. Hunklinger, *Low-Temperature Physics* (Springer, 2005).

[67] F. Pobell, *Matter and methods at low temperatures*, vol. 2 (Springer, 2007).

[68] É. Clapeyron, *Mémoire sur la puissance motrice de la chaleur* (J. Gabay, 1834).

[69] R. Clausius, Ann. Phys. **155**, 368 (1850).

[70] D. A. Shea and D. Morgan (Congressional Research Service, Library of Congress, 2010).

[71] O. V. Lounasmaa, *Experimental principles and methods below 1 K*, vol. 8 (Academic Press London, 1974).

[72] D. Betts and R. Scurlock, Cryogenics **17**, 583 (1977).

[73] P. Sainctavit and J.-P. Kappler, in *Magnetism and Synchrotron Radiation* (Springer, 2001), pp. 235–253.

[74] I. Letard, P. Sainctavit, J.-P. Kappler, P. Ghigna, D. Gatteschi, B. Doddi, et al., J. Appl. Phys. **101**, 113920 (2007).

[75] D. Koningsberger and R. Prins, *X-ray absorption: principles, applications, techniques of EXAFS, SEXAFS, and XANES* (John Wiley and Sons, New York, NY, 1988).

[76] W. Gudat and C. Kunz, Phys. Rev. Lett. **29**, 169 (1972).

[77] A. Beer, Ann. Phys. Chem **86**, 78 (1852).

[78] E. Beaurepaire, H. Bulou, F. Scheurer, and J. P. Kappler, *Magnetism and synchrotron radiation* (Springer, 2010).

[79] E. Fermi and J. Orear, *Nuclear physics: a course given by Enrico Fermi at the University of Chicago* (University of Chicago Press, 1950).

[80] P. A. Dirac, Proc. R. Soc. A pp. 243–265 (1927).

[81] A. Messiah, *Quantenmechanik vol. 1* (1958).

[82] G. P. Williams, *X-ray data booklet* (2001).

[83] J. Hubbell, H. A. Gimm, et al., J. Phys. Chem. Ref. Data **9**, 1023 (1980).

[84] J. Erskine and E. Stern, Phys. Rev. B **12**, 5016 (1975).

[85] G. Schütz, W. Wagner, W. Wilhelm, P. Kienle, R. Zeller, R. Frahm, and G. Materlik, Phys. Rev. Lett. **58**, 737 (1987).

[86] B. T. Thole, P. Carra, F. Sette, and G. van der Laan, Phys. Rev. Lett. **68**, 1943 (1992).

[87] P. Carra, B. T. Thole, M. Altarelli, and X. Wang, Phys. Rev. Lett. **70**, 694 (1993).

[88] H. C. Herper, M. Bernien, S. Bhandary, C. F. Hermanns, A. Krüger, J. Miguel, C. Weis, C. Schmitz-Antoniak, B. Krumme, D. Bovenschen, et al., Phys. Rev. B **87**, 174425 (2013).

[89] F. Elder, A. Gurewitsch, R. Langmuir, and H. Pollock, Phys. Rev. **71**, 829 (1947).

[90] J. Schwinger, Phys. Rev. **75**, 1912 (1949).

[91] S. Sasaki, K. Miyata, and T. Takada, Jpn. J. Appl. Phys. **31**, L1794 (1992).

[92] S. Sasaki, Nucl. Instr. Meth. Phys. Res. **347**, 83 (1994).

[93] http://www.psi.ch/media/the-swiss-light-source-sls (Dec-1-2009).

[94] A. Rogalev, V. Gotte, J. Goulon, C. Gauthier, J. Chavanne, and P. Elleaume, J. Synchrotron Radiat. **5**, 989 (1998).

[95] C. Sorg, N. Ponpandian, A. Scherz, H. Wende, R. Nünthel, T. Gleitsmann, and K. Baberschke, Surf. Sci. **565**, 197 (2004).

[96] M. Bernien, X. Xu, J. Miguel, M. Piantek, P. Eckhold, J. Luo, J. Kurde, W. Kuch, K. Baberschke, H. Wende, et al., Phys. Rev. B **76**, 214406 (2007).

[97] B. Krumme, D. Ebke, C. Weis, S. Makarov, A. Warland, A. Hütten, and H. Wende, Appl. Phys. Lett. **101**, 232403 (2012).

[98] C. F. Hermanns, K. Tarafder, M. Bernien, A. Krüger, Y.-M. Chang, P. M. Oppeneer, and W. Kuch, Adv. Mater. (2013).

[99] D. Klar, S. Bhandary, A. Candini, L. Joly, P. Ohresser, S. Klyatskaya, M. Schleberger, M. Ruben, M. Affronte, O. Eriksson, et al., Phys. Rev. B **89**, 144411 (2014).

[100] D. Klar, *Röntgenabsorptionsuntersuchung der magnetischen kopplungsphänomene von fe-phthalocyanin-molekülen auf ni- und co-filmen* (University Duisburg-Essen, 2011).

[101] R. Nünthel, T. Gleitsmann, P. Poulopoulos, A. Scherz, J. Lindner, E. Kosubek, C. Litwinski, Z. Li, H. Wende, K. Baberschke, et al., Surf. Sci. **531**, 53 (2003).

[102] C. M. Schneider, P. Bressler, P. Schuster, J. Kirschner, J. D. Miguel, and R. Mirand, Phys. Rev. Lett. **64**, 1059 (1990).

[103] J. Hong, R. Wu, J. Lindner, E. Kosubek, and K. Baberschke, Phys. Rev. Lett. **92**, 147202 (2004).

[104] C. Sorg, N. Ponpandian, M. Bernien, K. Baberschke, H. Wende, and R. Wu, Phys. Rev. B **73**, 64409 (2006).

[105] X. Liu, T. Iimori, K. Nakatsuji, and F. Komori, Appl. Phys. Lett. **88**, 133102 (2006).

[106] G. Kresse and J. Furthmüller, Comput. Mater. Sci. **6**, 15 (1996).

[107] G. Kresse and J. Joubert, Phys. Rev. B **59**, 1758 (1999).

[108] StoBe-deMon version 3.0 (2007), Hermann, K.; Pettersson, L.G.M., Casida, M.E.; Daul, C; Goursot, A.; Koester, A.; Proynov, E.; St-Amant, A.; Salahub *et al*.

[109] M. Lackinger and M. Hietschold, Surf. Sci. **520**, L619 (2002).

[110] C. Bobisch, T. Wagner, A. Bannani, and R. Möller, J. Chem. Phys. **119**, 9804 (2003).

[111] A. Gerlach, F. Schreiber, S. Sellner, H. Dosch, I. Vartanyants, B. Cowie, T.-L. Lee, and J. Zegenhagen, Phys. Rev. B **71**, 205425 (2005).

[112] C. Stadler, S. Hansen, F. Pollinger, C. Kumpf, E. Umbach, T.-L. Lee, and J. Zegenhagen, Phys. Rev. B **74**, 035404 (2006).

[113] H. Karacuban, M. Lange, J. Schaffert, O. Weingart, T. Wagner, and R. Möller, Surf. Sci. **603**, L39 (2009).

[114] C. Stadler, S. Hansen, I. Kröger, C. Kumpf, and E. Umbach, Nat. Phys. **5**, 153 (2009).

[115] Y. Wang, J. Kröger, R. Berndt, and W. Hofer, Angew. Chem. Int. Ed. **48**, 1261 (2009).

[116] X. Chen and M. Alouani, Phys. Rev. B **82**, 094443 (2010).

[117] H.-l. Fan, S.-l. Lei, J. Huang, and Q.-x. Li, Chin. J. Chem. Phys. **23**, 565 (2010).

[118] I. Kröger, B. Stadtmüller, C. Stadler, J. Ziroff, M. Kochler, A. Stahl, F. Pollinger, T.-L. Lee, J. Zegenhagen, F. Reinert, et al., New J. Phys. **12**, 083038 (2010).

[119] I. Kröger, B. Stadtmüller, C. Kleimann, P. Rajput, and C. Kumpf, Phys. Rev. B **83**, 195414 (2011).

[120] B. Stadtmüller, I. Kröger, F. Reinert, and C. Kumpf, Phys. Rev. B **83**, 085416 (2011).

[121] S. Lach, A. Altenhof, K. Tarafder, F. Schmitt, M. E. Ali, M. Vogel, J. Sauther, P. M. Oppeneer, and C. Ziegler, Adv. Func. Mater. **22**, 989 (2012).

[122] T. Kroll, R. Kraus, R. Schonfelder, V. Aristov, O. Molodtsova, P. Hoffmann, and M. Knupfer, J. Chem. Phys. **137**, 054306 (2012).

[123] N. Haack, G. Ceballos, H. Wende, K. Baberschke, D. Arvanitis, A. Ankudinov, and J. Rehr, Phys. Rev. Lett. **84**, 614 (2000).

[124] E. Annese, J. Fujii, I. Vobornik, G. Panaccione, and G. Rossi, Phys. Rev. B **84**, 174443 (2011).

[125] A. Candini, V. Bellini, D. Klar, V. Corradini, R. Biagi, V. De Renzi, K. Kummer, N. B. Brookes, U. del Pennino, H. Wende, et al., J. Phys. Chem. C **118**, 17670 (2014).

[126] K. S. Novoselov, A. K. Geim, S. Morozov, D. Jiang, Y. Zhang, S. Dubonos, I. Grigorieva, and A. Firsov, Science **306**, 666 (2004).

[127] A. K. Geim and K. S. Novoselov, Nat. Mater. **6**, 183 (2007).

[128] Y. S. Dedkov and M. Fonin, New J. Phys. **12**, 125004 (2010).

[129] Y. S. Dedkov, M. Fonin, and C. Laubschat, Appl. Phys. Lett. **92**, 052506 (2008).

[130] A. L. Walter, S. Nie, A. Bostwick, K. S. Kim, L. Moreschini, Y. J. Chang, D. Innocenti, K. Horn, K. F. McCarty, and E. Rotenberg, Phys. Rev. B **84**, 195443 (2011).

[131] J. P. Perdew, K. Burke, and M. Ernzerhof, Phys. Rev. Lett. **77**, 3865 (1996).

[132] S. Grimme, J. Comp. Chem. **27**, 1787 (2006).

[133] S. Marocchi, P. Ferriani, N. Caffrey, F. Manghi, S. Heinze, and V. Bellini, Phys. Rev. B **88**, 144407 (2013).

[134] E. Annese, F. Casolari, J. Fujii, and G. Rossi, Phys. Rev. B **87**, 054420 (2013).

[135] P. Gargiani, G. Rossi, R. Biagi, V. Corradini, M. Pedio, S. Fortuna, A. Calzolari, S. Fabris, J. C. Cezar, N. Brookes, et al., Phys. Rev. B **87**, 165407 (2013).

[136] W. Zhao, S. M. Kozlov, O. Höfert, K. Gotterbarm, M. P. Lorenz, F. Vines, C. Papp, A. Görling, and H.-P. Steinrück, J. Phys. Chem. Lett. **2**, 759 (2011).

[137] F. Bianchini, L. L. Patera, M. Peressi, C. Africh, and G. Comelli, J. Phys. Chem. Lett. **5**, 467 (2014).

[138] J. Hu and R. Wu, Phys. Rev. Lett. **110**, 097202 (2013).

[139] N. Marom and L. Kronik, Appl. Phys. A **95**, 165 (2009).

[140] A. Mugarza, R. Robles, C. Krull, R. Korytár, N. Lorente, and P. Gambardella, Phys. Rev. B **85**, 155437 (2012).

[141] V. Karpan, G. Giovannetti, P. Khomyakov, M. Talanana, A. Starikov, M. Zwierzycki, J. Van Den Brink, G. Brocks, and P. Kelly, Phys. Rev. Lett. **99**, 176602 (2007).

[142] C. F. Hermanns, M. Bernien, A. Krüger, W. Walter, Y.-M. Chang, E. Weschke, and W. Kuch, Phys. Rev. B **88**, 104420 (2013).

[143] G. Kresse and J. Hafner, Phys. Rev. B **47**, 558 (1993).

[144] V. I. Anisimov, F. Aryasetiawan, and A. Lichtenstein, J. Phys. Condens. Matter **9**, 767 (1997).

[145] P. M. Panchmatia, B. Sanyal, and P. M. Oppeneer, Chem. Phys. **343**, 47 (2008).

[146] S. Bhandary, B. Brena, P. M. Panchmatia, I. Brumboiu, M. Bernien, C. Weis, B. Krumme, C. Etz, W. Kuch, H. Wende, et al., Phys. Rev. B **88**, 024401 (2013).

[147] X. Chen, Y.-S. Fu, S.-H. Ji, T. Zhang, P. Cheng, X.-C. Ma, X.-L. Zou, W.-H. Duan, J.-F. Jia, and Q.-K. Xue, Phys. Rev. Lett. **101**, 197208 (2008).

[148] M. Mannini, F. Pineider, P. Sainctavit, C. Danieli, E. Otero, C. Sciancalepore, A. M. Talarico, M.-A. Arrio, A. Cornia, D. Gatteschi, et al., Nat. Mater. **8**, 194 (2009).

[149] M. N. Leuenberger and D. Loss, Nature **410**, 789 (2001).

[150] A. Ardavan, O. Rival, J. J. Morton, S. J. Blundell, A. M. Tyryshkin, G. A. Timco, and R. E. Winpenny, Phys. Rev. Lett. **98**, 057201 (2007).

[151] P. C. Stamp and A. Gaita-Arino, J. Mater. Chem. **19**, 1718 (2009).

[152] W. Wernsdorfer, N. Aliaga-Alcalde, D. N. Hendrickson, and G. Christou, Nature **416**, 406 (2002).

[153] D. Gatteschi and R. Sessoli, Angew. Chem. Int. Ed. **42**, 268 (2003).

[154] A. Barra, A. Caneschi, A. Cornia, F. Fabrizi de Biani, D. Gatteschi, C. Sangregorio, R. Sessoli, and L. Sorace, J. Am. Chem. Soc. **121**, 5302 (1999).

[155] A. Bouwen, A. Caneschi, D. Gatteschi, E. Goovaerts, D. Schoemaker, L. Sorace, and M. Stefan, J. Phys. Chem. B **105**, 2658 (2001).

[156] M. Mannini, F. Pineider, C. Danieli, F. Totti, L. Sorace, P. Sainctavit, M.-A. Arrio, E. Otero, L. Joly, J. C. Cezar, et al., Nature **468**, 417 (2010).

[157] F. Branzoli, P. Carretta, M. Filibian, G. Zoppellaro, M. J. Graf, J. R. Galan-Mascaros, O. Fuhr, S. Brink, and M. Ruben, J. Am. Chem. Soc. **131**, 4387 (2009).

[158] M. Gonidec, E. S. Davies, J. McMaster, D. B. Amabilino, and J. Veciana, J. Am. Chem. Soc. **132**, 1756 (2010).

[159] M. Gonidec, R. Biagi, V. Corradini, F. Moro, V. De Renzi, U. del Pennino, D. Summa, L. Muccioli, C. Zannoni, D. B. Amabilino, et al., J. Am. Chem. Soc. **133**, 6603 (2011).

[160] O. Kahn, *Molecular Magnetism* (VCH, New York, 1993).

[161] A. Palii, B. Tsukerblat, S. Klokishner, K. R. Dunbar, J. M. Clemente-Juan, and E. Coronado, Chem. Soc. Rev. **40**, 3130 (2011).

[162] F. Branzoli, P. Carretta, M. Filibian, M. Graf, S. Klyatskaya, M. Ruben, F. Coneri, and P. Dhakal, Phys. Rev. B **82**, 134401 (2010).

[163] www.webelements.com (Jan-20-2015).

[164] http://tc2mascot.lifescience.ntu.edu.tw/mascot/help/mass_accuracy_help.html (Jan-23-2015).

[165] D. Markovitsi, T.-H. Tran-Thi, R. Even, and J. Simon, Chem. Phys. Lett. **137**, 107 (1987).

[166] M. Moussavi, A. De Cian, J. Fischer, and R. Weiss, Inorg. Chem. **27**, 1287 (1988).

[167] H. Konami, M. Hatano, and A. Tajiri, Chem. Phys. Lett. **160**, 163 (1989).

[168] N. Ishikawa, Y. Mizuno, S. Takamatsu, T. Ishikawa, and S.-y. Koshihara, Inorg. Chem. **47**, 10217 (2008).

[169] K. Katoh, T. Komeda, and M. Yamashita, Dalton Trans. **39**, 4708 (2010).

[170] L. Malavolti, M. Mannini, P.-E. Car, G. Campo, F. Pineider, and R. Sessoli, J. Mater. Chem. C **1**, 2935 (2013).

[171] A. Candini, G. Gazzadi, A. Di Bona, M. Affronte, D. Ercolani, G. Biasiol, and L. Sorba, Nanotechnology **17**, 2105 (2006).

[172] P. Ohresser, E. Otero, F. Choueikani, K. Chen, S. Stanescu, F. Deschamps, T. Moreno, F. Polack, B. Lagarde, J.-P. Daguerre, et al., Rev. Sci. Instrum. **85**, 013106 (2014).

[173] A. Lodi Rizzini, C. Krull, T. Balashov, A. Mugarza, C. Nistor, F. Yakhou, V. Sessi, S. Klyatskaya, M. Ruben, S. Stepanow, et al., Nano Lett. **12**, 5703 (2012).

[174] L. Malavolti, L. Poggini, L. Margheriti, D. Chiappe, P. Graziosi, B. Cortigiani, V. Lanzilotto, F. B. de Mongeot, P. Ohresser, E. Otero, et al., Chem. Commun. **49**, 11506 (2013).

[175] B. Schulz and K. Baberschke, Phys. Rev. B **50**, 13467 (1994).

[176] R. Biagi, J. Fernandez-Rodriguez, M. Gonidec, A. Mirone, V. Corradini, F. Moro, V. De Renzi, U. Del Pennino, J. Cezar, D. Amabilino, et al., Phys. Rev. B **82**, 224406 (2010).

[177] L. Vitali, S. Fabris, A. M. Conte, S. Brink, M. Ruben, S. Baroni, and K. Kern, Nano Lett. **8**, 3364 (2008).

[178] K. Stevens, Proc. Phys. Soc. A **65**, 209 (1952).

[179] A. Abragam and B. Bleaney, *Electron paramagnetic resonance of transition ions* (Oxford University Press, 1970).

[180] J. Klanke, E. Rentschler, K. Medjanik, D. Kutnyakhov, G. Schönhense, S. Krasnikov, I. Shvets, S. Schuppler, P. Nagel, M. Merz, et al., Phys. Rev. Lett. **110**, 137202 (2013).

[181] D. Gatteschi, R. Sessoli, and J. Villain, *Molecular nanomagnets* (Oxford University Press, 2006).

[182] L. Sorace, C. Benelli, and D. Gatteschi, Chem. Soc. Rev. **40**, 3092 (2011).

[183] P. Giannozzi, S. Baroni, N. Bonini, M. Calandra, R. Car, C. Cavazzoni, D. Ceresoli, G. L. Chiarotti, M. Cococcioni, I. Dabo, et al., J. Phys. Condens. Matter **21**, 395502 (2009).

[184] A. Liechtenstein, V. Anisimov, and J. Zaanen, Phys. Rev. B **52**, R5467 (1995).

[185] P. E. Blöchl, Phys. Rev. B **50**, 17953 (1994).

[186] http://www.qe-forge.org/gf/project/pslibrary/ (Jul-9-2014).

[187] P. Larson, W. R. Lambrecht, A. Chantis, and M. van Schilfgaarde, Phys. Rev. B **75**, 045114 (2007).

[188] J. Schwöbel, Y. Fu, J. Brede, A. Dilullo, G. Hoffmann, S. Klyatskaya, M. Ruben, and R. Wiesendanger, Nature Commun. **3**, 953 (2012).

[189] K. Katoh, Y. Yoshida, M. Yamashita, H. Miyasaka, B. K. Breedlove, T. Kajiwara, S. Takaishi, N. Ishikawa, H. Isshiki, Y. F. Zhang, et al., J. Am. Chem. Soc. **131**, 9967 (2009).

[190] T. Komeda, H. Isshiki, J. Liu, Y.-F. Zhang, N. Lorente, K. Katoh, B. K. Breedlove, and M. Yamashita, Nature Commun. **2**, 217 (2011).

[191] M. Lopes, A. Candini, M. Urdampilleta, A. Reserbat-Plantey, V. Bellini, S. Klyatskaya, L. Marty, M. Ruben, M. Affronte, W. Wernsdorfer, et al., ACS nano **4**, 7531 (2010).

[192] X. Ling, L. Xie, Y. Fang, H. Xu, H. Zhang, J. Kong, M. S. Dresselhaus, J. Zhang, and Z. Liu, Nano Lett. **10**, 553 (2009).

[193] Y. Lan, S. Klyatskaya, M. Ruben, O. Fuhr, W. Wernsdorfer, A. Candini, V. Corradini, A. L. Rizzini, U. del Pennino, F. Troiani, et al., J. Mater. Chem. C (2015).

[194] F. Huttmann, D. Klar, N. Atodiresei, C. Schmitz-Antoniak, A. Smekhova, A. J. Martinez-Galera, V. Caciuc, T. Michely, and H. Wende, in preparation (2015).

[195] S. L. Dudarev, G. A. Botton, S. Y. Savrasov, C. J. Humphreys, and A. P. Sutton, Phys. Rev. B **57**, 1505 (1998).

[196] C. Xu, J. S. burnham, S. H. Gross, K. Caffey, and N. Winograd, Phys. Rev. B **49**, 4842 (1994).

[197] B. Brena, C. Puglia, M. de Simone, M. Coreno, K. Tarafder, V. Feyer, R. Banerjee, E. Göthelid, B. Sanyal, P. M. Oppeneer, et al., J. Chem. Phys. **134**, 074312 (2011).

[198] A. D. Becke, Phys. Rev. A **38**, 3098 (1988).

[199] J. P. Perdew, Phys. Rev. B **33**, 8822 (1986).

[200] W. Kutzelnigg, U. Fleischer, and M. Schindler, in *NMR Basic Principles and Progress* (Springer Verlag, Berlin/Heidelberg, 1991), vol. 23, pp. 165–262.

[201] L. Triguero, L. G. M. Pettersson, and H. Ågren, Phys. Rev. B **58**, 8097 (1998).

[202] L. T. O. Plashkevych, L. G. M. Pettersson, and H. Ågren, J. Electron Spectrosc. Relat. Phenom. **104**, 195 (1999).

[203] M. L. M. Rocco, K. H. Frank, P. Yannoulis, and E. E. Koch, J. Chem. Phys. **93**, 6859 (1990).